Atomic Structure and Dynamics Study of Defects in Graphene by Aberration-corrected Transmission Electron Microscope

Chuncheng Gong

Supervised by Professor Jamie H. Warner

Submitted in conformity with the requirements

for the degree of DPhil in Materials Science

Department of Materials

St Hugh's College

University of Oxford

September 2016

Abstract

Atomic Structure and Dynamics Study of Defects in Graphene by Aberration-corrected Transmission Electron Microscope

by Chuncheng Gong

St Hugh's College

in pursuit of DPhil degree, Trinity Term, 2016

Graphene has grabbed enormous research attention due to its multiple unique properties. These properties, however, can be strongly influenced by lattice imperfections. Aberration corrected transmission electron microscopy (AC-TEM) is one of the leading methods to image two-dimensional materials at the atomic level. This thesis addresses the issue of structure and dynamics characterization of dislocations and grain boundaries (GBs) in graphene with single atom sensitivity using the state-of-the-art AC-TEM in Department of Materials, University of Oxford.

My first goal is to understand the interaction between dislocation and the edge of graphene. When a dislocation is located near an edge, a decrease in the rippling and increase of the in-plane rotation occurs relative to the dislocations in the bulk. The increased in-plane rotation near the edge causes bond rotations at the edge of graphene to reduce the overall strain in the system. Dislocations are highly stable and remain fixed in their position even when located within a few lattice spacings from the graphene edge.

With the aid of an *in situ* heating holder, the high temperature behavior of dislocations is then investigated. Control of temperature enables the differentiation of electron beam induced effects and thermally driven processes. An analysis of the dislocation

movement shows both climb and glide processes, including new complex pathways for migration and large nanoscale rapid jumps between fixed positions in the lattice. The improved understanding of the high temperature dislocation movement provides insights into annealing processes in graphene and the behavior of defects with increased heat.

The *in situ* heterogeneous nucleation and growth of graphene are also studied within the AC-TEM. The growth mechanism consists of alternating carbon cluster attachment and indentation filling to maintain a uniform growth front of lowest energy. The highly polycrystalline graphene seed is found to evolve with time into a higher order crystalline structure. The motion of GBs is discontinuous and mediated by both bond rotation and atom evaporation. These results provide insights into the formation of crystalline seed domains that are generated during bottom-up graphene synthesis.

Finally, the formation, reconfiguration and annihilation of GB loops are demonstrated. It is shown that the GB loop cannot fully relaxed under electron beam irradiation with its terminal state being isolated dislocations far apart from each other. Line defects composed of several adjacent excess-atom defects can be found during the reconfiguration process. This work gives detailed information about the stability and behavior of large GB loops in two dimensional materials.

Declaration

The material contained within this thesis has not previously been submitted for a degree at the University of Oxford or any other university. The research reported within this thesis has been conducted by the author unless indicated otherwise.

Copyright Notice

Acknowledgement

This doctorate project would not have been accomplished without the guidance, support and encouragement from my supervisor, senior colleagues, friends and family. Firstly and foremost, I would like to express my sincere and profound gratitude to my supervisor, Professor Jamie Warner. The research in this thesis was only made possible under his meticulous and kindest supervision throughout my three-year DPhil time in Oxford. He showed me by example what a good material scientist should be like. He also passed on to me his superb skills in electron microscopy without any reservation, which will certainly benefit me for my future career in science. It is the greatest honor of mine to have the opportunity of being his student.

I would also like to extend my gratitude to the university staff, my senior colleagues and collaborators who offered their advice and support to my project: Dr Kuang He and Dr Alex Robertson for their selfless help in TEM training and image analysis; Mr Ye Fan for his guidance in the CVD synthesis of graphene; Dr Judy Kim and Dr Christopher Allen for being constantly genial and supportive during my use of Oxford-Jeol 2200MCO TEM; Ms Jennifer Holter and Mr Greg Cook for their training and technical help on Jeol 2010 TEM; Mr Paul Pattinson for his support and in the clean room in Department of Physics. Special thanks to my collaborator, Professor Gun-Do Lee from Seoul National University for performing TBMD and DFT calculations which provided the theory basis for my work.

I also want to thank the Clarendon Scholarship Fund for the generous financial assistance of tuition and living expenses over the past 3 years. To my friends in Oxford,

Dr Qifeng Yang and Dr Liye Yan – your continuous friendship and encouragement helped me go though the most difficult time. Last but not the least, the most profound gratitude to my parents for their love and unconditional support regardless of what happens.

Publications

In this section, a list of published research accomplished during the course of this doctorate project is presented. The result chapters in this thesis are based on 4 first author publications.

Chapter 4

1. **Gong, C.**; He, K.; Robertson, A. W.; Yoon, E.; Lee, G.-D.; Warner, J. H. Spatially Dependent Lattice Deformations for Dislocations at the Edges of Graphene. ***ACS Nano*** 2015, 9(1), 656–662.

Chapter 5

2. **Gong, C.**; Robertson, A. W.; He, K.; Lee, G.-D.; Yoon, E.; Allen, C. S.; Kirkland, A. I.; Warner, J. H. Thermally Induced Dynamics of Dislocations in Graphene at Atomic Resolution. ***ACS Nano*** 2015, 9(10), 10066–10075.

Chapter 6

3. **Gong, C.**; He, K.; Lee, G.-D.; Chen, Q.; Robertson, A. W.; Yoon, E.; Hong, S.; Warner, J. H. *In situ* Atomic Level Dynamics of Heterogeneous Nucleation of Graphene From Inorganic Nanoparticle Seeds. ***ACS Nano*** 2016, 10(10), 9397–9410.

Chapter 7

4. **Gong, C.**; He, K.; Chen, Q.; Robertson, A. W.; Warner, J. H. *In situ* High Temperature Atomic Level Studies of Large Closed Grain Boundary Loops in Graphene. ***ACS Nano*** 2016, 10(10), 9165–9173.

First-Author

5. **Gong C.**, Robertson, A. W.; He, K.; Ford, C.; Watt, A. A.; Warner, J. H. Interactions of Pb and Te Atoms with Graphene. ***Dalton Transactions*** 2014, 43(20), 7442-7448.

Second-Author

6. Dave S. H.; **Gong C.**; Robertson A. W.; Warner, J. H.; Grossman J. C. Chemistry and Structure of Graphene Oxide *via* Direct Imaging. ***ACS Nano***, 2016, 10(8): 7515-7522.

Co-Author

7. Chen, Q.; Robertson, A. W.; He, K.; **Gong, C.**; Yoon, E.; Kirkland, A. I.; Lee, G. D.; Warner, J. H. Elongated Silicon–Carbon Bonds at Graphene Edges. ***ACS Nano*** 2015, 10(1), 142-149.

8. Robertson, A. W.; Lee, G. -D.; He, K.; **Gong, C.**; Chen, Q.; Yoon, E.; Kirkland, A. I.; Warner, J. H. Atomic Structure of Graphene Subnanometer Pores. ***ACS Nano*** 2015, 9(12), 11599-11607.

9. Bonilla, L. L.; Carpio, A.; **Gong, C.**; Warner, J. H. Measuring strain and rotation fields at the dislocation core in graphene. ***Physical Review B*** 2015, 92(15), 155417.

10. Chen, Q.; Robertson, A. W.; He, K.; **Gong, C.**; Yoon, E.; Lee, G. -D.; Warner, J. H. Atomic Level Distributed Strain within Graphene Divacancies from Bond Rotations. ***ACS Nano*** 2015, 9(8), 8599-8608.

11. He, K.; Robertson, A. W.; **Gong, C.**; Allen, C. S.; Xu, Q.; Zandbergen, H.; Grossman, J. C.; Kirkland, A. I.; Warner, J. H. Controlled Formation of Closed-edge Nanopores in Graphene. ***Nanoscale*** 2015, 7(27), 11602-11610.

Table of Contents

Chapter 1

Introduction

1.1 Project aims

This objective of this thesis is to characterize the configuration and dynamics of one-dimensional defects (dislocations and grain boundaries) in graphene with single atom sensitivity at both room temperature and elevated temperatures. It is accomplished with the help of Oxford's state-of-the-art aberration-corrected transmission electron microscope (AC-TEM) and multiple advanced image analysis techniques.

1.2 The scope of this thesis

This doctorate project summarizes the research performed over the 3-year-DPhil course at the Department of Materials and St Hugh's College, University of Oxford, funded by Clarendon Scholarship Fund. The tight-binding molecular dynamics (TBMD) and density functional theory (DFT) simulation in this thesis are performed by Professor Gun-Do Lee's group from Seoul National University.

Chapter 2 is literature review which gives a detailed and systematic view of graphene properties, synthesis routes and various types of 'self-doping' defects – from simplest bond rotations to complex multivacancies and line defects. The influence of defects on

the properties of graphene and the pioneering role aberration-corrected TEM plays in imaging the lattice irregularity of two dimensional materials are also demonstrated.

The experimental details are described in Chapter 3, including the CVD synthesis of graphene, transferring onto TEM grids, AC-TEM imaging and image analysis techniques.

The use of Oxford-Jeol 2200MCO AC-TEM enables the imaging of graphene lattice with sub-Ångstrom resolution at a low accelerating voltage (80 kV). Therefore the atomic structure and dynamics of defects in graphene can be studied *via* direct imaging. In Chapter 4, interactions between dislocations and the edge of graphene are investigated. Geometric phase analysis and DFT simulation are employed to analyze the out-of-plane distortion introduced by dislocations.

A commercially available heating holder developed by DENS Solutions allows *in situ* TEM experiment performed at elevated temperatures (RT – 800 °C). In Chapter 5 – 7, the high temperature behavior of dislocations and grain boundaries in graphene are studied. In Chapter 5, the atomic structure and migration behavior of dislocations are demonstrated at different temperatures (RT, 500, 700, and 800 °C). The glide and climb motions of dislocations and their dependence on temperature are illustrated. Chapter 6 reports the *in situ* heterogeneous nucleation of graphene from Au nanoparticles at elevated temperatures in TEM. The growth mechanism and atomic structure of growth front are investigated. The as-grown graphene starts as highly polycrystalline, the crystallization of which under the combined effect of increased thermal energy and electron irradiation is also discussed. In Chapter 7, a rarely reported form of grain boundary – grain boundary loop is identified. Its full life cycle, from formation to

annihilation is demonstrated at both 500 and 800 °C, with the aim of providing insights into the stability and dynamics of high order defects in graphene at elevated temperatures.

The final chapter concludes the whole thesis and envisions possible future research as extension to this thesis.

Chapter 2

Literature Review

2.1 Introduction

Graphene is a one-atom-thick carbon allotrope with atoms tightly packed in a two-dimensional honeycomb structure. Each carbon atom is sp^2-coordinated to its three nearest neighbors with 120° bonding angles. The distance between two neighbouring carbon atoms is about 1.42 Å. The remaining π-bond of each atom is oriented along the z-axis and hybridized together to form a large π-conjugation system. Graphene is basically one single layer of graphite which is the parent material for all other graphitic carbon allotropes with different dimensionalities. It can be vertically stacked to create three-dimensional graphite, wrapped into zero-dimensional buckyballs or rolled up into one-dimensional carbon nanotubes as illustrated in Figure 2-1. Despite the fact that the theoretical model of graphene has been widely investigated in the studies of graphite, fullerenes and carbon nanotubes, it was not until 2004 Andre Geim and Konstantin Novoselov from the University of Manchester were first able to isolate monolayer graphene sheets by mechanical exfoliation from highly oriented pyrolitic graphite (HOPG). [1] Before that it has been long argued that two-dimensional crystals are thermodynamically unstable and do not exist in nature.

Since its discovery, graphene has attracted tremendous interest over the past decade from both research and industry, primarily for its exceptional electronic, chemical and

other properties. Geim and Novoselov were therefore awarded the Nobel Prize in Physics in 2010 for their groundbreaking work in two-dimensional materials.

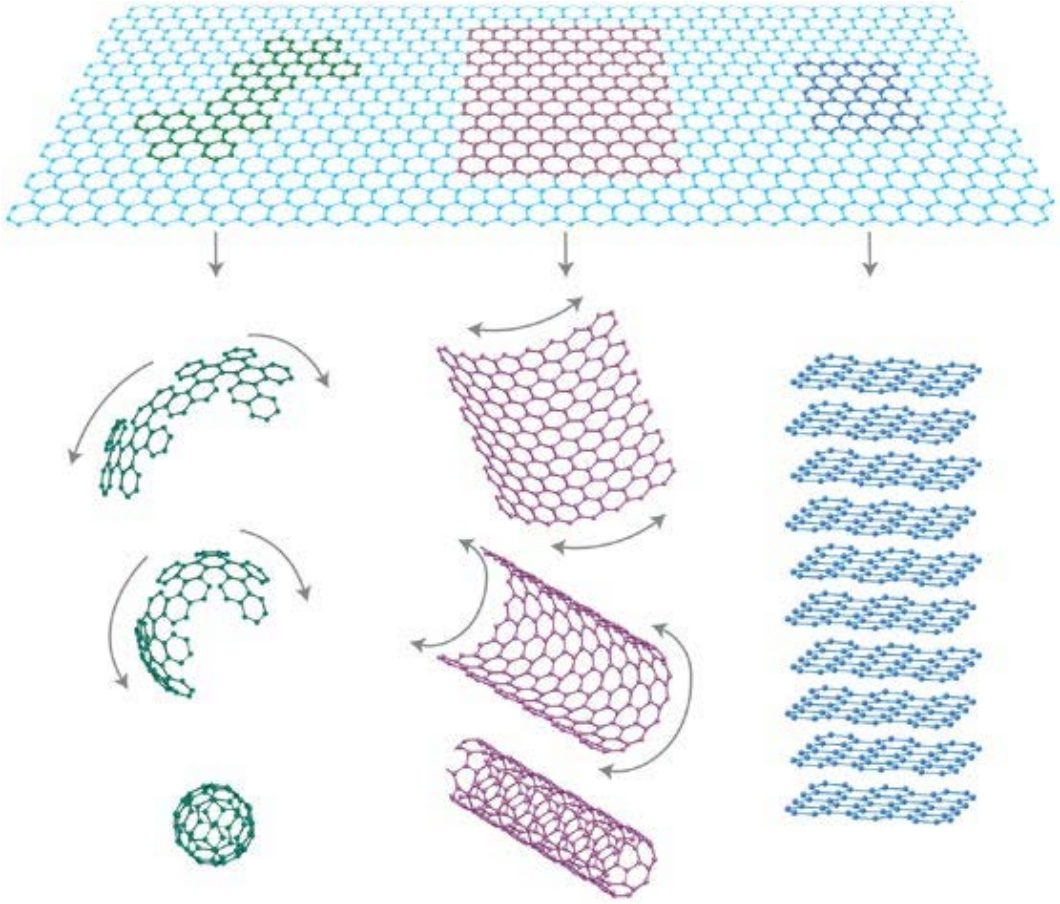

Figure 2-1. Graphene is the building block for all other graphitic material with different dimensionality. It can be wrapped into 0D buckyballs, rolled into 1D carbon nanotubes or stacked into 3D graphite. Adapted with permission from ref.[2], © 2007 Nature Publishing Group.

2.2 Properties of graphene

Graphene owns a wide range of exceptional properties and has been termed a “wonder material”. As a material with only one-atom-thickness, graphene has a high opacity of 2.3%. [3] It has an ultra-high surface-to-mass ratio of 2630 $m^2 g^{-1}$, giving its potential for energy conversion and storage. [4] In addition, it is a material far stronger than steel with an intrinsic tensile strength of 130 GPa and a Young's modulus (stiffness) of 1 TPa. [5] It also has a high thermal conductivity of ~ 2000 − 5000 W/mK near or at room temperature. [6,7] These properties has been discussed in detail in ref.[8].

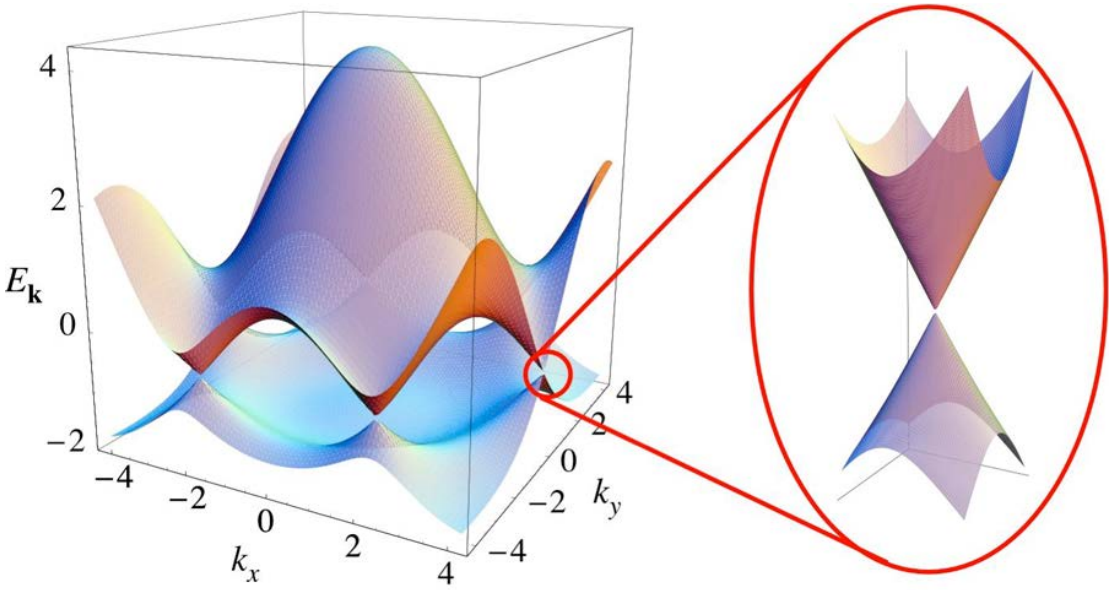

Figure 2-2. Electronic band structure of monolayer graphene, where its conduction and valence bands meet at the Dirac points. Adapted with permission from ref.[9], © 2009 American Physical Society.

Among the superior properties, the electronic properties of graphene are most intriguing. Figure 2-2 shows the electronic band structure of single layer graphene, in which conduction and valence bands touch at six points, so called Dirac points, which can be divided into two independent sets (K and K') of three points. [9] The electron

per carbon atom fully fills the conduction band and leaves the valence band vacant, which situates the Fermi level precisely at the K point. Thus, graphene can be regarded as a zero bandgap semiconductor or semi-metal. In the vicinity of the Dirac points ($|E| < 1$), the energy-momentum dispersion relation is to a large extent linear, as indicated by the inset in Figure 2-2, where electrons and holes are massless Dirac Fermions. [9–11] The Fermi velocity of electrons ~ 10^6 m/s, which enables electron to travel long distances (in the scale of micrometers) without scattering, referred to as ballistic transport. [12] Because of the unique band structure, graphene exhibits remarkably high electron mobilities at room temperature. Bolotin *et al*. (2008) reported the measurement of electron mobility in excess of 200,000 $cm^2 V^{-1} s^{-1}$ in freely suspended graphene. [13] Moreover, Novoselov *et al.* (2004) reported the experimental observation anomalous quantum Hall effect (QHE) in graphene at room temperature. [14] These properties make graphene an ideal material for both fundamental physics study and electronic industry. [15]

However, the above-mentioned exceptional properties of graphene can only be detected at an extremely low defect concentration, while the second law of thermodynamics has determined that a certain level of lattice disorder is inevitable in all crystals. Besides, it is also very difficult to avoid unintentionally introduced defects and impurities in the synthesis and transfer processes of the two-dimensional material. As a consequence, it is of significant importance to understand the structure and behavior of defects for the purpose of optimizing the electronic and other properties of graphene for specific applications.

2.3 Synthesis routes of graphene

In order to realize the full potential of graphene, it is essential to develop methods to reproducibly synthesize high quality monolayer graphene sheets. A variety of synthesis routes have been reported even since graphene was first discovered in 2004. These routes can be divided into two types: top-down and bottom-up. Top-down methods break the van der Waals forces that hold the graphite layers together and isolate few-layer graphene sheets, whereas as bottom-up approaches produce graphene from alternative carbon precursors. As the number of synthesis routes for graphene keeps growing, only four most frequently used methods are discussed in this section: 1) mechanical exfoliation; 2) chemical exfoliation; 3) epitaxial growth on silicon carbide; 4) chemical vapor deposition.

2.3.1 Top-down methods

2.3.1.1 Mechanical exfoliation

The mechanical exfoliation, also known as the 'scotch tape' or 'peel-off' method, was first reported by Geim *et al*. in 2004, which is a milestone in 2D material synthesis. [1] An adhesive tape is used to repeatedly peel off mono-, bi- and few-layer graphene sheets from the highly oriented pyrolytic graphite (HOPG). The number of layers is identified by examining the contrast of graphene flakes using an optical microscope after transferring the sample onto a SiO_2(300 nm)/Si substrate.

Compared with other methods, graphene isolated by mechanical exfoliation is of highest quality, with reported carrier mobility in excess of 15,000 $cm^2\ V^{-1}\ s^{-1}$ under ambient conditions. [2] No sophisticated instruments are involved in the synthesis process. However, graphene produced by this method has irregular shapes and is

usually at a size of several microns. Also, the synthesis process is time consuming and labor intensive. Therefore, this method is only reserved for the investigation of graphene fundamental properties.

2.3.1.2 Chemical exfoliation

In this approach, graphene is synthesized by first oxidation of graphite, exfoliation of graphene oxide (GO) and then reduction of graphene oxide (rGO). The Hummers method is most frequently used to oxidize graphene using concentrated acids and strong oxidants. [16] Although this method can be used to produce graphene in an industrial scale, the properties of rGO never match those of exfoliated graphene due to the high concentration of defects and oxygen-containing functional groups formed in the oxidation process. [17] In addition, solution processing often leads to contamination of graphene surface. Thus, chemical exfoliation is not suitable to produce graphene for electronic application or AC-TEM imaging.

2.3.2 Bottom-up methods

2.3.2.1 Epitaxial growth on silicon carbide

Early in 1962, Badami reported the graphitization of silicon carbide (SiC) during annealing at about 2000 °C in vacuum conditions. [18] Graphene grown on SiC surface typically has one to three layers, dependent on the growth temperature. [19] This process occurs due to the preferential Si sublimation under such annealing conditions. Si atoms desorb and the remaining carbon atoms rearrange themselves to form epitaxial graphene lattice. [20] The produced graphene is of relatively high quality and is especially attractive for wafer-based applications, such as electronic device fabrication.

However, the transfer of graphene from SiC is difficult due to the strong interaction between the two materials, which restricts its applications on other substrates. [21]

2.3.2.2 Chemical vapor deposition (CVD)

Chemical vapor deposition (CVD) has been extensively used to grow graphene on transition metal substrates from carbon containing gases. The growth mechanisms can be categorized as either surface catalyzed decomposition of carbon containing precursors or segregation of carbon dissolved in bulk substrates. The growth of thin graphite films by CVD was first demonstrated by John May in 1969 using Pt as substrate. [22] Somani *et al*. (2006) reported the synthesis of few layered graphene in which Ni foils and camphor were used as catalyst and substrate respectively. [23] Since then, graphene growth has been performed on a variety of transition metals such as Ni, [24–28] Cu, [29–36] Fe, [37] Ru, [38] Co, [39] Rh, [40] Ir, [41] Pd, [42] Pt, [43] and Au. [44]

Among these substrates, Ni and Cu have attracted most research attentions due to their low cost, catalytic efficiency and graphene quality. The graphene growth on Ni substrate is dominated by segregation of dissolved carbon. The solubility of carbon in Ni films is relatively high at elevated temperatures and decreases with temperature. As a result, graphene can be formed *via* the precipitation of carbon atoms on the substrate surface during the cooling process. The thickness and quality of graphene sheets strongly depend on the rate of cooling. [25,26] Besides, Ni (111) is a hexagonal lattice and has similar lattice constants with graphene, making it a perfect lattice-matched substrate for the CVD growth of graphene. [24] Nevertheless, it is difficult to produce uniform mono- or bilayer graphene on Ni substrates, as the growth process is affected

by the polycrystallinity of Ni. [27] Zhang *et al.* (2010) performed graphene CVD growth on single-crystalline Ni(111) with a smooth surface and revealed that the majority area (91.4%) is mono- or bilayer. [28]

In contrast, Cu has an ultra-low carbon solubility, which only allows limited carbon diffusion from substrate to surface. Instead, the Cu substrate catalyzes the decomposition of carbon containing species which subsequently leads to the formation of graphene on its surface. This process can be described as self-limiting, as there is no exposed Cu to facilitate further reaction after the substrate surface fully covered by the first layer graphene. As a result, most of graphene grown on Cu are mono- or bilayer. [30,31] The study of growing high quality monolayer graphene on Cu foils was originally reported by Ruoff *et al*. in 2009. [29] In their experiment, 25 μm thick Cu foils were initially annealed in hydrogen atmosphere at 1000 °C, before methane was introduced into the system as the carbon source for graphene growth. SEM images show "wrinkles" in the continuous graphene film, which originate from the difference in thermal expansion coefficients between graphene and Cu. A detailed comparative study of graphene grown on Ni and Cu has indicated that graphene on polycrystalline Ni has a lot of multilayer regions whereas graphene on Cu is a uniform monolayer sheet. [45]

However, CVD grown graphene is inevitably polycrystalline and contains a large amount of grain boundaries, which have been reported to deteriorate its transport properties. [46,47] Its quality is generally no match for the mechanical exfoliated graphene. Therefore, in order to reduce grain boundaries and increase domain size, it is crucial to control the number of nucleation sites, which are often associated with the

structural defects on the substrate surface, such as impurities, dislocations and grain boundaries. [32] It has been revealed that the pretreatment of Cu surface (*i.e.* electropolishing) helps to improve the size of graphene domains. [33,34] Geng *et al*. (2012) demonstrated that the use of liquid Cu improves graphene quality, as it eliminates grain boundaries in solid Cu and reduces potential nucleation sites. [35] This is achieved by raising the reaction temperature above the melting point of Cu (1086 °C) and using a Mo or W support foil to prevent the Cu from balling (Figure 2-3a).

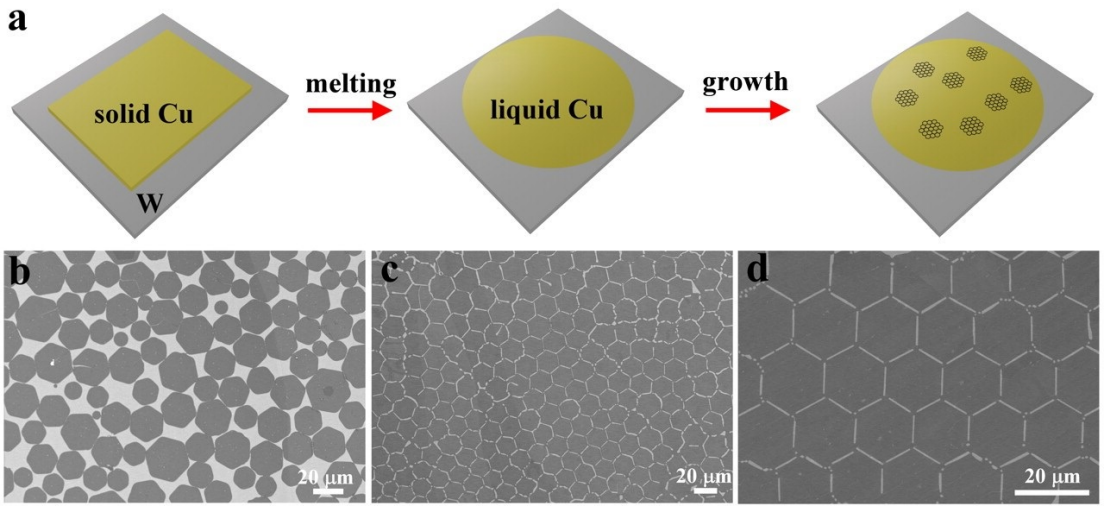

Figure 2-3. Graphene growth on melted Cu. (a) Schematic illustration showing the synthesis of graphene domains on liquid Cu surface. (b,c) SEM image showing the evolution of HGFs alignment with time. (d) A perfectly ordered graphene lattice made of HGFs with similar size. Reproduced with permission from ref.[35], © 2012 National Academy of Sciences, USA.

This approach starts with the formation of single-crystalline hexagonal graphene flakes (HGFs) which are well dispersed on the Cu surface (Figure 2-3b). The orientation of HGFs are randomly distributed. When the coverage of HGFs increases, the HGFs self-align into an ordered structure (Figure 2-3c), as the liquid nature of melted copper enables free migration and rotation of domains to minimize total surface/edge energy. Figure 2-3d shows that when the HGFs have similar domain size, a perfectly ordered

graphene lattice can be achieved. Wu *et al*. (2012) reported individual graphene domain in excess of 200 μm can be produced using this method. [36]

2.4 High resolution transmission electron microscopy of graphene

It has always been challenging to directly image the structural defects in bulk crystals even with the state-of-the-art microscopes. As most of the defects are buried deep inside materials, delicate sample preparation methods have to be developed to gain access to the defects in the inner side. The structure of graphene is well exposed due to its two-dimensional nature, making it a perfect candidate for microscopy studies. Therefore, the graphene lattice can be studied in more detail, even in atomic spatial resolution by various experiment techniques, although most techniques are originally developed for the structural study of bulk crystals.

Scanning tunneling microscopy (STM), scanning transmission electron microscopy (STEM) and transmission electron microscopy (TEM), have all been extensively applied in imaging the structural irregularity in graphene and other two-dimensional materials, such as hexagonal boron nitride (h-BN) and transition metal dichalcogenides [(TMDCs) MX_2 (M = Mo, W; X = S, Se)]. Atomic force microscopy (AFM) and scanning electron microscopy (SEM) can also provide useful information in analyzing the lattice disorder in two-dimensional materials, but lack enough spatial resolution to resolve the atomic structure of individual point defects. [48]

STM is an instrument for surface imaging at the atomic scale, based on the concept of quantum tunneling. A bias voltage is applied between the sample and the scanning tip

several Ångstrom above. The information of the surface configuration is acquired by moving the fine tip across the sample and measuring the tunneling current flowing through it. A spatial resolution of ~ 100 pm can therefore be achieved. However, the tunneling current is affected by not only the position of atoms from the sample but also the local electronic structures, which makes the interpretation of STM images not straightforward. [49]

Conventional TEMs have long been used to the characterize lattice deformation in crystals. In 1956, Sir Peter Hirsch and his collogues were the first to report the observation of dislocation movements in aluminum using 100 kV TEM. [50] Since then, techniques for high resolution TEM imaging have experienced an impressive growth. In about 1970, a spatial resolution of ~ 0.3 nm could be achieved. [51] The advance was made by improving the electronic and mechanical stabilities and reducing the aberrations. In the 70s, TEM began to be applied in imaging the grain boundaries in various kinds of materials (*i.e.* metallic oxides, metals and semiconductors), [52–54] as it provides straightforward lattice information in atomic scale. In recent years, monochromators have been developed to limit the beam energy spread within ~ 0.21 eV. With advances in further reducing the spherical aberration, a resolution of under 80 pm can be achieved in the state-of-art HR-TEM. [55,56]

Over the last 20 – 30 years, the scanning transmission electron microscope (STEM) has been developed as a powerful tool to resolve the atomic structure of crystals. It is a special type of TEM operated by focusing the electron beam into a small probe (~ 0.1 nm) and using it to raster-scan over the specimen. [57] The lattice structure is imaged by collecting the signal with a high-angle angular aperture, which corresponds to both

the atomic number and the surface configuration of the specimen. Modern aberration-corrected STEM also produces sub-Ångstrom resolution images.

Compared with STM and STEM, the TEM system has its unique strength in resolving the atomic structure of graphene. Imaging graphene in STM requires a substrate to support the specimen, while (S)TEM can be used to investigate freely suspended graphene. The interpretation of STM results is also less straightforward than that of (S)TEM. STEM is a powerful tool for the structural study of materials composed of two or more elements such as TMDCs since the contrast in STEM images is directly related to the atomic number (Z-contrast technique). However, it has not evident superiority over TEM in the studies of graphene, especially the 'self-doping' defects (*i.e.* no involvement of foreign atoms). In addition, the monochromator which greatly reduces the beam energy spread cannot be applied in the STEM system.

Despite the advantages, TEM imaging inevitably leads to electron irradiation onto the specimen surface, which cannot be neglected especially for materials made of light elements such as carbon nanotubes, fullerenes, graphene and boron nitride. [58–64] The displacement threshold energy (T_d) is used to describe the irradiation hardness of a material. T_d is defined as the minimum kinetic energy that has to be transferred to an atom in a ballistic knock-on event for it to leave its original lattice site and then either occupy an interstitial position or leave the system without any form of recombination. In the case of graphene, the minimum energy to sputter a saturated carbon atom is approximately 22 eV. [65,66] Egerton *et al*. (2004) suggested that the maximum energy that can be transferred to a carbon nucleus from an 80 keV electron in graphene is 15.7 eV, well below T_d. [58] However, Meyer *et al*. (2012) experimentally demonstrated

that under 80 kV electron irradiation carbon can still be sputtered from pristine graphene lattice, although the possibility is rather small. [66] They have also indicated that this low accelerating voltage does not prevent the displacement of under-coordinated atoms and the beam-driven chemical etching. The removal of a carbon atom from graphene lattice leads to the formation of a monovacancy leaving an atom undercoordinated (See Section 2.5.1.2 in this chapter for details). The minimum energy to sputter this unsaturated atom is only 14.7 eV. [67] As a result, once a hole is opened up in the graphene sheet, one would expect the atoms on the edge be continuously etched by the knock-on damage under 80 kV electron irradiation. However, Meyer *et al*. argue that chemical etching is the dominant mechanism in opening up holes in graphene by showing the TEM results that holes rapidly grow with foreign atoms (probably Si) attached to the open edges. [66]

On the other hand, defects can also be intentionally introduced to graphene by electron irradiation for the purpose of tailoring its properties. [68–72] Focused electron beam in (S)TEM has long been used to introduce vacancies and holes in carbon nanomaterials, but the control of defect formation with nanoscale precision is always challenging. [68–70] Robertson *et al*. (2012) reported a method to controllable create defects in graphene by focusing the beam within a 10-nm spot (beam current density ~ 10^8 *e* nm^{-2} s^{-1}) for a certain period of time. [73] Then the beam was expanded (~ 10^5 *e* nm^{-2} s^{-1}) to image the graphene lattice after defect formation. By precisely controlling the exposure time from 30 – 120 s, they managed to create a wide range of point defects.

2.5 ‘Self-doping’ defects in graphene

Defects without the presence of foreign atoms are referred to as ‘self-doping’ or ‘intrinsic’ defects. Intrinsic defects in bulk crystals can be classified as zero-, one- and two-dimensional ones. Point defects including vacancies and interstitial atoms are zero-dimensional. Dislocations are one-dimensional line defects in 3D crystals. Stacking faults and grain boundaries are two-dimensional defects. In graphene, due to the reduced dimensionality, these defects plays a quite different role. Only point defects (0D) and line defects (1D) can be found in graphene. In addition, when carbon atoms are removed from or added to the graphene lattice, the strong sp^2-hybridized atom network has the ability rearrange itself to form non-hexagonal polygons (*i.e.* pentagons, heptagons and octagons). Similar to those in bulk crystals, defects in graphene introduce negligible curvature and strain in the surrounding lattice, and sometimes even lead to changes in the local electronic, magnetic or chemical properties. Thus, understanding the stability and behavior of these defects could provide inspiration to develop graphene-based devices and sensors.

2.5.1 Point defects

2.5.1.1 Stone-Wales defect

The Stone–Wales (SW) defect is named after Anthony Stone and David Wales from Cambridge University who reported this defect in their work on the isomerization of fullerene in 1986. [74] It is a crystal defect which can be created by rotating a C–C bond by 90° around the middle point of the bond, converting four adjacent hexagons into two pentagons and two heptagons as illustrated in Figure 2-4. Such a transformation is referred as a SW transformation or a SW bond rotation.

The kinetic barrier for this process is calculated to be 9 – 10 eV (Figure 2-4c), [75,76] which is significantly higher than the thermal fluctuation of graphene lattice at room temperature, making the spontaneous transition nearly impossible. However, despite a low frequency of occurrence, it is still possible to observe SW defects in a TEM operated at a low accelerating voltage, which are activated by sub-threshold collision between electrons and carbon nuclei. The formation energy for a SW transformation is about 5 eV, which is the lowest energy defect among all point defects in graphene. [76] This means the minimum energy for a SW rotation to reverse back is ~ 5 eV, which would require another sub-threshold collision and thus its stability after transition is guaranteed.

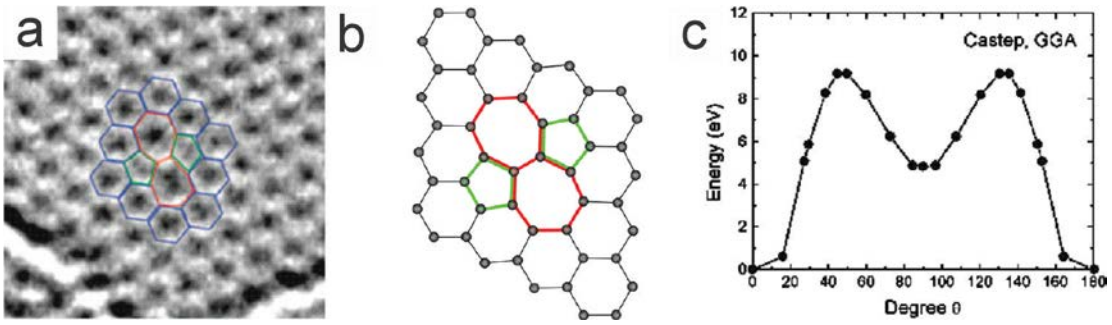

Figure 2-4. Stone-Wales defect. (a) HR-TEM image of a Stone-Wales (SW) defect formed by rotating a C–C bond by 90°. Reprinted with permission from ref.[77], © 2008 American Chemical Society. (b) DFT calculated atomic structure of a SW defect. Adapted from ref.[78], © 2011 American Chemistry Society. (c) Calculated energy barrier of the bond rotation as a function of rotated angle. Reproduced from ref.[76], © 2005 American Physical Society.

Peng and Ahuja (2008) reported that the SW defect in monolayer graphene opens a band gap of 0.25 eV, which makes it a potential candidate for defect nanoengineering of the local band structure. [79] Ma *et al*. (2009) studied the SW rotation using density functional theory and quantum Monte Carlo simulations and predict that instead of the

simple in-plane rotation of a C–C bond, a SW transformation involves long range out-of-plane displacement extending over several nanometers. [75] Also, multiple SW rotation possibilities in large vacancy structures greatly complicate their configurations, which will be discussed in more detail in the divacancy (2.5.1.3) and multivacancies (2.5.1.4) sections below.

2.5.1.2 Monovacancy

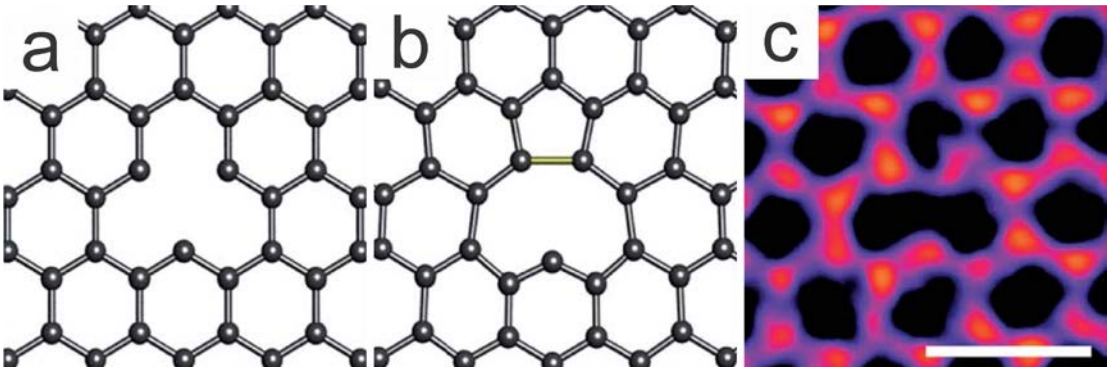

Figure 2-5. Monovacancy in graphene. (a) Atomic model of a pristine graphene lattice with one carbon atom missing. (b) Atomic model of the structure in (a) gone through a Jahn-Teller distortion, accompanying AC-TEM image shown in (c). The scale bar in panel c is 0.5 nm. Reprinted with permission from ref.[80], © 2013 American Chemical Society.

Monovacancy (MV), also called single vacancy, is the simplest form of vacancy in all materials. It has been experimentally observed in graphene, CNTs and graphite using both STM and TEM. [77,80–82] A MV in these carbon allotropes is formed *via* the removal of one single carbon atom from the lattice, leaving three dangling bonds as illustrated in Figure 2-5a. First principle calculations show that it can further go through a Jahn–Teller distortion, yielding the bond reconstruction between two of the three under-coordinated carbon atoms and the formation of a closed 5- and a 9-membered rings (Figure 2-5b). [83–88] El-Barbary *et al.* (2003) reported that Jahn–Teller

distortion gives a ~ 0.2 eV lower energy and small out-of-plane displacements. [88] According to their calculation, the remaining under-coordinated carbon is moved out of the plane by $\Delta z \sim 0.5$ Å due to an increase in the local density of states at the dangling bond. This result is also confirmed by the STM experiment. In STM images the MV shows up as a protrusion. [81] The formation energy of a MV in graphite is ~ 7.5 eV calculated by DFT, [88,89] much higher than that in silicon (~ 4 eV) and most metals (< 4 eV), [90,91] which is expected due to the presence of the under-coordinated atom. The formation energy of a MV in graphene (graphite) is also higher than that in CNT, since the curvature in CNT breaks the trigonal symmetry of the honeycomb lattice and lead to selective saturation of two of the three dangling bonds with lowest energy.

Robertson *et al.* (2013) characterized MVs in monolayer graphene using Oxford's state-of-the-art AC-TEM equipped with a monochromated beam source. [80] The unprecedented sub-Ångstrom spatial resolution enables them to determine whether the MV is symmetric or reconstructed by bond length measurement in TEM images. They have also quantitatively measured the lattice strain and displacement around both MV configurations using geometric phase analysis (GPA) and prove that Jahn–Teller reconstructed MV gives rise to extra strain compared to the symmetric one. Theoretical study suggests that the migration of MVs takes place by switching one of the edge atoms to the opposite site and thus shifting the vacancy to a neighboring position. [88,89] This has also been experimentally observed by Robertson *et al.* in their TEM research. The migration energy for a MV in graphene is calculated to be ~ 1.5 eV, which can be easily reached under low accelerating voltage electron irradiation in a TEM or at temperature above 100 °C. [88,89]

MVs in graphene are found to introduce local magnetic moment and lead to a dramatic decrease in the mobility of charge carriers. [81] DFT and TMBD simulations indicate that the magnetic moment of a MV is about 1.10 μ_B. [86,92,93] It has also been suggested that the MV may act as the potential doping site for light foreign atoms such as B and N, while the doping of heavy atoms (Pt, Co and In) require higher order vacancies. [94]

2.5.1.3 Divacancy

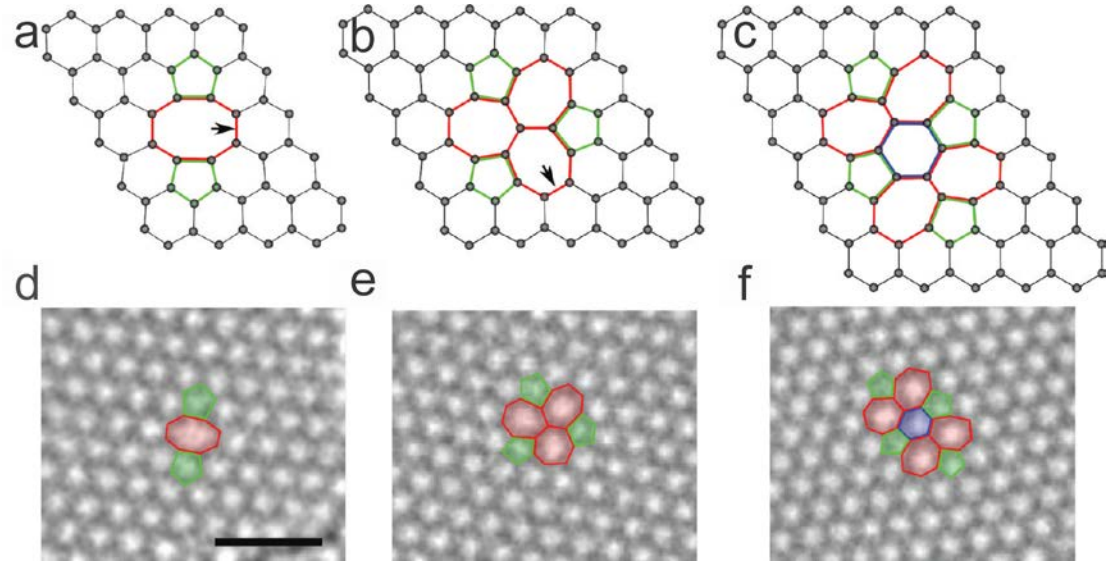

Figure 2-6. Divacancies in graphene. Atomic models of (a) a DV1 (5-8-5), (b) a DV2 (555-777) and (c) a DV3 (5555-6-7777), with their corresponding HR-TEM images shown in (d–f) respectively. Bonds to be rotated in the next frame are highlighted by the black arrows. The scale bar in panel d is 1 nm. (a–c) Adapted with permission from ref.[78], © 2011 American Chemistry Society. (d–f) Reprinted from ref.[95], © 2011 American Physical Society.

Divacancy (DV), also known as double vacancy, is the most frequently observed vacancy structure in the AC-TEM inspection of graphene. It can be created by removing a pair of neighboring atoms from graphene lattice or by the combination of two MVs.

In Figure 2-6d an AC-TEM image of a fully reconstructed DV is shown. The removal of two carbon atoms yields a pentagon-octagon-pentagon [DV_1 (5-8-5), Figure 2-6a and d] sequence with no dangling bond. However, it is not the only configuration of a DV. Figure 2-6b and c show that it could reconstruct into two more complex structures *via* a series of SW bond rotations under electron irradiation. The SW rotation of the highlighted C–C bond in Figure 2-6a leads to the transformation from the DV_1 (5-8-5) to a defect structure made of three pentagons and three heptagons [DV_2 (555-777)]. The TEM image of a DV_2 and accompanying atomic model are shown in Figure 2-6b and e. DV_2 (555-777) is the most energetically favored among all three DV configurations, with its formation energy ~ 1 eV lower than that of a DV_1 (5-8-5). [88] A second bond rotation highlighted by the black arrow in Figure 2-6b further transforms the DV_2 to a DV_3 (5555-6-7777) defect (Figure 2-6c and f). The central hexagon in the DV_3 (5555-6-7777) is rotated by 30° with respect to the perfect graphene lattice. [96–98] DFT calculation suggests that the formation energy a DV_3 (5555-6-7777) defect lies between those of DV_1 (5-8-5) and DV_2 (555-777). Qu *et al.* (2015) revealed that the bond rotations that convert DV_1 to DV_2 and DV_3 help distribute the lattice mismatch strain over more C–C bonds. [99]

The formation energy of all three DVs is about 8 eV according to DFT calculation, which is in the same magnitude as that of MV. [88,89] This is understandable since the minimum energy required to sputter the under-coordinated carbon atom in a MV is ~ 14 eV, significantly lower than the sputtering threshold for pristine graphene lattice (~ 22 eV). [60,100] Therefore one can expect a MV to quickly convert into a DV under electron beam irradiation. DVs in graphene are extraordinarily stable as all carbon

atoms are saturated. The migration barrier for a DV is ~ 7 eV which is also higher than that of a MV (~ 1.5 eV) making DVs highly immobile at room temperature. [88] Kotakoski et al. (2014) performed prolonged STEM imaging of DVs in graphene with a high beam current density (~ 10^9 *e* s^{-1} nm^{-2}) at 60 kV and found that the random walk of a DV is done by switching between configurations, such as DV_1 (5-8-5) → DV_2 (555-777) → DV_1 (5-8-5) and DV_2 (555-777) → DV_3 (5555-6-7777) → DV_2 (555-777). [101]

2.5.1.4 Multivacancies

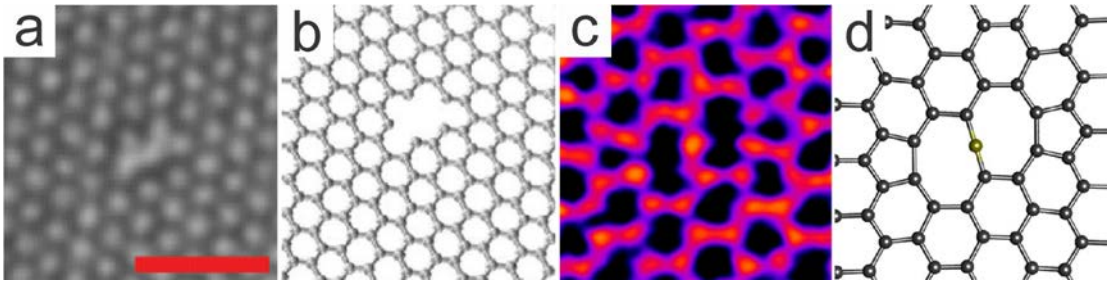

Figure 2-7. Trivacancies in monolayer graphene. (a) AC-TEM image of a trivacancy (U-trivacancy) created using high velocity ions bombardment. (c) AC-TEM image of a bridging atom stabilized trivacancy (B-trivacancy). (b,d) Atomic models of TEM images shown in (a) and (c) respectively. The scale bar in panel a is 1 nm. (a,b) Reprinted with permission from ref.[69], © 2009 American Chemistry Society. (c,d) Reproduced from ref.[102], © 2014 American Chemistry Society.

The atomic configurations for vacancies with more than two adjacent carbon atoms missing, such as trivacancies and tetravacancies, are much more complicated, as bond rotations can give rise to a large number of possible structural variations. In general, vacancies with even number of carbon atoms removed (V_{even}) always allow full saturation of all under-coordinated atoms, while there is at least one dangling bond in vacancies with odd number missing carbon atoms (V_{odd}). Because of the instability of

under-coordinated sp^2 carbon atoms, V_{even} defects are more energetically favorable over the V_{odd}. [103] Dai *et al.* (2011) demonstrated that the dangling bond in the V_{odd} introduce magnetism and the unpaired *2p* electron of carbon atom plays a pivotal role in the formation of magnetic moment, derived from first-principle simulations. This result indicates that ferromagnetic coupling is present between carbon atoms in V_{odd} defects. [104]

Large vacancy structures can be artificially introduced to graphene sheets by high energy ion/atom bombardment or electron beam irradiation. Rodriguez-Manzo and Banhart (2009) reported a method which could be used to create trivacancies in single- and double-walled carbon nanotubes using strongly focused electron beam in a STEM. [69] Wang *et al.* (2012) were also able to generate trivacancies (Figure 2-7a) in monolayer graphene *via* high-energy gold ion/atom bombardment. [94] However, Robertson *et al.* (2014) pointed out there is another configuration of trivacancy (Figure 2-7c, B-trivacancy) consisting of two pentagons, two octagons and an under-coordinated carbon atom in the central bridging position. [102] The defect is generated by focusing the electron beam within a nanoscale region to significantly increase the beam current density in a TEM operated at 80 kV. The bridging atom, which help stabilize the B-trivacancy, can also be found in higher (>3) order odd-numbered vacancies under TEM observation. [102] No U-trivacancy defect was observed in their experiment which can be attributed to the difference in defect creation methods. DFT calculation indicates that the B-trivacancy exhibits a magnetic moment (1.92 μ_B) remarkably higher than that of a U-trivacancy (1.02 – 1.04 μ_B). [105,106]

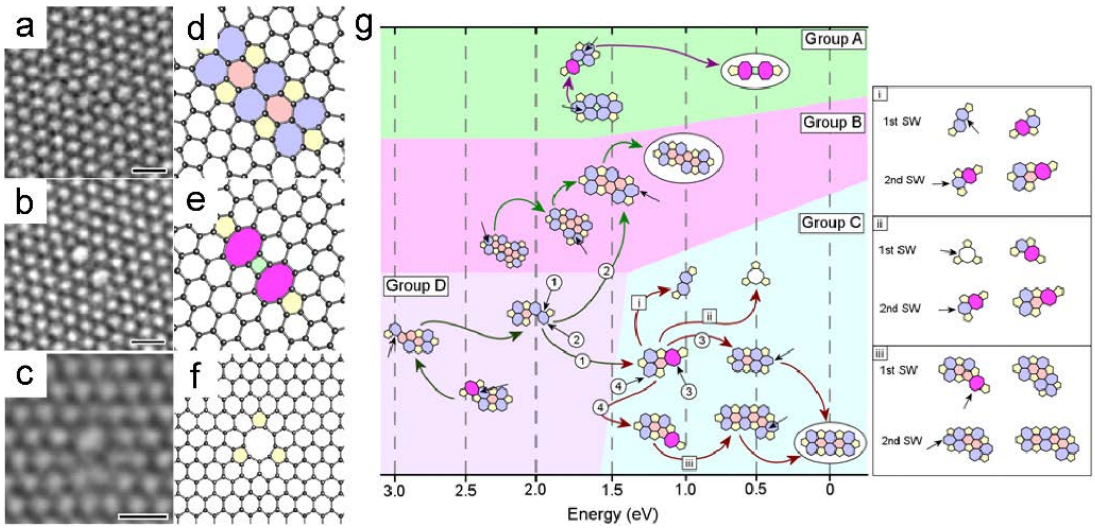

Figure 2-8. Tetravacancies in graphene. (a–c) Smoothed AC-TEM of two most frequently observed tetravacancies and a Y-tetravacancy, along with (d–f) the accompanying atomic models. The scale bar in all images is 0.5 nm. (g) Pathways showing how SW bond rotations in tetravacancies lead to the most frequently observed configurations in the circle. Unannotated colored arrows suggest indicate that the transformation requires a single bond rotation. Colored arrows with Roman numerals indicate that transformation require two SW rotations which are shown in the right-sided panels. The bonds are highlighted with black arrows. The formation energy of all defect structures is calculated by DFT method. (a–g) Reproduced with permission from ref.[107], © 2014 American Chemistry Society.

Tetravacancies in graphene exhibit even more configurations. Robertson *et al.* reported the observation of 17 different types of tetravacancies in graphene (corresponding atomic models shown in Figure 2-8g) generated by exposing the sample to the focused electron beam for a certain period of time. [107] Figure 2-8a and b show the two most frequently occurred configurations of tetravacancy defects. The Y-tetravacancy (Figure 2-8c) which is frequently modelled in literatures, however, is rarely observed in their experiments. The variety of tetravacancy configurations is mainly due to the large number of C–C bonds in the defect which could undergo a SW bond rotation. Figure 2-8g shows the paths by which various tetravacancy structures relax to the

configuration with lower energy and finally reach the most frequently observed structure (circled) *via* bond rotations. It has been indicated that a tetravacancy is more likely to rotate backwards to a lower energy state, as the energy required for a SW relaxation is less than that for another SW rotation to a higher energy state.

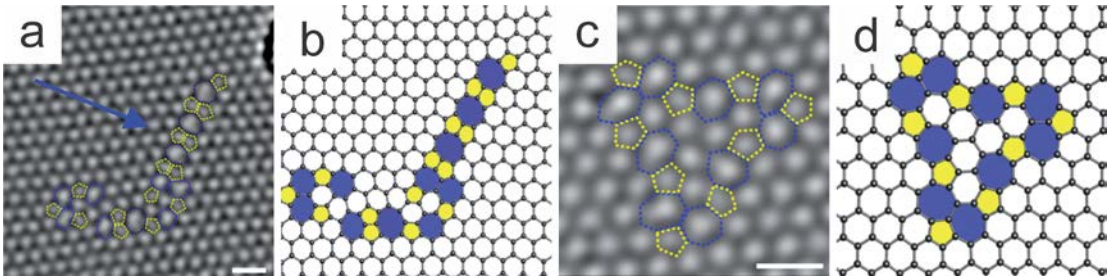

Figure 2-9. Multivacancies assembled by several divacancy defects. (a) AC-TEM images of a large vacancy including an extended zigzag chain of divacancies indicated by the blue arrow. (c) AC-TEM image of a closed loop assembled by three (5555-6-7777) divacancies. (b, d) Atomic models of TEM images shown in (a) and (c) respectively. Scale bars in all images are 0.5 nm. (a–d) Reproduced with permission from ref.[108], © 2013 The Royal Society of Chemistry.

Compared with divacancies, trivacancies and tetravacancies are far less frequently observed in the TEM inspection of defects in graphene. To date, studies on the graphene vacancy structure with five or more neighboring atoms missing have not yet been systematically reported. In most cases, the multivacancy generated after prolonged exposure of electron beam inside the TEM are the assembly of divacancies. Figure 2-9 shows the TEM images and corresponding atomic model of an extended zigzag divacancy chain (Figure 2-9a) and a closed divacancy loop (Figure 2-9b) in monolayer graphene. [73] The extended zigzag carbon chain defect has been suggested to exhibit the band structure of a one-dimensional metallic wire embedded in the graphene sheet. [109,110] The closed pentagon-heptagon loop in Figure 2-9c can be regarded as the assembly of three (5555-6-7777) divacancies. DFT calculations reveal

that the formation energy per missing atom for the loop defect is significantly lower than those of the other defect structures with six carbon atoms lost. [111] However, experimental results demonstrate that if a large number of carbon atoms are simultaneously removed from a small region in graphene (*i.e.*, by energetic ion bombardment), it is more likely to form a hole with unsaturated bonds around its circumstance. [95] Another way to reconstruct defective graphene is to form a pair of edge dislocations, which will be discussed hereinafter.

2.5.1.5 Sub-nanometer pores

Very recently, Robertson *et al.* (2015) demonstrated the atomic structure of subnanometer pores in graphene by *in situ* high temperature experiments in an AC-TEM. [112] Figure 2-10 identifies several types of subnanometer pores that have been experimentally observed with the number of lost carbon atoms ranging from 6 to 13. However, these pores have been reported to have an extremely low frequency-of-occurrence, since there are alterative, more generically favored configurations. It has also been indicated that subnanometer pores may only exist at elevated temperatures and under vacuum condition.

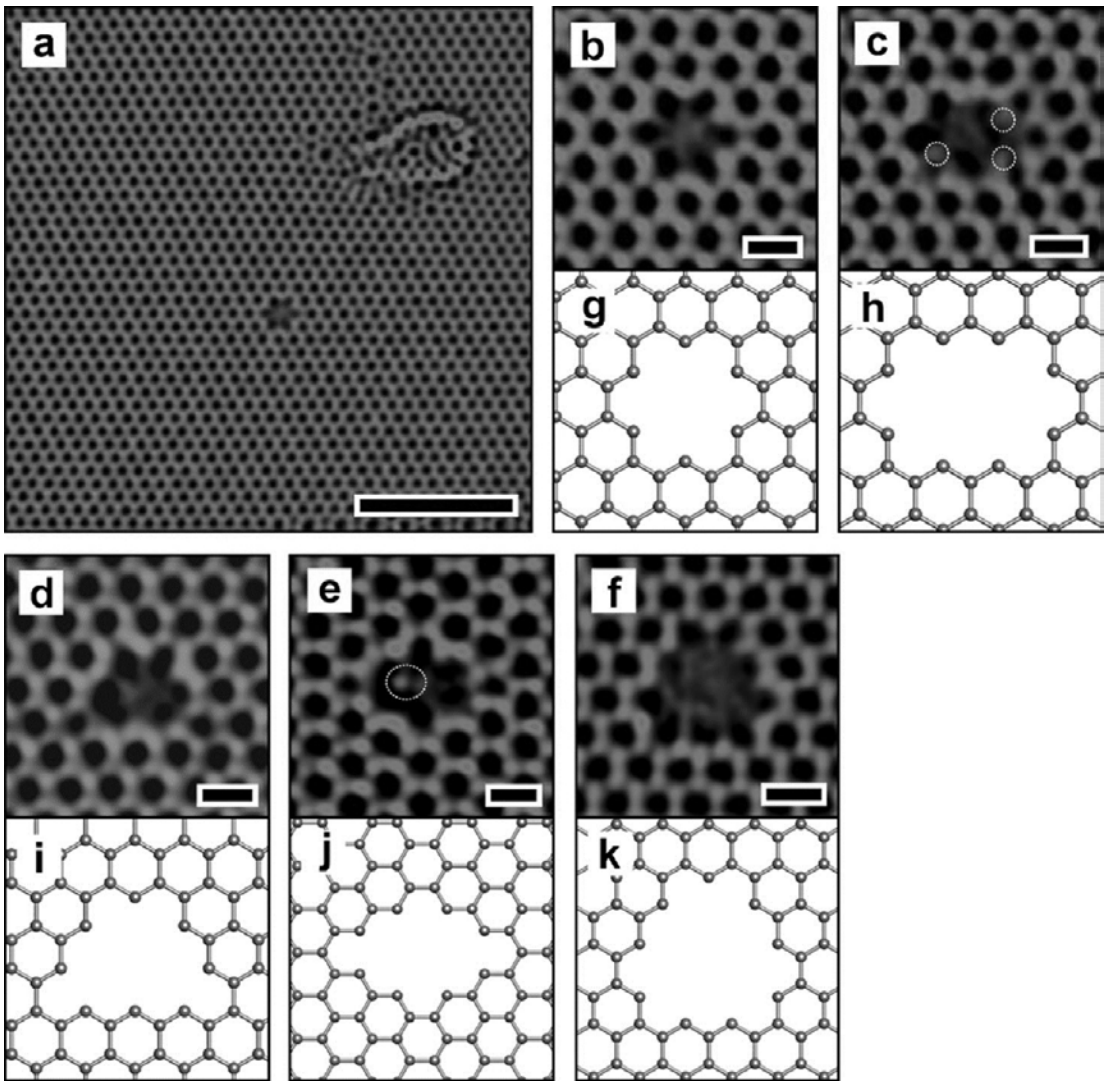

Figure 2-10. Subnanometer pores in graphene. (a) A low magnification AC-TEM image of a subnanometer pore with 6 atoms missing. (b–f) High magnification AC-TEM images of five different subnanometer pores. (g–k) Accompanying atomic models. Dashed circles highlight possible mobile atoms inside the pores. Scale bars are 2 nm in panel a and 0.2 nm in other panels. Adapted with permission from ref.[112], © 2015 American Chemistry Society.

2.5.1.6 Adatom and excess-atom defects

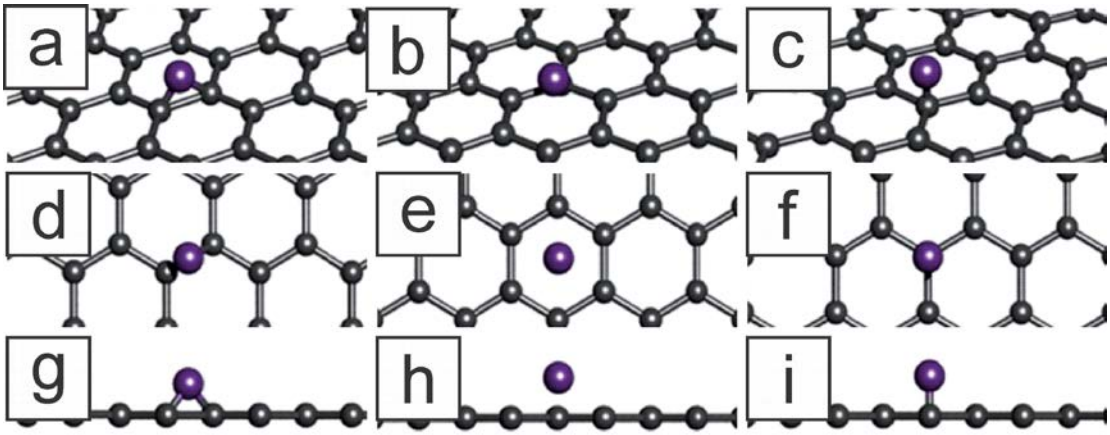

Figure 2-11. Perspective (a–c) above (d–f) and side (g–i) views of atomic models illustrating three kinds of possible adatom (blue atom) position: (a,d and g) the bridge site (B), (b,e and f) the hollow site (H), and (c,f and i) top site (T). Reproduced with permission from ref.[108], © 2013 The Royal Society of Chemistry.

Interstitial atoms in graphene and other 2D materials always occupy a third dimension, as the energy barrier to place an extra atom into the 2D plane is extremely high. There are practically three high symmetry sites for carbon adatoms on graphene lattice: bridge (B), hollow (H) and top (T), all shown in Figure 2-11a–c respectively. The bridge is the energetically favored position among the three sites, with the formation energy of top site and hollow site being 0.22 eV and 0.37 eV higher respectively. [113] When a carbon adatom interacts with a pristine graphene layer, some sp^2 C–C bonds may switch to sp^3-hybridization and get out-of-plane bonded with the adatom. The calculated binding energy of a carbon adatom on bridge site is 1.2 – 1.8 eV. [114] Lehtinen *et al.* (2003) demonstrated that the carbon adatom on graphene introduces a magnetic moment of about 0.5 μ_B. [115] They have shown that the *ab initio* calculated migration barrier for a carbon interstitial is 0.4 eV, which means the single carbon adatom is highly mobile on the graphene sheet at room temperature and is difficult to capture using TEM.

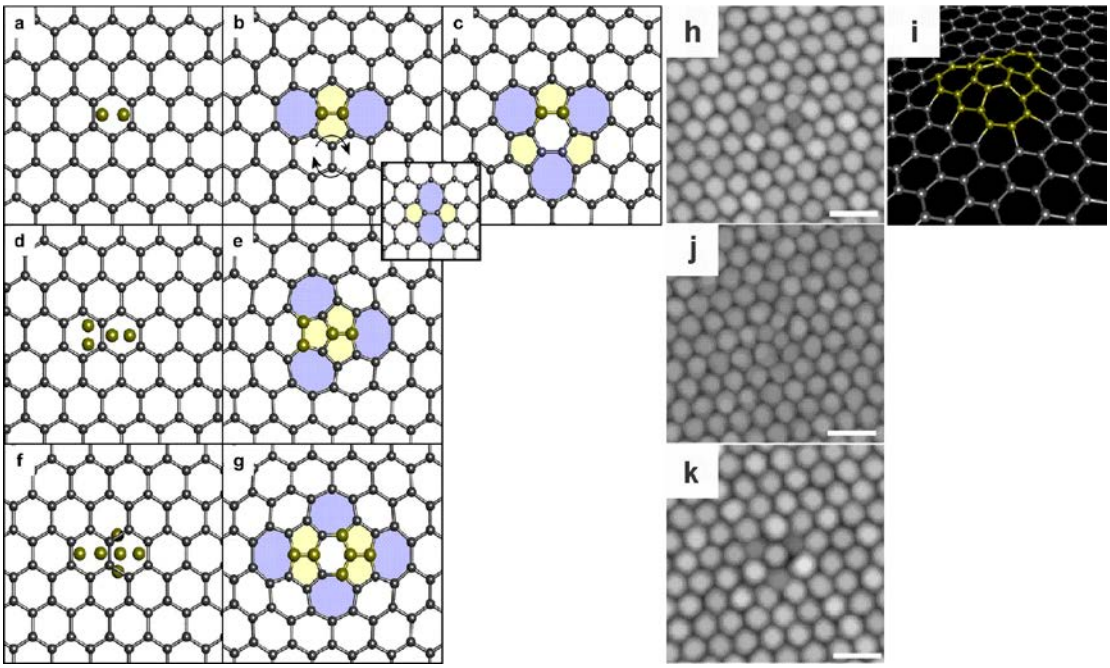

Figure 2-12. Excess-carbon atom defects in graphene. (a) Atomic models showing two carbon adatoms located on a pristine graphene layer, before reconstructed into the ISW defect (b). The inset panel in (b) illustrates a SW rotation. (c) A further bond rotation indicated by the black arrows in (b) results in the formation of a C_2 defect. (d) Four carbon adatoms reconstructed into a C_4 defect in (e). (f) Six carbon adatoms reformed into a C_6 defect in (e). All carbon adatoms are highlighted in yellow. (h–k) Maximum filtered AC-TEM images corresponding to the C_2, C_4 and C_6 defects in (c, e and g) respectively with scale bars being 0.5 nm. (i) Perspective view of DFT calculated atomic model of a C_2 defect. (a–i) Reproduced with permission from ref.[116], © 2014 American Chemistry Society.

If two carbon adatoms are successively incorporated into the graphene lattice, a 7-55-7 configured defect can be generated. This defect consisting of two pentagons and two heptagons is termed as an inverse Stone-Wales (ISW) defect, since its configuration is the inverse version of 5-77-5 Stone-Wales (SW) rotation (inset in Figure 2-12b). [72,117–120] DFT calculations show that the formation energy of an ISW defect is 6.2 eV, higher than that of a SW rotation (5 eV). A further step of bond rotation could transform the ISW defect into a 3-fold symmetry defect shown in Figure 2-12c. Here,

C_x is used to define the reconstructed excess-atom defect containing x additional atoms, while a C_2 defect is defined only to refer the configuration in Figure 2-12c rather than an ISW defect (Figure 2-12b). The formation energy of a C_2 defect calculated by DFT is 6.07 eV which is slightly lower than that of an ISW defect. The C_2 (555-777) (Figure 2-12h) defect was observed by Robertson *et al.* (2014) using an AC-TEM operated at a low accelerating voltage of 80 kV, along with the C_4 (555-777) (Figure 2-12j) and C_6 (5555-7777) (Figure 2-12k). [116] They have revealed that these defect are highly immobile and the added carbon atoms would be quickly sputtered (less than 2 min) under electron irradiation. The excess-atom defects shown in Figure 2-12 introduce local out-of-plane distortion and generate hillocks, as demonstrated by the DFT optimized atomic model in Figure 2-12i. [121] Although it has been proposed that these defects can be used to tailor the electronic properties of graphene, [72,120] their instability and short lifetime would make it a great challenge.

2.5.2 One-dimensional defects

2.5.2.1 Dislocation

Dislocations are practically one type of line defects which play a crucial part in determining the strength of a material. The first concept of dislocation was proposed in the beginning of 20th century for the purpose of explaining the plasticity of materials in microscopic scale. Since then numerous research efforts have been devoted into this field. Analogy to their role in bulk crystals, dislocations strongly affect the elasticity and plasticity of graphene. [122–124] In bulk materials the real-time monitoring of dislocations at the atomic level is restricted by the spatial and temporal resolution limits of current characterization techniques. Graphene serves as a perfect candidate for AC-

TEM characterization due to its two-dimensional nature. Sub-Ångstrom resolution can be achieved in the state-of-the-art AC-TEM which is sufficient to resolve each single carbon atom. The study of dislocations in graphene provides a perspective in improving the theoretical understanding of how dislocation affects the mechanical properties of crystals. [125]

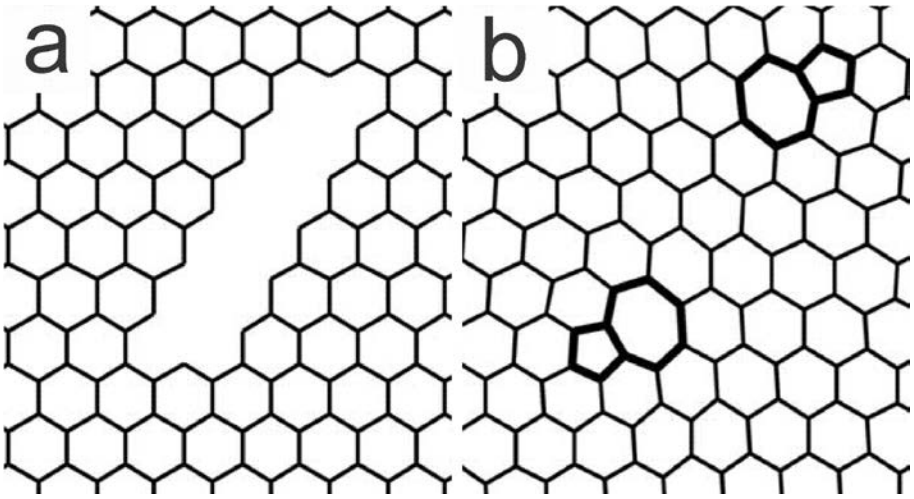

Figure 2-13. Schematic atomic models illustrating the formation of a pair of dislocations. (a) Monolayer graphene sheet with a zigzag chain of carbon atoms removed, which subsequently transformed into a pair of pentagon-heptagon dislocation cores, shown in (b) *via* sp^2-bond reconstruction. Adapted with permission from ref.[125], © 2012 American Association for the Advancement of Science (AAAS).

Because of the decreased dimensionality, screw dislocations which involve the interaction between layers do not actually exist in graphene and only edge dislocations can be found. [125] Figure 2-13 schematically illustrates the initial and relaxed geometry of a graphene sheet with a zigzag chain of carbon atoms removed. The full saturation of dangling bonds in the initial geometry leads to the formation of a pair of pentagon-heptagon defects. The pentagon-heptagon configuration is the most commonly reported (1, 0) dislocation core, which adds a row of atoms along the

armchair axis. Similar conclusions can be reached if an armchair chain of carbon atoms is removed. In theory, a pair dislocation can also be generated with zero density deficit by separating the two pentagon-heptagon defects in a SW defect. Yazyev and Louie (2010) found that the formation energy increases with the distance between two dislocations and approaches a constant value, 6.17 eV for a single dislocation. [123] This values is in the same order with those of simple point defects, such as SW rotations (5 eV) and monovacancies (7.5 eV).

The direct observation of dislocations using TEM was first achieved in the 1950s. Despite the low spatial resolution at that time, it is undoubtedly one of the most important discoveries made by TEM in the past century. [50,51] In 1969, Cockayne *et al.* introduced the weak beam method in TEM which enables them to determine the position of dislocation lines with more accuracy. [126] Since then the TEM has been extensively applied in imaging the structure and arrangement of dislocations. [127]

TEM operated at a low accelerating voltage has been long used to resolve the lattice structure of graphitic nanomaterials. [77,95,128–135] First TEM studies of dislocations in graphite were reported in the early 1960s. [136,137] In 1966, Roscoe and Thomas built an atomic model of tilt-grain boundaries in graphite and proposed that the edge dislocation consists of pentagon-heptagon pairs. [138] Hashimoto *et al.* (2004) demonstrated that edge dislocations can be created in graphene layers when exposed to the electron irradiation. [128] However, the lack of aberration-corrector and monochromator prevented further imaging the atomic configuration of dislocations in graphene.

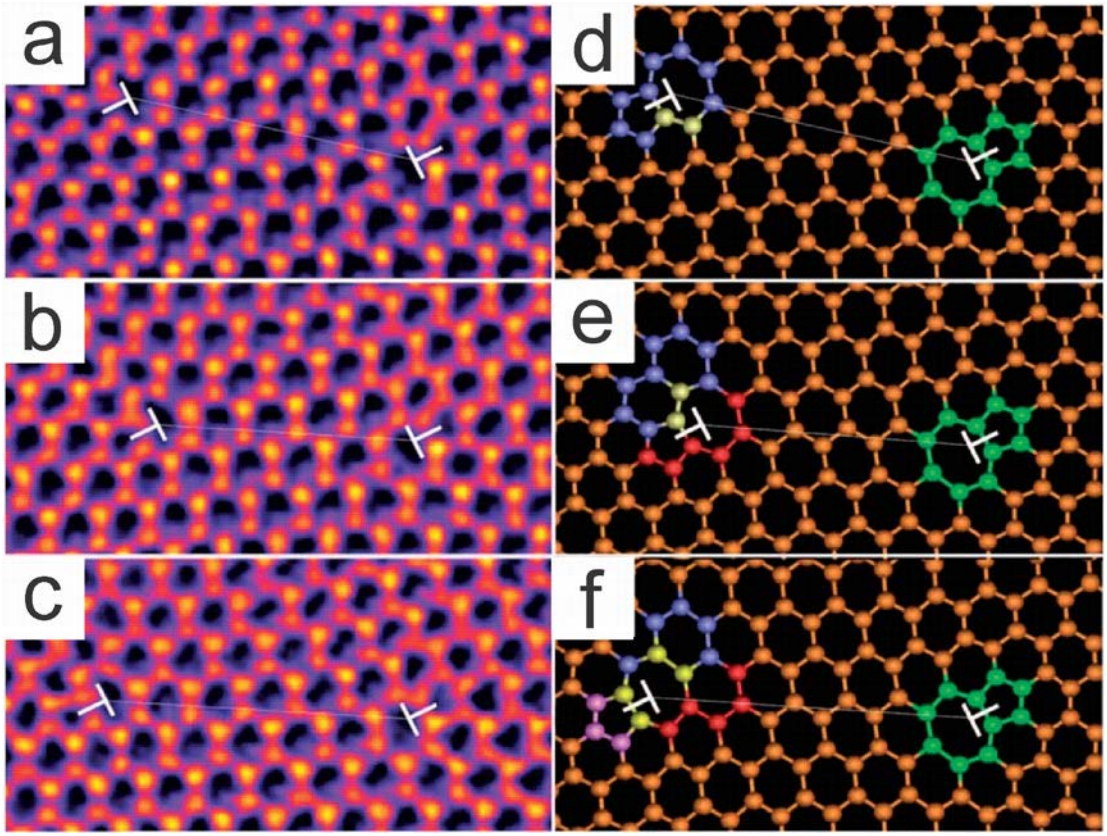

Figure 2-14. The migration of a dislocation in graphene. (a–c) Real-time AC-TEM images showing the basic glide (b) and climb (c) motions of a 5-7 dislocation. The dislocation are highlighted with white Ts. (d–f) Corresponding atomic models. Reproduced with permission from ref.[56], © Copyright © 2012 American Association for the Advancement of Science.

In 2012, Warner *et al.* atomically resolved the structure of a dislocation pair in graphene using an AC-TEM with monochromated beam source. [56] They have shown that similar to those in 3D crystals, the dislocations in graphene also migrate *via* glide or climb motions. In Figure 2-14, time sequential TEM images demonstrating the migration of a 5-7 dislocation are shown. A SW-like bond rotation of the C–C bond highlighted in yellow in Figure 2-14d and e leads to a lattice shift of the dislocation colored in blue (a glide step), making the dislocation pair moving closer. The dislocation then rapidly moves horizontally along the zigzag direction *via* the

sputtering of a carbon dimer (a climb step). A maximum of 26% contraction and 27% elongation of the C-C bonds in the dislocations have been revealed by directly measuring the bond lengths in HR-TEM images. It is also indicated that the strain field for both dislocations extends a few Ångstroms to intersect.

The time interval between the TEM frames in Figure 2-14 is 2 – 3 min. In order to increase the frequency of structural changes in graphene, Lehtinen *et al.* (2013) raised the beam current density to 1×10^{8} e nm^{-2} s^{-1} in an AC-TEM operated at 80 kV, which is one to two orders of magnitude higher than that is used for normal defect examination. [139] As a result, they have managed to observe the full life circle of dislocations in graphene, from birth to annihilation. TEM images in Figure 2-15 illustrate the real-time dynamics of the formation of a dislocation pair by the gradual sputtering of carbon atoms under prolonged electron irradiation. A D_1 (5-8-5) defect is created in the first place, which can be seen as the assembly of two pentagon-heptagon defects (Figure 2-15a). With the increase in the number of missing carbon atoms, the multivacancy eventually rearranges itself into a missing chain of carbon atoms between two dislocation cores (Figure 2-15e). This result corresponds to the previous theoretical prediction that a dislocation pair is more energetically favored than a multivacancy structure with ≥10 missing atoms. [140,141] Figure 2-16 shows a more complex form of dislocation glide discovered by Lehtinen *et al*. [139] A SW bond rotation first occurs next to the dislocation core, generating a 555-777 defect structure which can be regarded as three adjacent dislocation cores (Figure 2-16b). This chain of dislocation cores has been shown to have a lower formation energy in CNTs under high stress

conditions. [142] A further SW bond rotation of another C–C bond relaxes the upper two dislocations and brings the initial dislocation two steps downwards.

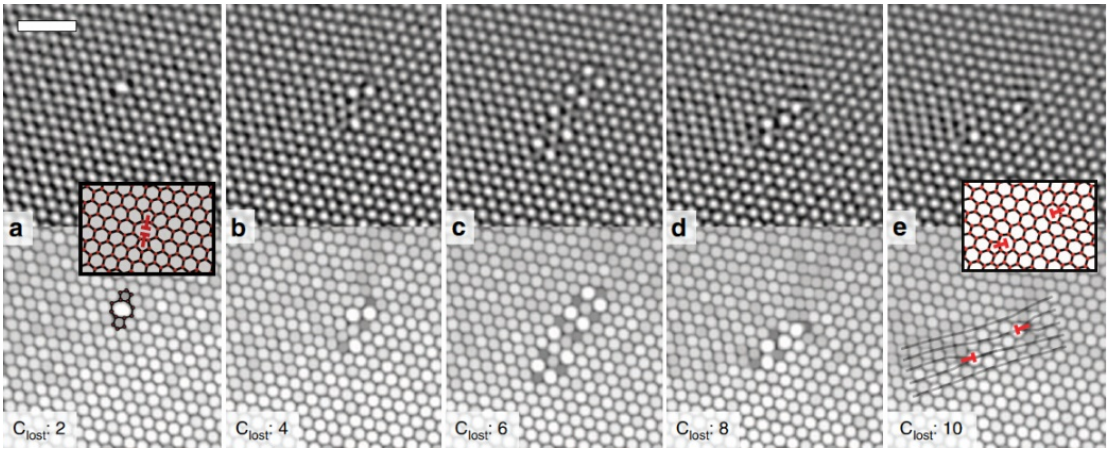

Figure 2-15. AC-TEM images illustrating the birth of a dislocation pair in graphene. The upper panels are the smoothed AC-TEM images. Their corresponding maximum filtered frames are displayed in the panels below. The scale bar in panel a is 1 nm. Reproduced with permission from ref.[139], © 2013 Nature Publishing Group.

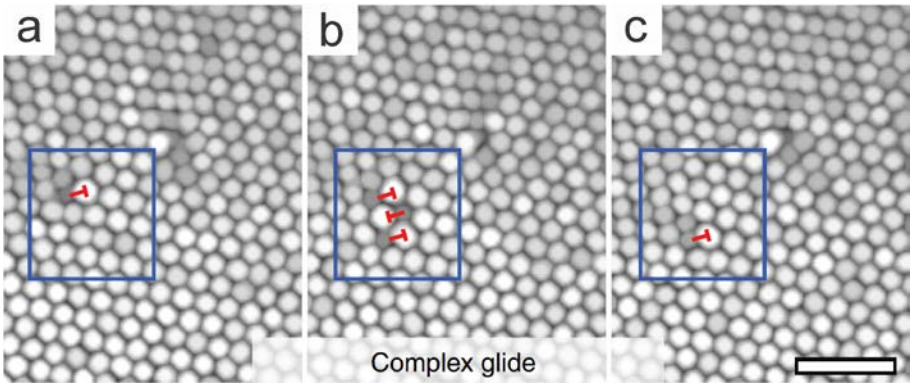

Figure 2-16. Maximum-filtered AC-TEM images showing a complex glide step of a 5-7 dislocation. Reproduced with permission from ref.[139], © 2013 Nature Publishing Group.

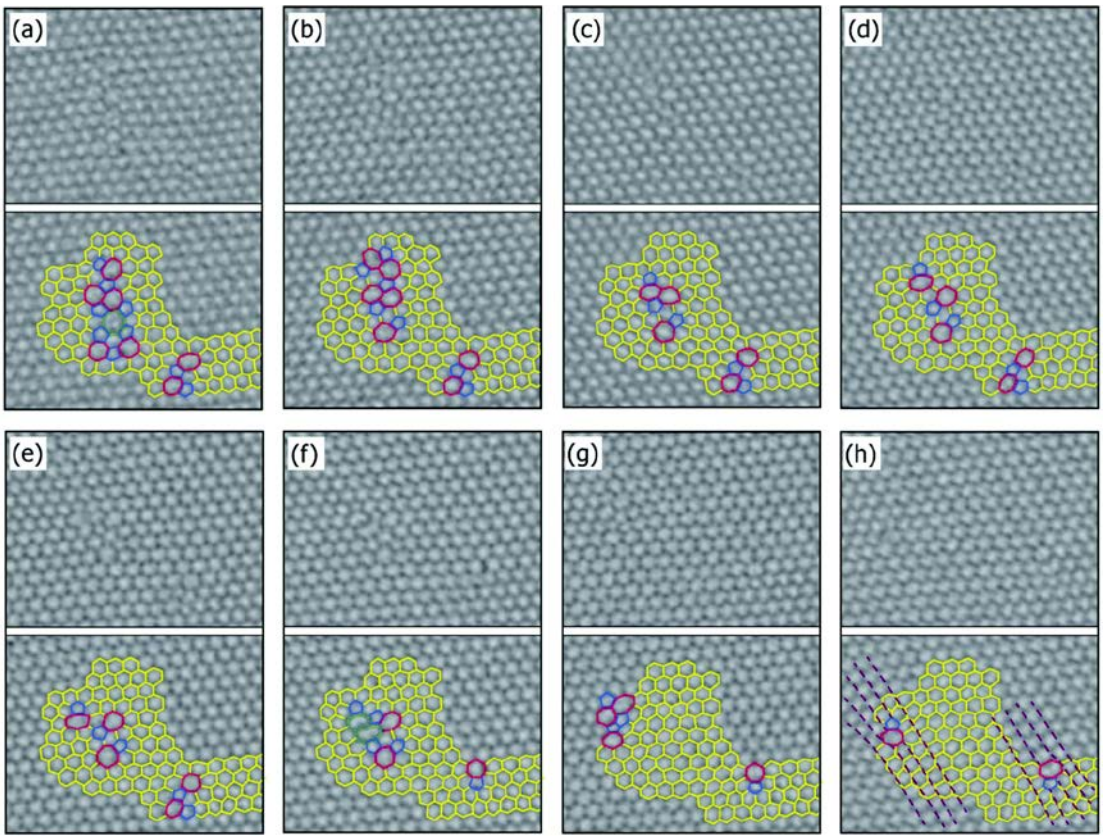

Figure 2-17. HR-TEM images showing real-time transformation from point defects to a pair of 5-7 dislocations. Reproduced with permission from ref.[143], © 2014 The Royal Society of Chemistry.

Lee *et al*. (2014) utilized a focused electron beam at 80 kV to create irregular defect structures (Figure 2-17a) and observed the defects gradually reconstructed into a pair of edge dislocations under electron irradiation in the imaging mode (Figure 2-17h). [143]

Unlike bulk materials, freely suspended graphene membrane can flex and buckle in a third dimension. [144–146] Theoretical modelling has revealed that the intrinsic rippling structure is practically one of out-of-plane distortions that help to stabilize graphene. [147,148] Since the TEM images are the 2D projection of the 3D object, the bucking fields in graphene can only be indirectly observed as in-plane compressive

strain. The length scale of the intrinsic buckling is 20 – 100 nm while the displacement in z-axis is only 0.5 – 2 nm), which makes subsequent change in d-spacing resulting from the lattice tilt quite inconspicuous even in AC-TEM.

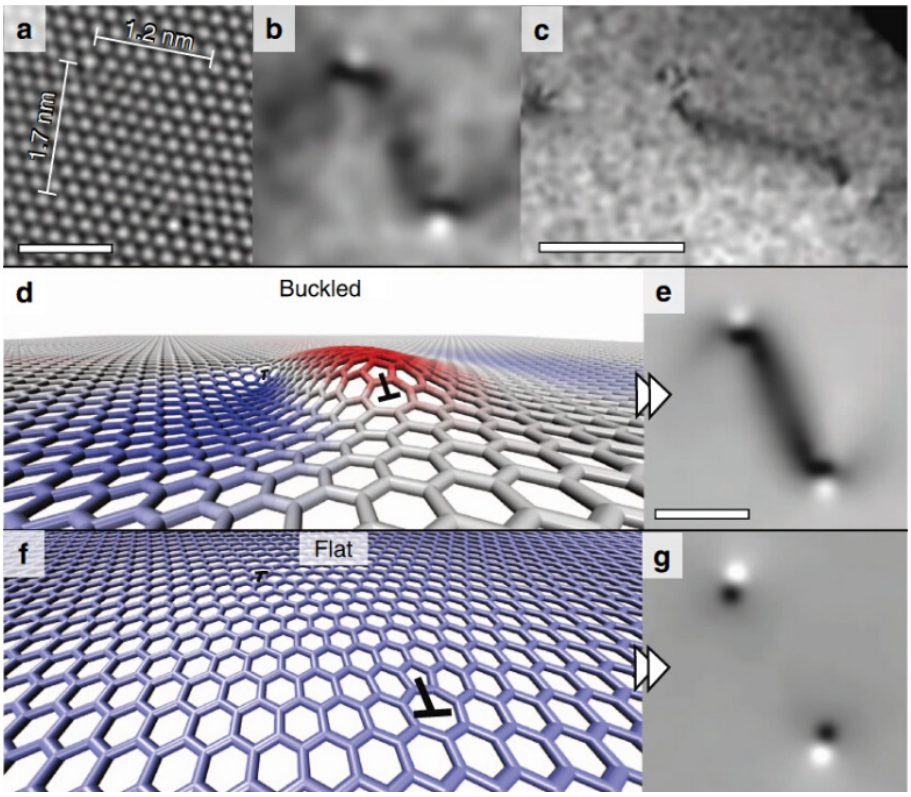

Figure 2-18. TEM imaging of the out-of-plane deformations introduced by two dislocations in graphene. (a) AC-TEM image showing two dislocation cores. (b) The same image shown in (a) after several steps of image filtering. (c) Large field-of-view imaging of ripping extending over a long distance. (d) A perspective view of the atomic model with the same configuration in (a), relaxed in a molecule dynamics simulation. (e) Atomic model same as that in (d), but with the system strained to be flat. (e,g) Simulated and filtered TEM images correspond to the models in (d) and (f) respectively. Scale bars are 1 nm in panel a and e, and 5 nm in panel c. Reproduced with permission from ref.[139], © 2013 Nature Publishing Group.

It has been confirmed by various experiments that the graphene sheet can be extensively rippled by introducing dislocations. [148–150] In Figure 2-18a an AC-TEM image of two interacting dislocation cores (not a pair) is shown. Lehtinen *et al.*

have discovered that the center of a tilted polygon in an AC-TEM image is less bright. [139] They further applied a maximum filter to the image to amplify the darkness of the tilted area (Figure 2-18b). There is an apparent dark contrast line between the dislocation cores, suggesting that the projection size of graphene lattice along that line is reduced. However, this could also result from the C–C bond contraction. To verify which scenario happens, they performed TEM image simulation to a molecular dynamics relaxed atomic model with same dislocation configuration, which is in good agreement with the experimental results. Another simulation carried on the same atomic model but strained to be flat shows no sign of dark contrast between the dislocation cores, ruling out the effects of compressive strain of C–C bonds. Warner *et al.* (2013) reported a method to remarkably increase the magnitude of rippling in graphene by introducing a large number of dislocations using focused electron beam with 80 keV energy in a TEM. [150] They raster-scanned the focused *e*-beam back and forth in a graphene sheet in order to provide the scanned area with multiple short exposures. By doing so they managed to create a large amount of dislocations without opening holes at the same time.

2.5.2.2 Gain Boundary

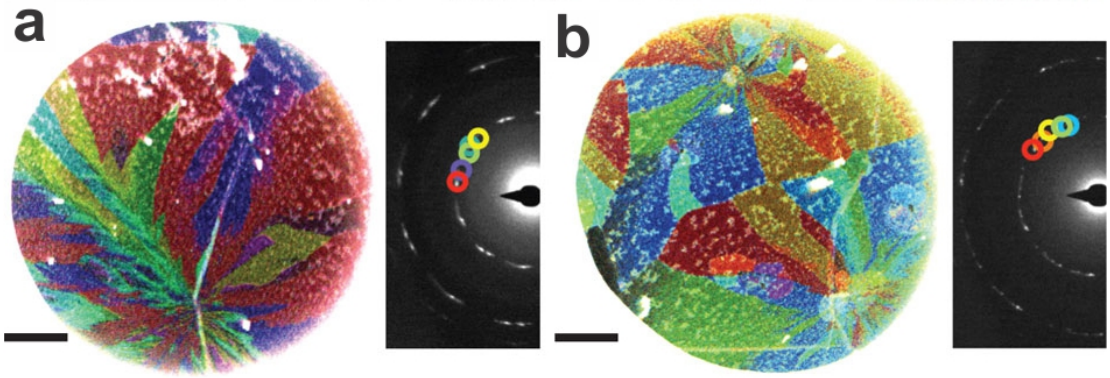

Figure 2-19. Mapping grains with different lattice orientations using dark-field TEM imaging. The false color used in the dark field image corresponds to the diffraction spot circled with the same color. Both scale bars are 500 nm. Reproduced with permission from ref.[129], © 2011 Nature Publishing Group.

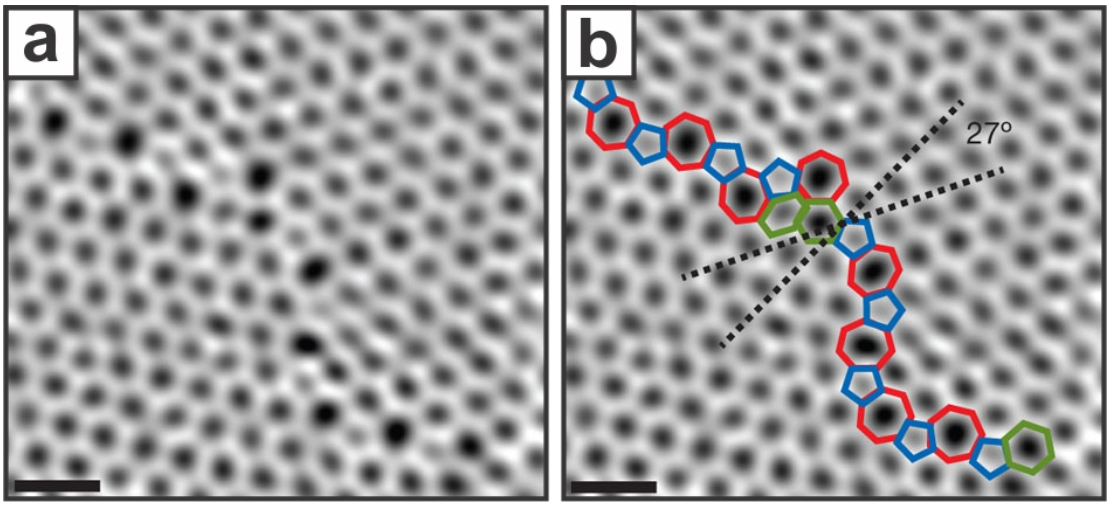

Figure 2-20. STEM images of a GB composed of adjacent pentagon-heptagon dislocations. (a) STEM image showing two graphene grains intersect with a 27° mismatch angle. (b) The same image from (a) with pentagons, heptagons and distorted hexagons highlighted in blue, red and green, respectively. Both scale bars are 0.5 nm. Reprinted with permission from ref.[129], © 2011 Nature Publishing Group.

Chemical vapor deposition is currently the only route to synthesize high quality graphene on an industrial scale. However, CVD synthesized graphene is inevitably polycrystalline and contains a large amount of GBs, which would introduce local

property deviations and influence potential applications of graphene. As a result, GBs in graphene have attracted far more research attention than point defects and dislocations in both theory and experiment.

Grains with different orientations in polycrystalline graphene can be easily distinguished in the dark-field (DF) imaging mode in a HR-TEM. By using an objective aperture filter in the back-fold plane to one by one select the diffraction spots, the grains corresponding to the selected orientations can be revealed in the real space, as shown in Figure 2-19.

Recent advances in aberration correction in (S)TEM enable the direct observation of the atomic configuration of the graphene grain boundary. Huang *et al*. (2011) demonstrated that the atomic structure of the tilted grain boundary is an alternating pentagon-heptagon chain using atomic resolution STEM imaging (Figure 2-20). [129] This conclusion was later confirmed by a large number of TEM and STM observations. [151–153] It has been suggested that the density of dislocation cores in a GB increases with the mismatch angles. [124] Lahiri *et al*. (2010) also reported the observation of 5-8-5 linear GBs (Figure 2-21) in polycrystalline graphene grown on Ni (111) by chemical vapor deposition, the formation of which is due to the strong interaction between graphene and Ni substrate. [109]

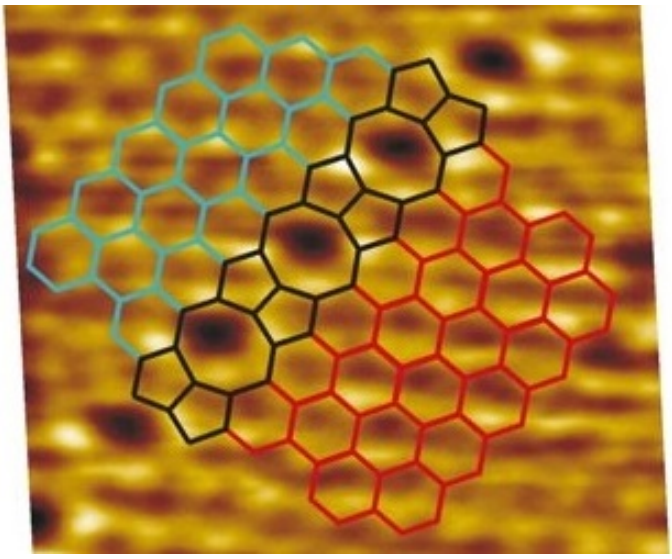

Figure 2-21. STM image of an extended 5-8-5 configured GB in graphene synthesized by CVD method on Ni substrate. Reprinted with permission from ref.[109], © 2010 Nature Publishing Group.

In most cases graphene GBs are classified as symmetric and asymmetric. GBs from CVD-synthesized graphene are often highly asymmetric and curved as shown in Figure 2-20. Westenfelder *et al.* (2011) demonstrated that highly meandering GBs could reconstruct into symmetric ones under the combined effect of electron irradiation and extreme heat (1000 °C). [154] Yang *et al*. (2014) reported that thermal annealing at temperatures above 600 °C helps to straighten curved GBs and improve crystalline quality of graphene. [153] The migration of GBs in graphene is very similar to that of dislocations. Kurasch *et al*. (2012) revealed that it is mediated by the rotation of C–C bonds under 80 kV electron irradiation by providing time sequential TEM images, which resembles the glide motion of dislocations. [152] Lee *et al*. (2015) performed *ab initio* simulation and suggested that GB migration could be also driven by the evaporation of a carbon dimer, similar to the climb step of a 5-7 configured dislocation, [155] which was later confirmed by the experimental results shown in Chapter 6.

A large number of reports have indicated that GBs in graphene can strongly impact its mechanical, electronic and chemical properties. [47,124,156–163] Wei *et al*. (2011) revealed that GBs can either enhance or weaken the strength of graphene, dependent on the detailed arrangements of pentagon-heptagon pairs. [156] Grantab *et al*. (2010) suggested that the strain at failure and ultimate strength increase with the mismatch angle of GBs in both zigzag- and armchair-oriented graphene using MD and DFT calculations. [124] The 5-8-5 configured GB discovered by Lahiri *et al*. has been reported to act as a quasi-one-dimensional metallic wire embedded in a perfect graphene sheet. [109] Yazyev *et al*. (2010) identified the presence of a well-defined transport band gap of 1.04 eV in graphene introduced by a particular asymmetric graphene GB, which makes it promising to develop graphene-based transistors. [47] Yasaei *et al*. (2014) observed that a GB has ~ 300 times higher sensitivity towards absorbed gas molecules [dimethyl methylphosphonate (DMMP), chosen for its electron-donating nature] than pristine graphene. [163] These findings open up new pathways for the design of graphene sensors and devices.

2.4 Conclusion

Graphene has grabbed appreciable research attention since its debut in 2004, mainly because of its unique properties. A variety of synthesis routes have been developed to produce graphene for multiple applications. Nevertheless, the law of physics has determined the existence of a certain level of lattice disorder in all materials. The imperfection in synthesis and transfer processes also introduces defects and contaminations into the graphene lattice, which makes some if its extraordinary properties remain only in theory. On the other hand, certain types of defects can be intentionally doped to tailor graphene properties for nanoengineering and nanoscale device fabrication.

Aberration-corrected high-resolution TEM plays a crucial role in not only direct imaging the two-dimensional lattice in great detail, but also controllably creating defects *via* electron irradiation. The application of AC-TEM has made a remarkable contribution to numerous researches in the field of graphene and other 2D materials in the past decade. This chapter highlights the pioneering studies on graphene 'self-doping' defects, including point defects, dislocations and grain boundaries, and gives the background for the next few chapters.

Chapter 3

Methodology

3.1 Introduction

This chapter elaborates specific experimental and analytical techniques that are exclusively applied in this research project, including CVD synthesis of graphene, transferring onto TEM grids, AC-TEM imaging and image processing and analysis. Instead of looking into the working principles of these techniques, this chapter focuses on delivering the experimental details, such as CVD recipes, instrument models and parameters. With the provided operation details, it is expected that all the experiments and analysis performed in this thesis can be replicated.

3.2 CVD synthesis of graphene

Graphene was synthesized by atmospheric pressure CVD using the experimental set-up illustrated in Figure 3-1.This method was originally developed by Dr Wu and his colleagues. [36] Molybdenum (Alfa Aesar, 99.95% pure, 0.1mm thick) and high purity copper foils (Alfa Aesar, Puratonic 99.999% pure, 0.1 mm thick) were cut into 1×1 cm^2 pieces and immersed into HCl solution (Alfa Aesar, 37% HCl:H_2O = 1:3) for 2 – 3 min to wash off the oxide layer, followed by the sonication in acetone and IPA both for 10 min.

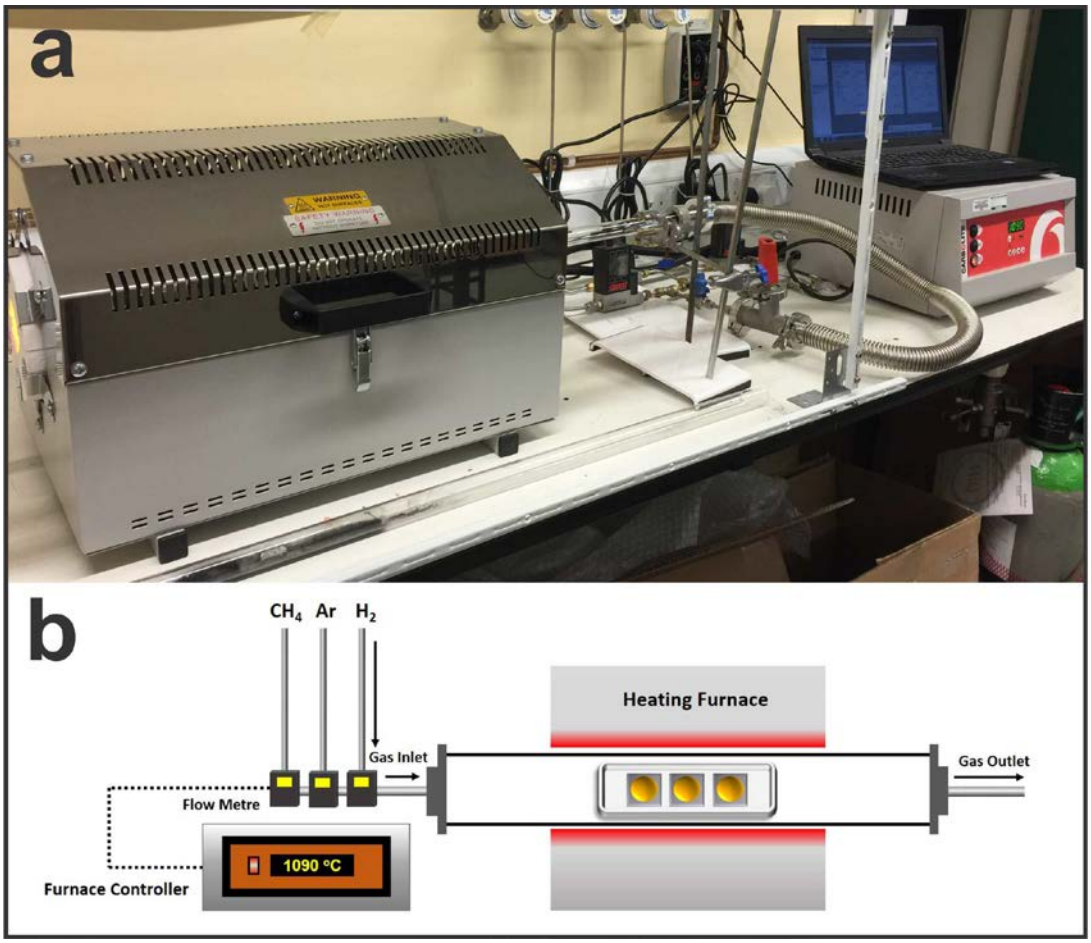

Figure 3-1 A photograph and schematic diagram of the CVD setup used to prepare graphene samples in this thesis.

The pretreated Cu and Mo pieces were loaded into a ceramic boat with Cu on top and Mo at the bottom, which was then placed in the middle of a 1-inch quartz tube in the CVD system. The Mo act as a support layer to prevent melted copper from balling. The CVD reaction can be divided into the following steps. First, 100 s.c.c.m. H_2/Ar (20% H_2 in Ar), 100 s.c.c.m. CH_4 (1% CH_4 in Ar) and 200 s.c.c.m. 100% Ar were flowed to flush the system for 30 minutes. Afterward, CH_4 flow was switched off and H_2 flow was reduced to 80 s.c.c.m., while the reaction chamber was heated to 1090 °C to anneal the sample for 30 min. Next, 10 s.c.c.m. of 1% CH_4 in Ar was added into the system

for 90 min for graphene growth. Following this, the methane flow and furnace were turned off, and the ceramic boat was moved out of the heating zone for rapid cooling.

3.3 Transfer onto TEM grids

A poly-methyl-methacrylate (PMMA) supportive scaffold (8% wt in anisole, 495K molecular weight) was spin cast onto the graphene side of the graphene/Cu/Mo stack at 4700 rpm for 60 s. The sample was then baked at 180 °C for 90 s in air for PMMA to solidify. The Cu layer was etched by floating the sample on the mixed solution of iron (III) chloride and hydrochloride for several hours. Mo was also etched by iron (III) chloride but at a much slower rate than Cu. After the etching of Cu, the PMMA-graphene film floated on the surface while the Mo layer sank to the bottom. The film was then transferred onto the top of deionized (DI) water for 30 min using a clean glass slide. This process was repeated three times to fully dissolve residual iron chloride, before transferring the film onto targeted substrates. In this work, the PMMA/graphene film was transferred onto a Si_3N_4 grid (Agar Scientific Y5385) or a heating grid designed for *in situ* TEM experiments. The sample was left in the fume hood for 4 – 6 hours and heated at 150 °C for 15 min for complete drying. Eventually, the grid was cured in the CVD furnace at 350 °C overnight to burn out PMMA, leaving only graphene on the grid.

3.4 Scanning electron microscopy/focused ion beam

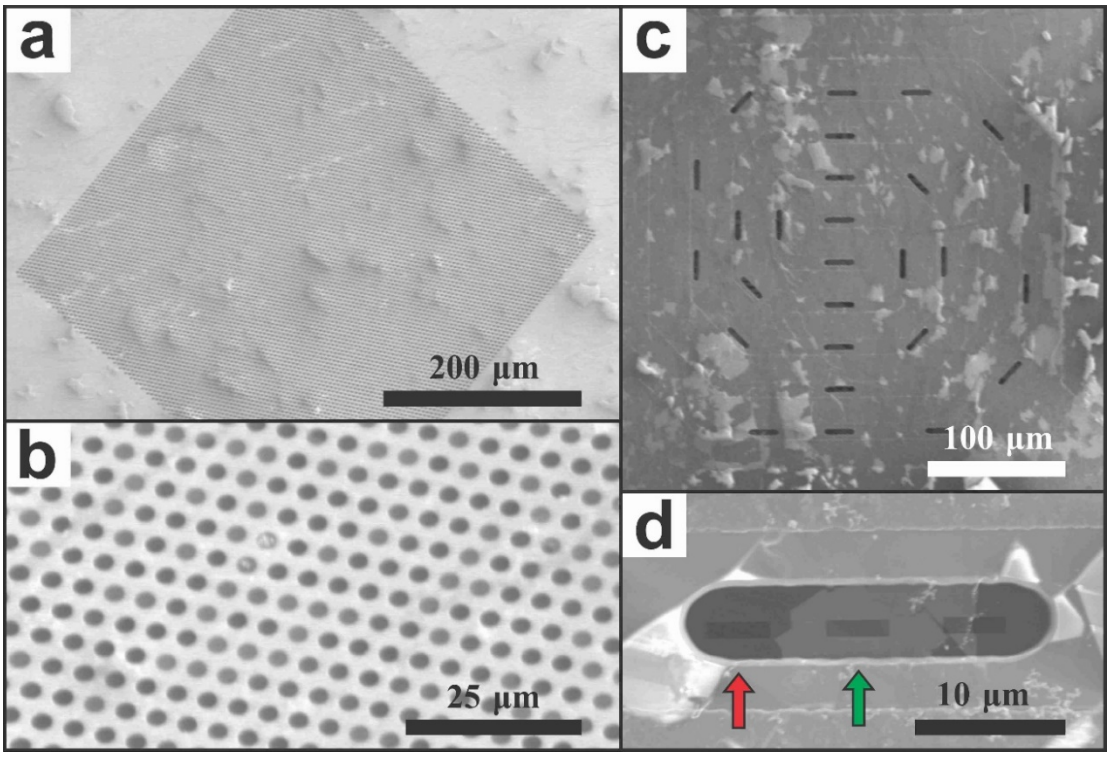

Figure 3-2. SEM micrographs showing TEM grids partially covered by monolayer graphene film. (a,b) Agar Scientific Y5385 holey Si_3N_4 grid. (c,d) Pt coil imbedded TEM chip designed for *in situ* heating experiments (DENS Solutions SH30-4M-FS) with 0.2 × 3 µm windows fabricated by FIB. The green arrow in panel d indicates a window fully covered by graphene and the red arrow indicate an empty window.

The instruments used in this thesis is Hitachi S-4300 field-emission SEM and ZEISS NVision 40 FIB-SEM (Focused Ion Beam-Scanning electron microscope dual system). The FIB was used to fabricate 0.2 × 3 µm windows in the Si_3N_4 membrane of TEM grids (DENS Solutions SH30-4M-FS, Figure 3-2d) designed for *in situ* transmission electron microscopy. These windows as shown in Figure 3-2 allow HR-TEM imaging of suspended graphene at atomic resolution.

SEM in this project was generally used to examine the coverage and surface cleanliness of graphene on TEM grids at an accelerating voltage of 3 kV. In Figure 3-2, windows

covered by graphene can be easily distinguished as their contrast is lighter than the empty ones.

3.5 Aberration-corrected transmission electron microscopy

The atomic resolution TEM images analyzed in the following chapters were capture by Oxford-Jeol 2200MCO field-emission TEM with a CEOS probe and aberration corrector at an accelerating voltage of 80 kV. A Zemlin tableau is automatically acquired by the software with beam tilts predefined by the user. A series of diffractograms are taken on a very thin amorphous area with different tilt angles at 500K × magnification. Figure 3-3 shows a phase plate after aberration correction (a) and a tableau of 21 diffractograms with an outer tilt angle of 24 mrad. The details of residue aberration are listed in Table 3-1.

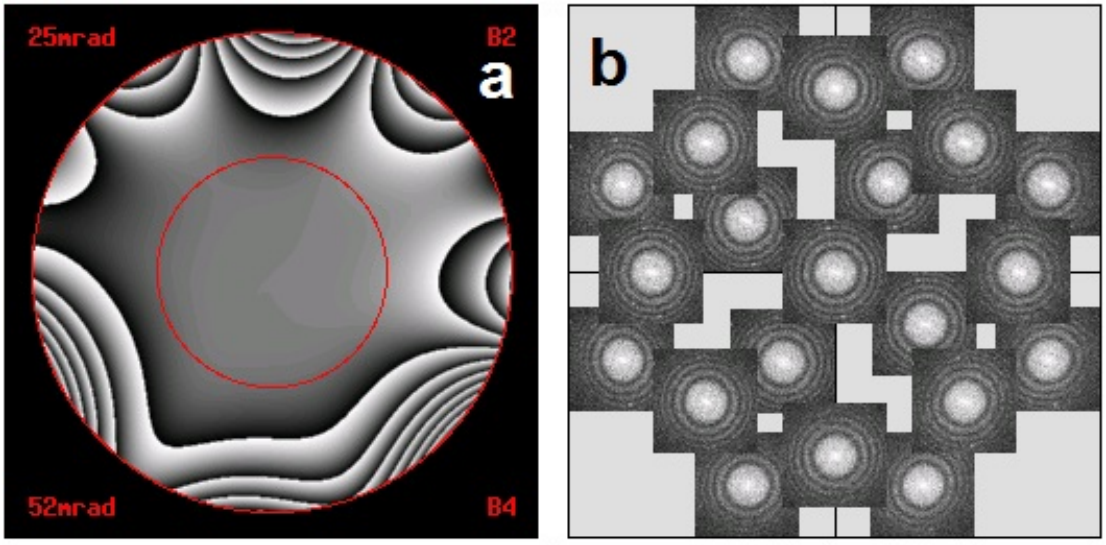

Figure 3–3. A Zemlin tableau taken with an outer tilt angle of 24 mrad before the acquisition of images in real space. (a) Phase plate due to residual aberrations. (b) 21 diffractograms taken with different beam tilt angles using an enhanced tableau.

Table 3-1. Details of the Residue Aberration in Figure 3-3

Aberration Coefficient	Notation	Value
Defocus	C1	- 145.7 nm
2-fold astigmatism	A1	289.9 pm
3-fold astigmatism	A2	21.05 nm
3rd order Spherical aberration	C3	- 1.247 μm
Coma	B2	21.05 nm

These values vary each time the aberration correction software is run. In order to achieve sufficient spatial resolution to resolve graphene lattice configuration, these aberrations are limited within a specific range: A1 < 1 nm; A2 < 50 nm; B2 < 20 nm; -5 μm < C3 < 2 μm; A3, S3 < 1 μm. After that the magnification can be raised to 1 – 2M × for graphene real space imaging. Original TEM frames were recorded using a Gatan Ultrascan 4K × 4K CCD camera with 0.5 – 2 s acquisition time and 2 pixel binning. The time interval between two sequential images are 5 – 15 s (mono-off).

A small proportion of TEM images shown in Chapter 4 – 7 were taken with the additional use of a double Wien filter monochromator with a 7 μm slit which reduces the energy spread of the electron beam to ~ 0.21 eV. Figure 3-4 shows the comparison in spatial resolution between original TEM frames taken with monochromator on and off. It is apparent that the application of monochromator significantly improves image quality, but it also requires protracted time for the fine manual adjustment of aberrations. The interval between two images are therefore extended to ~ 20 s on average. In practice, a majority of TEM data in this thesis are recorded in mono-off

mode, as the resolution in Figure 3-4b is sufficient to resolve the lattice structure in graphene.

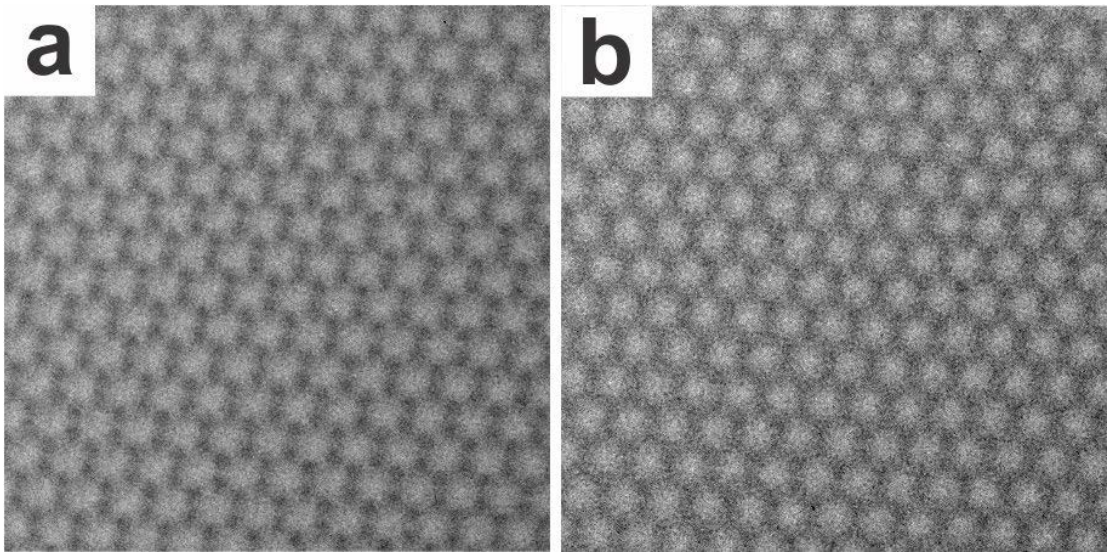

Figure 3-4. Original AC-TEM images acquired by Oxford-Jeol 2200MCO with monochromator (a) and (b) off.

3.6 *In situ* heating holder

Heating experiments were performed using a commercially available *in situ* heating holder (DENS Solutions SH30-4M-FS). Inside the holder, the specimen was heated by passing a current through the platinum resistive coil which is imbedded in the TEM chip (DENS Solutions DENS-C-30). As there is a linear correlation between temperature and chip resistance, the specimen temperature can be measured and controlled with high accuracy.

3.7 AC-TEM image processing

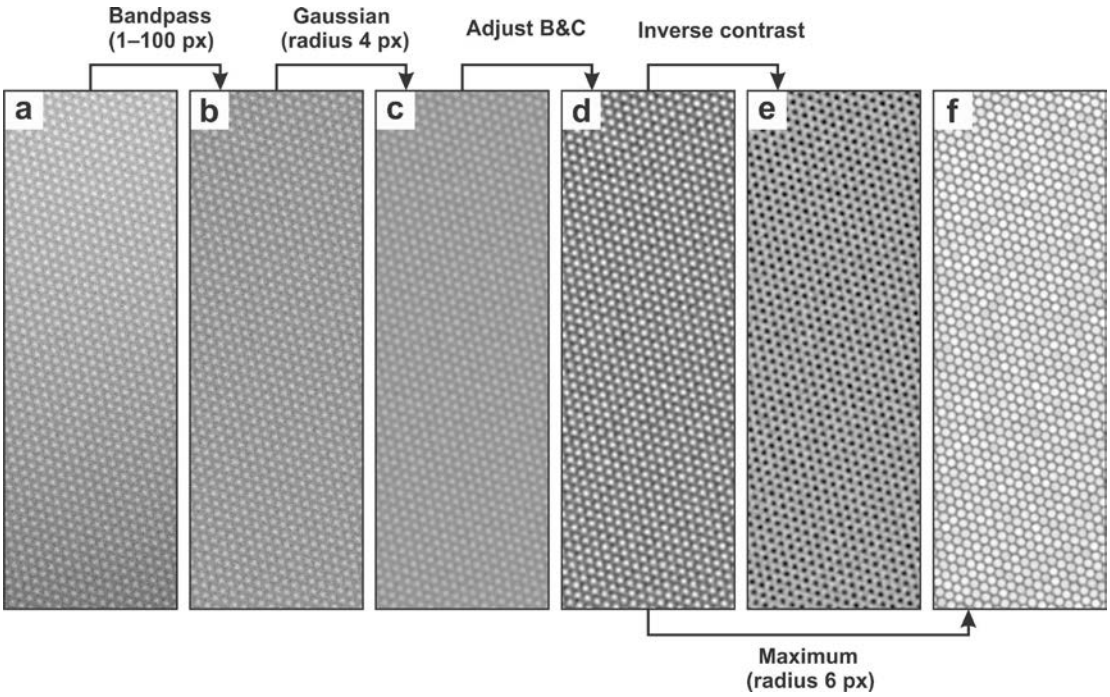

Figure 3-5. An example showing the processing techniques of AC-TEM images. A bandpass filter (1 – 100 pixels) is first used to even the image illumination (panel b), followed by a Gaussian filter with a radius of 4 pixels (panel c). Subsequently, the brightness and contrast of the image is adjusted. The contrast of the image can be inversed to show light atoms on a dark background (panel e). A maximum filter can be applied to panel (d) to highlight the atomic configuration of graphene.

Raw TEM data often has low signal-to-noise ratio and is hard to interpret *via* visual inspection. Thus it is necessary to develop image processing techniques to facilitate further inspection and analysis. Figure 3-5 shows the imaging processing procedure employed in this thesis using the Image J software. A FFT bandpass filter (1 – 100 pixels) is first applied to remove the shading effect due to the uneven illumination during image capturing (Figure 3-5b). The image is then blurred to further reduce the noise using a Gaussian filter with a radius ranging from 2.0 to 6.0 pixels, depending on the signal-to-noise ratio of the image (Figure 3-5c). Following this, the brightness and

contrast (B&C) is optimized for a better visual effect (Figure 3-5d). Most raw TEM images in this research show dark atoms on a light background and the contrast can be inversed using ImageJ (Figure 3-5e). Sometimes in order to highlight non-hexagon rings in graphene, a maximum filter with a radius of 4–6 pixels is applied (Figure 3-5f).

3.8 AC-TEM image analysis and simulation

3.8.1 TBMD and DFT calculations

The density functional theory (DFT) and tight-binding molecular dynamics (TBMD) simulations are performed by Professor Gun-Do Lee at Seoul National University. The atomic models which correspond to the graphene lattice to analyze are initially prepared in Accelrys Discovery Studio 3.5 Client. DFT calculations are were carried out within the generalized gradient approximation of Perdew−Burke−Ernzerhof (PBE) functional using Vienna *ab initio* simulation package (VASP) code. [164,165] TBMD simulations are performed using a modified environment-dependent tight-binding (EDTB) carbon potential, [166] which is modified from the original EDTB carbon potential to study carbon sp^2 bond networks, [167] and has been successfully applied to investigations of various defect structures in graphene and carbon nanotubes. The details of the TBMD simulation methods have been described in ref.[168].

3.8.2 JEMS simulation

TEM image simulation is an important tool in TEM studies, as it gives the simulated TEM view of a predefined structure that can be used to compare with the real images.

All simulations shown in the following chapters are performed in the JEMS software (developed by Dr P. A. Stadelmann). The DFT/TBMD optimized atomic models are converted into JEMS readable files using a Python script provided by Dr C. S. Allen. The simulated images are produced based on multislice algorithms in the software. [169,170] The defocus spread, 2-fold, 3-fold astigmatism and coma of simulated images can be adjusted in JEMS using aberration data from real experiments (Section 3.5).

3.8.3 Geometric phase analysis

Geometric Phase Analysis (GPA) was performed in Digital Micrograph using Koch's FRWR tools plugin, based on the methods proposed by Hytch *et al*. [171] The details of this analysis approach are discussed in Chapter 4.

Chapter 4

Spatial Dependent Lattice Deformations for Dislocations at the Edges of Graphene

4.1 Introduction

Dislocations play a key role in the plasticity of materials and their 3D deformations. [172–174] However, a century after it was first proposed, the real-time atomic-scale motion and annihilation of dislocations in 3D crystals is still limited. Graphene is a one-atom-thick crystal with extraordinary electronic, magnetic and mechanical properties, which are easily affected by defects and dislocations. [1,5,9,175–178] The two-dimensional nature of graphene makes it a perfect candidate to study dislocations at the atomic level using transmission electron microscopy (TEM). [56,128,139]

High resolution TEM operated at an accelerating voltage of 80 kV drastically reduces knock-on damage to graphene. When chromatic aberration effects are reduced by monochromation of the electron source combined with aberration correction it is possible to obtain ~ 80 pm spatial resolution. [77,108,179,180] Recent work showed that focusing an electron beam at 80 keV greatly increases the beam current density and it can controllably create defects in graphene including vacancies, dislocations and holes. [73] These defects are likely to be introduced by a complex chemical etching process, rather than direct knock-on sputtering. The formation, migration and interaction between two dislocations have been illustrated recently at the atomic level

using AC-TEM. [56,139] It has also been reported that a dislocation in graphene is a very stable form of defect, which can only be eliminated from the lattice of graphene by either annihilation from two opposite orientated dislocations or by migration to the edge of the lattice. [143,181]

Freely suspended graphene membranes can flex and buckle in z-direction. [144,146,182] Rippling is an out-of-plane distortion that is thought to help stabilize graphene. [147,183] It was theoretically predicted and later experimentally confirmed that dislocations lead to rippling in free-standing graphene sheets. [148–150] The study of how dislocations behave close to the edge of graphene has not been experimentally examined and is the subject of this chapter. By using atomic resolution TEM this chapter aims to understand the changes in the local strain properties around dislocations at the edge compared to those located in the bulk.

4.2 Results and discussion

4.2.1 Creation of dislocations and edges

Dislocations were created in graphene using a focused electron beam, as previously reported, and in some circumstances holes opened up next to the dislocations to provide an edge to interact with. [73] Figure 4-1a shows the formation of a hole and two pentagon-heptagon dislocation cores after the first exposure to the focused beam for 60 s. Once the edge is created, the atoms on the edge are susceptible to sputtering by the 80 keV electrons. A second and third exposure to a focused electron beam for 60 s after 10 and 15 min accelerated the sputtering of edge atoms. After that the beam was expanded back to image the irradiated area (Figure 4-1b–d). When the beam current density was reduced to $\sim 10^5$ *e* nm^{-2} s^{-1} in the imaging mode, the hole still kept on expanding, but at a very slow radial expansion rate of 1.4 pm s^{-1}. With the gradually sputtering of carbon atoms on the edge, the distance between the edge and the dislocations was reduced. The dislocation on the right side finally vanished 27 min after it was created (Figure 4-1e and f). The 55-77 and 555-7-8 defects on the left side, indicated in Figure 4-1c and e are the reconstructed dislocation structure with a Stone-Wales rotation to the pentagon-heptagon structure. The two dislocation cores highlighted in Figure 4-1 are not paired, *i.e.*, they do not have opposite direction, which means there must be at least two more dislocations within this local area. These two dislocations are highlighted because one of them is located near the edge (yellow box), whereas the other is located further away from the edge (white box). This gives a good comparison between the behaviors of dislocations at the edge and in the bulk. In order to understand what changes may result from a dislocation being located near the edge

of graphene, density functional theory (DFT) calculations of similar atomic structures were performed.

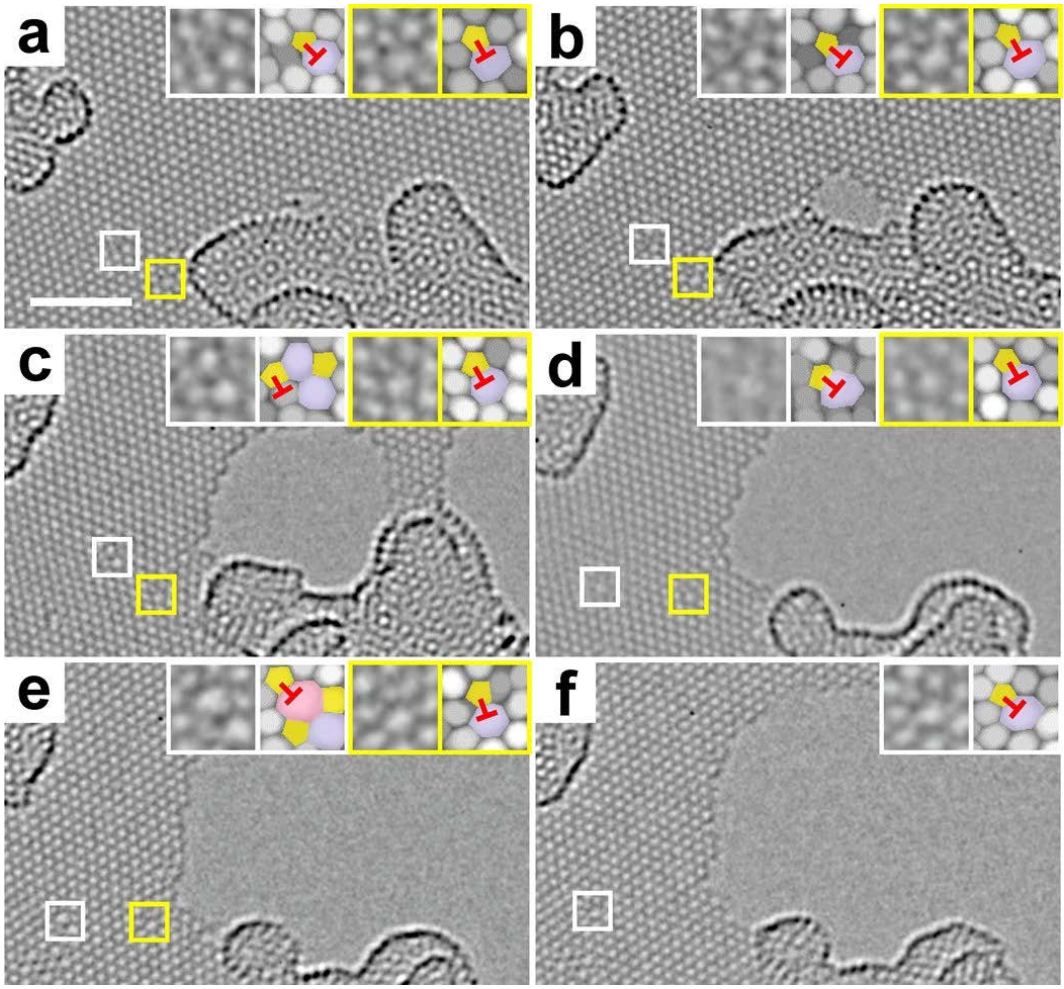

Figure 4-1. AC-TEM images showing the formation of dislocations near the edges of holes in graphene (magnified and maximum filtered views shown in the insets). Images were taken at times of (a) t = 0, (b) t = 7 min and 13 s, (c) t = 12 min and 41 s, (d) t = 18 min and 41 s, (e) t = 25 min and 24 s, (f) t = 26 min and 40 s. The scale bar in panels a is 2 nm. The color scheme in the maximum filtered images represents the number of carbon atoms in each ring, with 5 = yellow, 7 = blue, and 8 = pink.

4.2.2 Lattice deformation introduced by dislocations at different positions

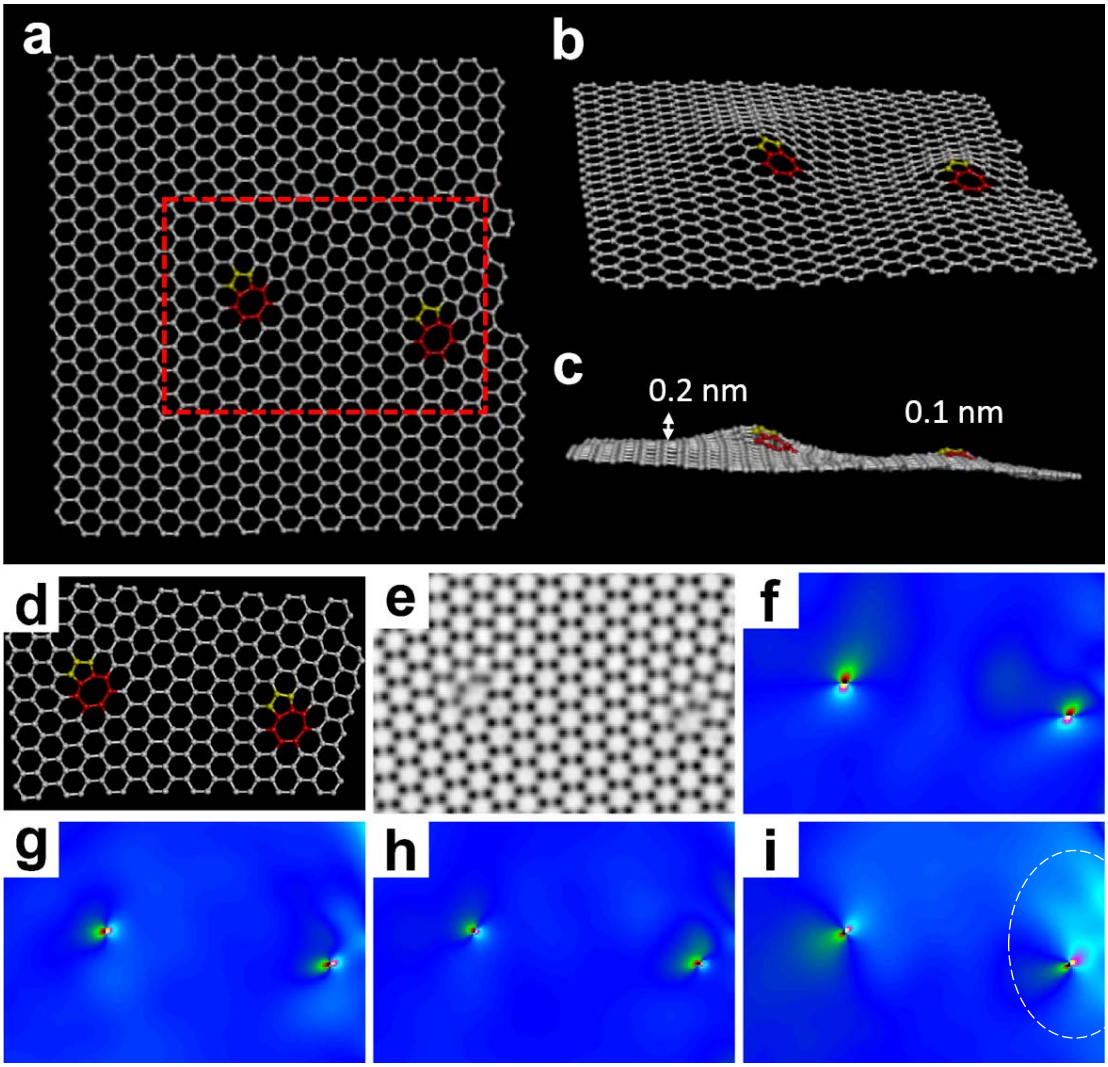

Figure 4-2. Density Functional Theory (DFT) simulations of ripples introduced by two dislocations located at different positions in graphene and their analysis. (a–c) DFT calculated atomic models of graphene with two dislocations (one in the center and one at the edge) (top, side and 3D views), provided by Professor Gun-Do Lee's group from Seoul National University. Multislice images simulation (e) is applied to the atomic model of the red box in a (d) with - 2 nm defocus and 4 nm defocus spread. (f–i) Geometric phase analysis (GPA) strain plots (f) ε_{xx}, (g) ε_{xy}, (h) ε_{yy} and (i) rotation (radians) based on the image in e. Color scale bar used for GPA plots is in panel f (-1 to 1).

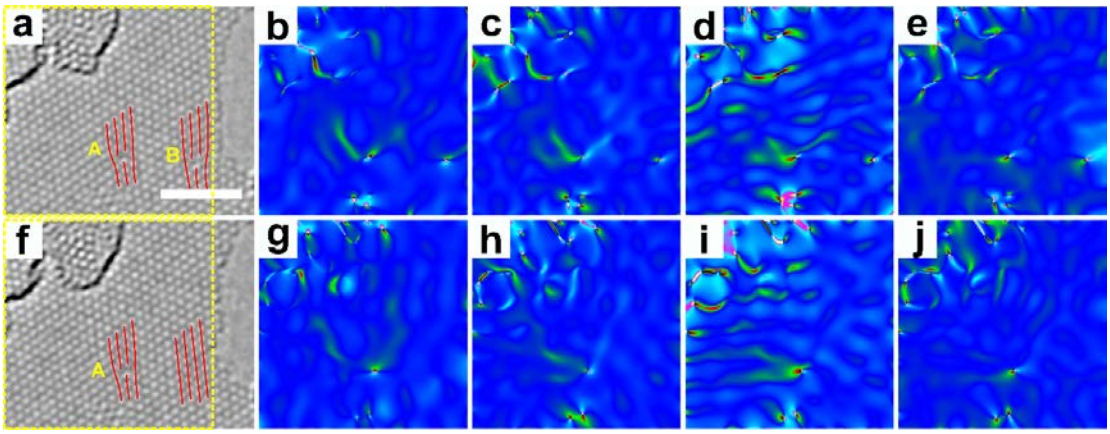

Figure 4-3. AC-TEM images of graphene with dislocations and their GPA plots. Smoothed AC-TEM images taken (a) before and (f) after Dislocation B disappeared. (b–e) GPA analysis based in panel a with (b) ε_{xx}, (c) ε_{xy}, (d) ε_{yy} and (e) rotation (radians). (g–j) GPA analysis based on panel f with (g) ε_{xx}, (h) ε_{xy}, (i) ε_{yy} and (j) rotation (radians). Time between panels a and f is 67 s. The scale bar in panel a is 2 nm.

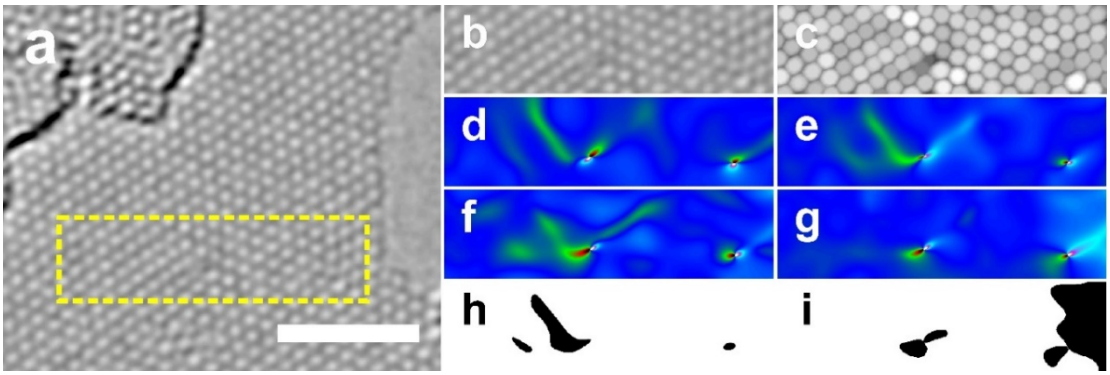

Figure 4-4. Smoothed and maximum filtered AC-TEM images and accompanying GPA plots of both dislocations cropped from Figure 4-3a. (a) Same TEM image as in Figure 4-3a with a dashed yellow rectangular box showing the cropped area presented in (b). (c) Maximum filtered image of panel b. (d–g) GPA plots of panel b, (d) ε_{xx}, (e) ε_{xy}, (f) ε_{yy} and (g) rotation (radians). (h) Binarized version of panel f, with the area where $\varepsilon_{yy} < -0.1$ being black, rest being white. (i) Binarized version of panel g, with the area where |rotation| > 0.1 is black. The scale bar in panel a is 2 nm.

Figure 4-2a–c shows the atomic model of two separated dislocations in graphene calculated by DFT. The simulation results indicate that both dislocation cores introduce rippling. Furthermore, it can be observed that the size of the ripple introduced by the

dislocation near the graphene edge is smaller than that introduced by the dislocation in the center of graphene. A rough value of the height of the two ripples is measured and shown in Figure 4-2c; the ripple introduced by the central dislocation is about twice (0.2 nm) that of the one located near the edge (0.1 nm). To further study the difference in lattice distortion introduced by two dislocations, a multislice image simulation using the DFT atomic model (the red box region in Figure 4-2a) was performed, shown in Figure 4-2d, and then analyzed the image using geometric phase analysis (GPA). Applying GPA to HR-TEM images is an effective way to identify and measure the out-of-plane distortion of graphene. [56,150,169–171] Previous research has demonstrated that the tilting of graphene lattice in z-direction is resolved as a noticeable decrease in lattice spacing in HR-TEM images, as the 2D projection of graphene 3D structure. [150] Theoretical simulations also indicated that C–C covalent bond lengths barely changed within the hexagonal rings. Thus, the "compression" in strain plots conducted by GPA can be interpreted as the lattice tilting of ripples, which is confirmed by the ε_{xx} strain plot in Figure 4-2f. The magnitude and location of the green region (corresponding to - 0.2 in strain) in Figure 4-2f are in accordance with visual inspection of the atomic model in Figure 4-2c. The rotation plot from GPA can also be used to measure the in-plane C–C bond rotation. The light blue region (corresponding to + 0.2), indicated with a white dashed circle in Figure 4-2i, shows the area with significant bond rotation, which is mostly located between the right dislocation and the edge.

4.2.3 Bond rotation and other defect structures at graphene edge

In Figure 4-3 the experimental TEM images are examined. Figure 4-3a shows both dislocations cause lattice distortion of the surrounding area (indicated with red lines). When the dislocation disappeared, the additional row of atoms and the lattice distortion were eliminated (Figure 4-3f). This result is further analyzed using GPA, as is shown in Figures 4-3b–e and g–j. The "compression" shown in GPA plots (ε_{xx}, ε_{xy} and ε_{yy}) in Figure 4-3 is due to the tilting of the graphene lattice from ripples. Figure 4-4 shows the GPA in higher magnification. The green region (corresponding to - 0.2 in strain) in ε_{xx}, ε_{xy} and ε_{yy} strain plots represent the regions with significant change in lattice distance. In a similar way, the light blue and green colors in the rotation plots in Figure 4-3f,j and 4-4 indicate noticeable in-plane C–C bond rotation in these regions. It is found that the dislocation at the inner side of graphene (A) causes a much larger rippling of its surrounding area. The relative rippling area where $\varepsilon_{yy} < -0.1$ (black region in Figure 4-4h) introduced by Dislocation A (0.215 nm^2) is ~ 18 times that caused by Dislocation B (0.0120 nm^2). In the maximum filtered image (Figure 4-4c), the pentagon in Dislocation A and its neighboring hexagon are far less regular and less clearly resolved than those in Dislocation B, which also suggests Dislocation A causes a more severe out-of-plane distortion than B. On the contrary, the in-plane rotation ($|rotation| > 0.1$) caused by Dislocation A is only restricted in a small surrounding area, while that of dislocation B extends to a much larger area out to the edge. The strain introduced by the dislocation is accommodated differently if the dislocation is located near the edge of graphene. It gives rise to extensive in-plane rotation in the lattice

between the dislocation and edge, rather than “hillocks” (large area of out-of-plane distortion) resulting from ripples.

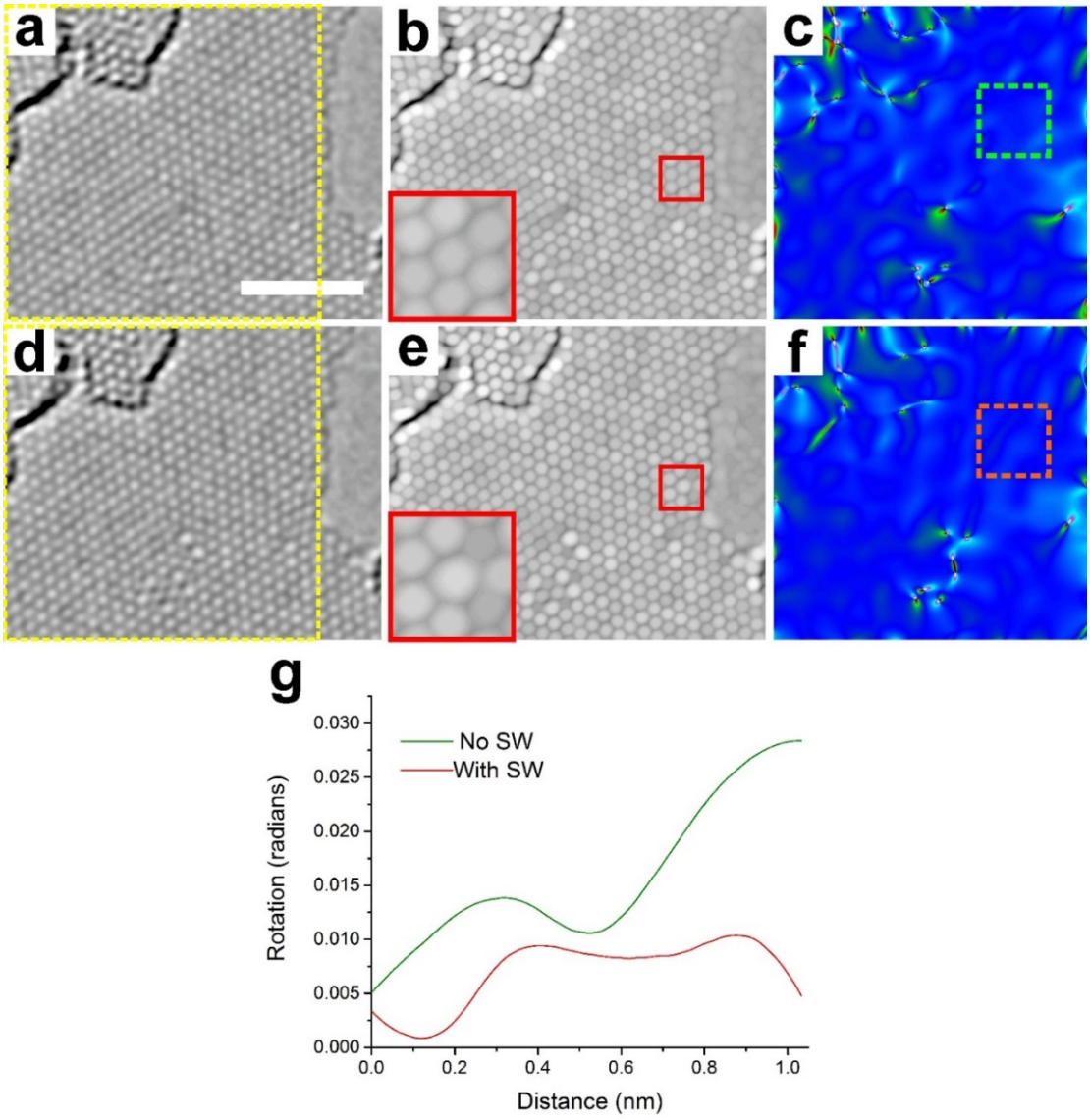

Figure 4-5. Bond rotations at the edge of graphene. AC-TEM images of the edge of graphene (a) before and (d) after a bond rotation at the edge. (b) Maximum filtered image of (a), with magnified view shown in the inset. (c) Rotation plot from GPA of the cropped area in panel a. (e) Maximum filtered image of (d), with magnified view shown in the inset. (f) Rotation plot from GPA of the cropped area in panel d. (g) Boxed line profile from the dashed square in panel c and f showing the average rotation over vertical 158 pixels corresponding to a distance of 0.65 nm. The scale bar in panel a is 2 nm.

Instead of a large area of C–C bond rotation, the lattice mismatch introduced by the dislocation can also be accommodated by defect structures at the edge. Bond rotation of edge atoms is the most frequently observed behavior, shown in Figure 4-5d and 4-6a. Two similar TEM images, one with Stone-Wales rotation on the edge (Figure 4-5d), the other without (Figure 4-5a) are analyzed. The rotated area (green and blue area in rotation plots) around the dislocation core reduced significantly with the Stone-Wales rotation on the edge (Figure 4-5c, f). The mean value of rotation in the vertical direction of the same region away from the dislocation in both images is also measured. The result shown in Figure 4-5g reveals that the existence of Stone-Wales rotation on the graphene edge can lead to the decrease of rotation in the area far from the dislocation core.

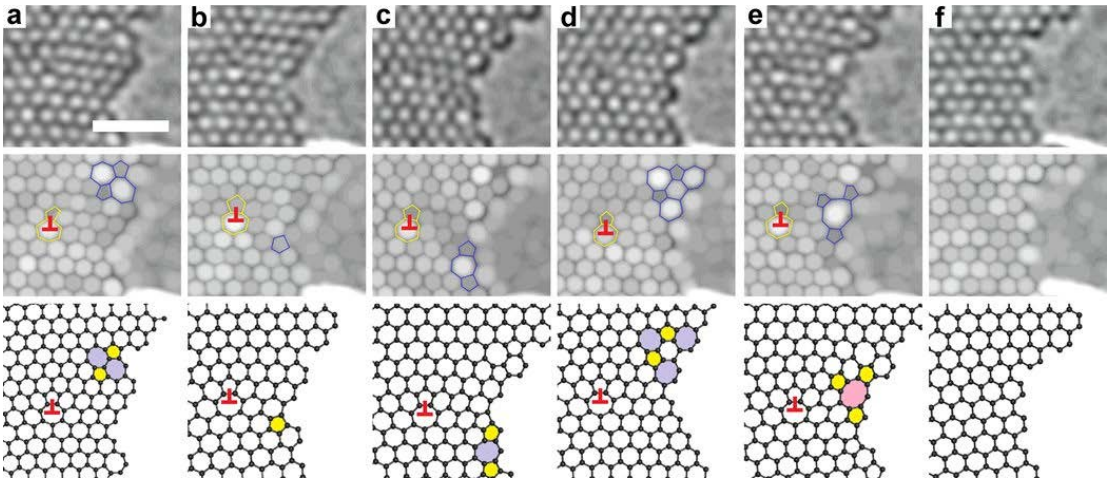

Figure 4-6. Different kinds of defects found at the edge of graphene when a dislocation is nearby. AC-TEM images (with corresponding maximum filtered images below) showing (a) bond rotation, (b) an isolated pentagon, (c) a 5-7-5 structure, (d) double bond rotation structure, (e) a 555-8 structure. The scale bar in panel a is 1 nm. The color scheme in the atomic models represents the number of carbon atoms in each ring, with 5 = yellow, 7 = blue and 8 = pink.

To study the time-dependent edge structure with the dislocation nearby, in total 54 TEM images over 608 s, with 11 s per image on average were taken. About 40 images were taken when the dislocation was near the edge and the remaining 14 were taken after the dislocation disappeared by migrating to the edge. Along with the bond rotations, various other types of defects were also found on the edge, which are listed by the frequency-of-occurrence in the 40 images in descending order. The bond rotation was present in 31 out of 40 images (Figure 4-6a) in the exact same position. The individual pentagon was the second most frequently occurring structure (18 times), shown in Figure 4-6b. The 5-7-5 reconstructed edge (Figure 4-6c) and the double bond rotated structure (Figure 4-6d) both occurred 6 times. And the 555-8 structure (Figure 4-6e) which might go through several rotations and edge reconstructions, showed up 5 times. After the dislocation disappeared, none of these structures appeared in the remaining 14 images for 2 min 9 s as is shown in Figure 4-3f, indicating they are primarily caused by the dislocation. It is worth noting that bond rotations and defects can still occur at the edge of holes, without nearby dislocations, it is just that the frequency of occurrence drops dramatically. However, small holes have curvature effects, which are absent from large holes, and this can also increase the occurrence of bond rotations at the edge. The hole examined in Figure 4-6 was large enough that curvature did not play a major role.

4.2.4 Migration of dislocation to graphene edge

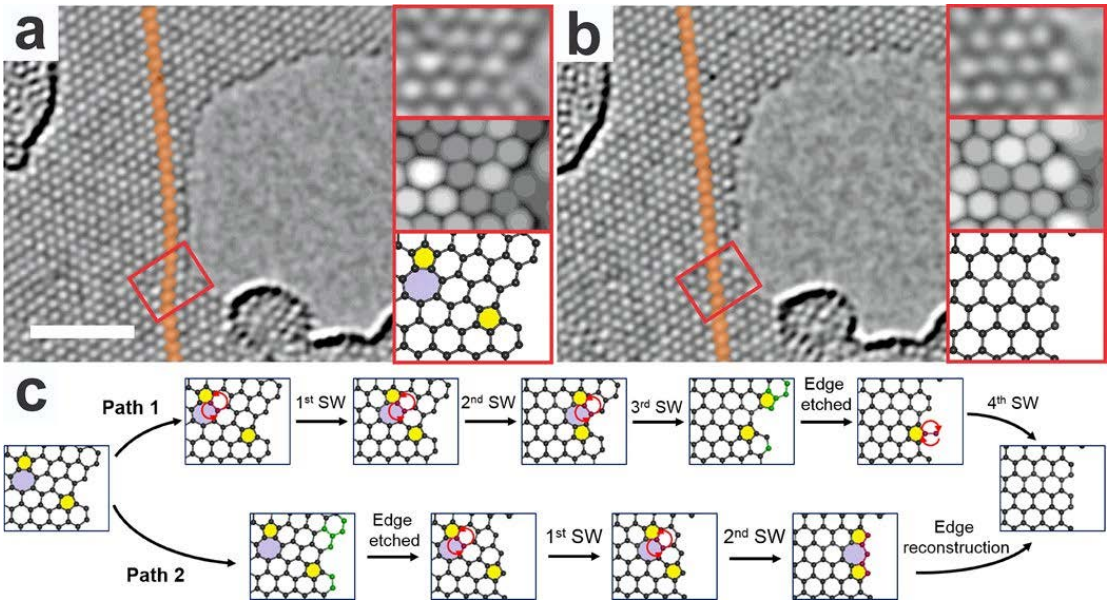

Figure 4-7. AC-TEM images taken (a) before and (b) after a dislocation disappeared, with magnified, maximum filtered views and atomic models presented in the insets. The time between two images is 67 s. The scale bar in panel a is 2 nm. (c) Atomic models showing two possible paths of how the dislocation glides to the edge. The color scheme in atomic models represent the number of carbon atoms in each ring, with 5 = yellow, 7 = blue. Orange lines indicate the distortion of the graphene lattice line is released when the dislocation is gone.

Figure 4-7 discusses some of the final structural pathways that could lead to the dislocation migrating to the edge. There are numerous ways in which the dislocation can make this journey, and therefore only simplest pathways are discussed here. Figure 4-7a shows the dislocation close to the edge, with the orange line indicting the curvature of the lattice, and in Figure 4-7b, the dislocation is gone and so too has the curvature. The disappearance of the dislocation between Figure 4-7a and b can be explained by several glides *via* bond rotation. Figure 4-7c gives two possible explanations. In path 1, three bond rotations occur first. As a result, the heptagon in the dislocation core disappears to the edge and the lattice distortion is released. After the

sputtering of the green atoms by the electron beam, the atoms highlighted in red are rotated to form a 6 member ring. Figure 4-7c shows a second path in which green atoms are etched first, followed by two bond rotations. Consequently, the lattice distortion is released and a 5-7-5 edge structure is formed. 5-7-5 then reconstructs into three hexagons with an additional carbon atom. Both pathways presented in Figure 4-7 require the dislocation to move along its glide plane through at least two bond rotations to reach the edge. Prior to this the dislocation remained fixed in its position. DFT and TBMD calculations (Figure 4-8) indicate that it is energetically favorable for the dislocation to glide toward the edge of graphene once it is close enough.

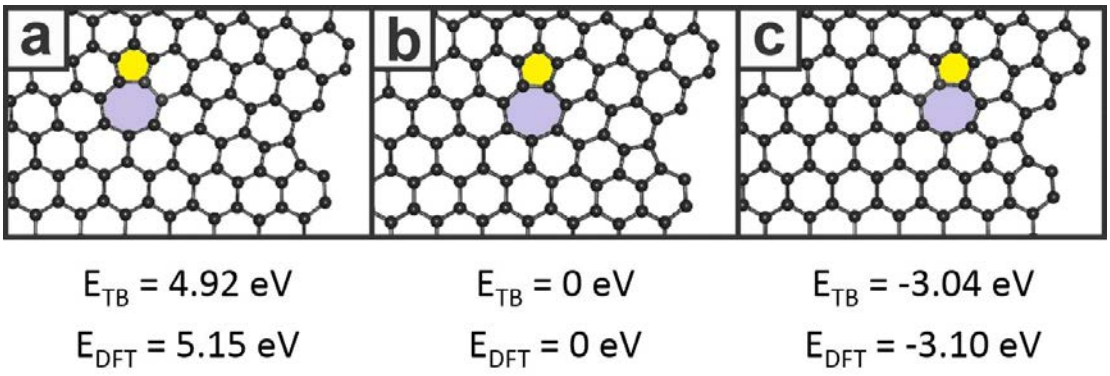

Figure 4-8. Tight-bonding molecular dynamics (TBMD) and DFT calculated relative formation energies for graphene with dislocations located at different positions near the edge, with the formation energy in panel b set to zero. The simulation results are provided by Professor Gun-Do Lee's group from Seoul National University.

4.3 Conclusions

The ability to track in real time two dislocations in graphene, one near a hole and another within the bulk, has allowed the understanding of local strain properties and how the dislocation affects the edge of graphene. The dislocation near the edge causes larger in-plane C–C bond rotations at the expense of reduced “hillocks” caused by out-of-plane distortions. Bond rotations at the graphene edge help alleviate the strain from the in-plane lattice rotations caused by nearby dislocations. Dislocations remained localized in their positions even to within a few lattice spacings of the edge, before it either glides toward the edge or the edge is sputtered all the way to the dislocation and it then disappears. These results provide important fundamental insights into the behavior of edge dislocations in graphene in the bulk and near the edge. The strain properties induced by the dislocation are substantially different when near the edge and highlight the sensitivity to the local structural environment.

Chapter 5

Thermally Induced Dynamics of Dislocations in Graphene at Atomic Resolution

5.1 Introduction

The exceptional electronic, magnetic, and mechanical properties of graphene can be modulated by introducing defects and excess-atoms. [1,5,9,175,177,178,184–186] Dislocations have higher stability against quenching compared with other intrinsic defects such as monovacancies and divacancies. [140,187] A dislocation in graphene can be annihilated through either the recombination of two opposite orientated dislocations or by gliding toward the edge of graphene. The movement of dislocations plays a crucial role in determining the macroscopic plastic deformation of materials, especially at elevated temperatures. Thus, understanding the atomic structure and dynamics of dislocations in graphene is of significant importance for developing a complete structure model. Various work over the years has revealed that the motion of dislocations in CNT and graphene is quite different from that in three-dimensional crystals. [139,140,188–192] The migration of dislocations in graphene normally occurs by Stone–Wales (SW) bond rotations (glide) or the loss of a carbon dimer (climb) at certain positions. Due to the high surface-to-volume ratio, dislocations are also found to introduce rippling (out-of-plane distortion) in free suspended graphene. [143,144,150,182,193] Despite the large amount of research in the structural study of

graphene, only few reports have focused on the high temperature dynamics of defects and dislocations in graphene and other carbon nanomaterials. Kotakoski *et al.* have studied the random walk and structural changes of divacancies in graphene under electron irradiation in an aberration-corrected scanning transmission electron microscope (STEM). [101] Suenaga *et al.* reported the direct imaging of pentagon-heptagon defects in a SWNT at equivalent temperatures of 2273 K, which are suggested to be responsible for the plasticity of the material. [194] He *et al.* have studied the atomic structure of graphene edges at different temperatures using both TEM and STEM and have proved the edge configuration in graphene is temperature dependent. [195] Huang *et al.* have also performed *in situ* HR-TEM experiments at more than 2000 °C and observed the superplasticity of SWNTs and the shrinkage of giant fullerenes. [196,197] The dynamics for the migration of isolated dislocations at elevated temperatures has not yet been explored.

Aberration corrected transmission electron microscopy (AC-TEM) has been a powerful tool in resolving the graphene lattice and controllably creating defects in graphene with a focused beam. With aberration correction and a monochromated electron source, it is possible to obtain a spatial resolution of 80 pm. [102,107,179,192,198,199] Experimental analysis suggests that operating TEM at or below an accelerating voltage of 80 kV could remarkably reduce electron irradiation damage to the graphene specimen, but does not prevent occasionally sputtering of carbon atoms and bond rotations. [64,66,73,77,134]

In this chapter, an *in situ* heating holder within an AC-TEM is utilized to study the atomic structure and dynamics of dislocations in graphene at different temperatures.

Defects were initially created by focusing the electron beam onto the sample using a previously reported approach and then searching for isolated dislocation cores to study. [73] An accelerating voltage of 80 kV is used to acquire atomic-resolution images with minimized knock-on damage when using a beam current density of $\sim 10^7\ e\ s^{-1}\ nm^{-2}$. The contribution of electron beam impacts to the dynamics of dislocations may not depend heavily on temperature, and by increasing the temperature, addition movement of dislocations associated with increasing thermal energy is detected.

5.2 Results and Discussion

5.2.1 Dislocation behavior at different temperatures

The pentagon-heptagon (5-7) configuration is the most commonly reported structure of a dislocation core in graphene. The migration of a dislocation can be accomplished by either a Stone-Wales bond rotation (a glide step) or the removal of a carbon dimer (a climb step). The bond-rotation driven dislocation glide was reported by Yakobson as early as 1998 in simulating the mechanical relaxation in CNTs. [188] In 2007, Ding *et al.* further showed that the pseudoclimb of dislocation also plays a role in the plastic elongation of CNTs. [189,190] The activation energy for a bond rotation is calculated to be 5 – 10 eV, depending on the local sp^2-bond configurations. [76,96] The density functional theory (DFT) calculation gives a value of 6.95 eV for a basic glide motion, which is significantly higher than the thermal vibration of the graphene lattice (0.068 eV), [78] and results in a dislocation at room temperature that is fixed in its position. Figure 5-1 is an example showing a dislocation that remains in its position over 7 min and 13 s. However, in some cases under 80 kV electron irradiation, a SW

rotation is induced by the electron beam, as is shown in Figure 5-1b,d. [98,200] Both rotated defects remain stable for more than 60 s, as the energy barrier for the SW rotation to unwind is ~ 5 eV.

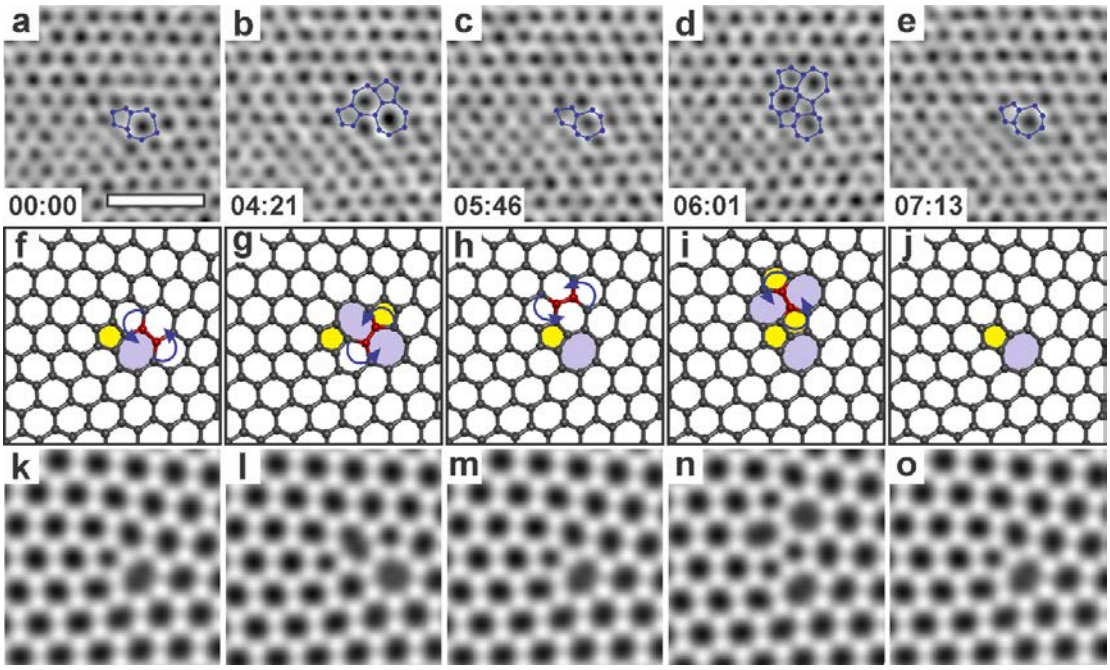

Figure 5-1. Beam-driven structural changes of a dislocation in graphene at room temperature. A total of 35 images were taken over 7 min and 13 s. (a–e) AC-TEM images showing the structural changes of a dislocation under electron irradiation. The lifetime of the structure shown in panels b and d is 73 ± 14 and 92 ± 14 s, respectively. (f–j) Atomic models of (a–e) with blue arrows and atoms highlighted in red indicating bonds that undergo a SW rotation in the next panel. The color scheme in the atomic models represents the number of carbon atoms in each ring, with 5 = yellow and 7 = blue. (k–o) Multislice simulated TEM images with 1 nm defocus and 4 nm defocus spread using the atomic models in (f–j), respectively. The scale bar in panel a is 1 nm.

Figure 5-2 shows a sequence of AC-TEM images of a dislocation core in graphene at 500 °C. The dislocation no longer stays immobile as it did at room temperature. It slowly shift its position by SW rotations, the trajectory of which is shown in Figure 5-2c. The migration path of the dislocation is one-dimensional restricted in the gliding

plane at 500 °C. Four glide steps in a time period of about 9 min occurred. No climb steps were observed at room temperature or 500 °C.

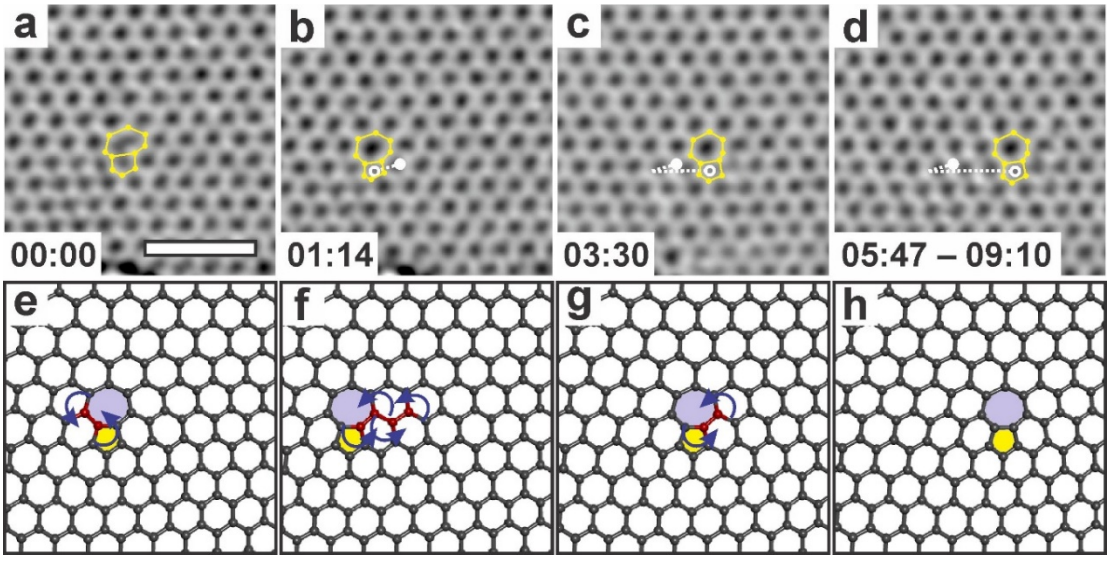

Figure 5-2. Migration path for a dislocation in graphene at 500 °C. A total of 39 frames were taken over a period of about 9 min and 10 s. (a–d) AC-TEM images showing the position of an isolated dislocation core. The trajectory is drawn by connecting the central point of the pentagon from each dislocation with white dashed lines. The start and end position are indicated by a filled and a hollow circle, respectively. (e–h) Corresponding atomic models. The scale bar in panel a is 1 nm.

When the temperature of the specimen is increased to 700 °C, dislocations start to move more rapidly *via* both bond rotations and removal of carbon dimers. The migration path of a dislocation at 700 °C in 13 min and 38 s is shown in Figure 5-3. The time interval between each AC-TEM frame is ~13 – 15 s. Only the frames in which the dislocation shifts its position and is relaxed to the form of isolated pentagon–heptagon are included in Figure 5-3 (Figure 5-3n is an exception for the dislocation directly glided to its position in Figure 5-3o without the bond rotation reverted). Twenty-four glide and eight climb steps are detected during the imaging period.

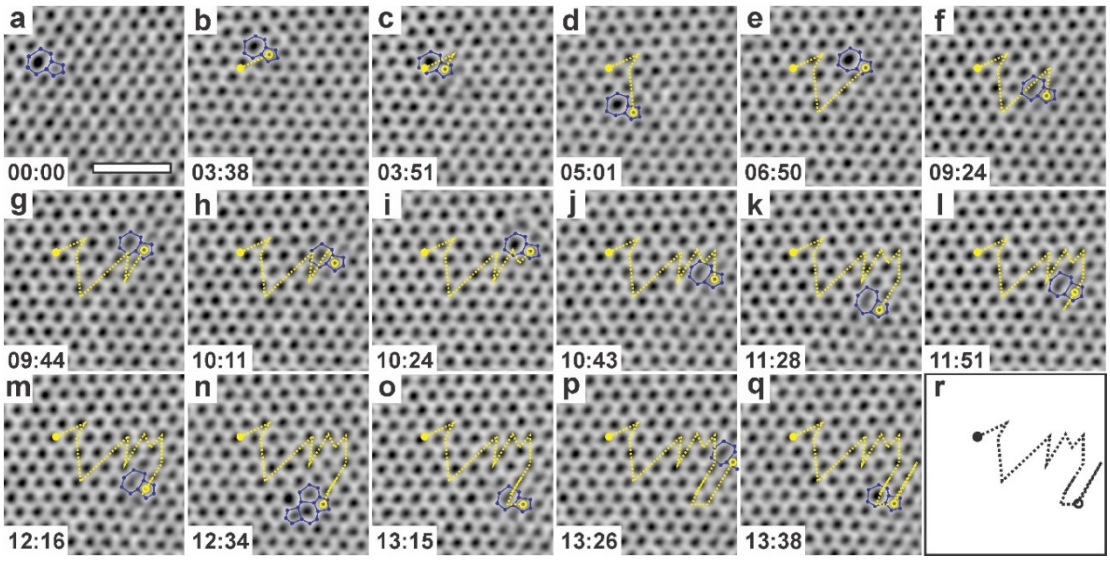

Figure 5-3. Trajectory of a dislocation in graphene at 700 °C. A total of 63 frames were recorded over 14 min and 30 s. Only those frames where the dislocation is in the form of an isolated pentagon–heptagon (expect panel n) are included. The scale bar in panel a is 1 nm.

The trajectory of the dislocation in Figure 5-3 is apparently different from the previously reported random walk of point defects in graphene. [101] This is due to the different mechanisms for the glide and climb behavior. The glide motion for the 5-7 dislocation occurs rigorously along the Burger vector *via* the rotation of a carbon dimer by 90° of its middle point (marked by the red ellipse in Figure 5-4a). Since there is no other defect nearby for the dislocations in Figure 5-2 and 3 to interact with, it is of equal probability for the dislocation to glide toward both directions in the slip plane. On the other hand, the climb motion is perpendicular to the slip plane, requiring the removal of a pair of carbon atoms (highlighted by the green ellipse in Figure 5-4a). Theoretically, a dislocation can climb toward the opposite direction by introducing two extra carbon atoms to the graphene lattice, which is however not observed in this specific study. This is probably because after the ejection of the first carbon atom, it requires far less energy to sputter the under-coordinated carbon atom, while

successively incorporating two carbon atoms into the graphene lattice is a more difficult process. Thus, all the climb components in the trajectory are in the same direction, which leads to the migration path schematically shown in Figure 5-4b with glide motions combined.

5.2.2 Mechanisms for dislocation behavior at elevated temperatures

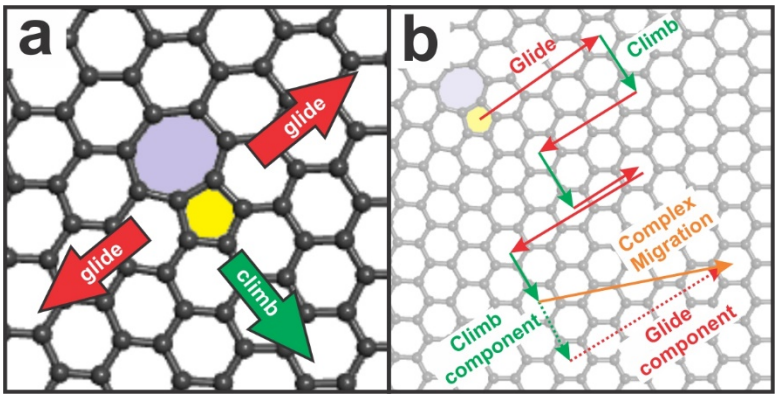

Figure 5-4. Schematic diagrams showing the possible migration directions for dislocations in graphene. (a) A dislocation can migrate along the gliding plane *via* bond rotations (basic glide step, indicated by the red arrows) or perpendicularly to the gliding plane *via* the removal of a carbon dimer (basic climb step, marked by the green arrow). (b) Schematic trajectory of a dislocation with both glide and climb motions involved. A complex migration step can be regarded as several equivalent basic glide and climb steps, which is particularly discussed in Figures 5-6–10.

Here, the theory for the dependence of both glide and climb steps on temperature is discussed. The behavior for dislocation glide can be explained by the two-dimensional diffusion. According to the definition of two-dimensional diffusivity, the diffusion coefficient is calculated by

$$D = \frac{\bar{\delta}^2}{4\tau}$$

where $\bar{\delta}$ is the average jump distance and τ the jump time. It is assumed that the glide motion over more than one lattice is accomplished by several separate basic steps. The jump distance of each step is approximately equivalent to the graphene lattice constant 0.24 nm. Some migration steps consist of both glide and climb behavior and only the displacement in gliding plane is taken into calculation. By analyzing the data in Figure 5-2 and 5-3, $D \approx 1.51 \times 10^{-4}$ nm^2 s^{-1} (773 K) and 4.10×10^{-4} nm^2 s^{-1}(973 K) is obtained. In this experiment, the glide motion of the dislocation is driven by both the thermal energy and electron beam irradiation. The relation between diffusion coefficient and experimental conditions is given by

$$D = D_0 \exp\left(-\frac{E_b}{k_\mathrm{B}T + E_{beam}}\right)$$

in which D_0 is the diffusion constant, $k_\mathrm{B} = 8.617 \times 10^{-5}$ eV/K the Boltzmann constant, E_b the diffusion energy barrier for a bond rotation which is 6.95 eV calculated by DFT. E_{beam} represents the contribution of electron beam in driving dislocation glide, while $k_\mathrm{B}T$ represents the contribution from thermal energy. As the number of scattering events is in proportion to the beam current density and the imaging condition (beam current density) is basically the same for experiments preformed at different temperatures in this chapter, E_{beam} can be treated as a constant. Putting the experimental measured diffusion coefficient into the equation gives

$$\frac{D_1}{D_2} = \exp\left(-\frac{E_b}{k_\mathrm{B}T_1 + E_{beam}} + \frac{E_b}{k_\mathrm{B}T_2 + E_{beam}}\right).$$

E_{beam} is the only unknown in the expression, solving gives $E_{beam} \approx 0.353$ eV.

The theory above can only be used to analyze the temperature-dependent glide motions. The climb behavior, however, needs to overcome a much higher energy barrier and further involves atom loss. It is studied by calculating the sputtering cross section using the analytical method developed by Meyer *et al.* [66] The minimum energy to sputter a three-coordinated carbon atom from the pristine graphene lattice is approximately 22 eV. [64–66,201] However, a dislocation introduces an out-of-plane distortion in the local area. The displacement threshold energies in curved area are calculated to be lower. [190] The threshold for removing a carbon atom from the pentagon in a 5-7 configured dislocation is calculated to be 2 – 3 eV lower. [139] Thus, in this work the threshold for a climb process is assumed to be 19 eV, which is used to calculate the sputtering cross section as a function of temperature, the result of which is shown in Figure 5-5 and Table 1. The cross section for sputtering a carbon atom in the pentagon is 40 – 600 times that in the perfect lattice, which explains why the atom loss is only observed in or next to the dislocation rather than the creation of new defects in the pristine lattice. The curve shows a strong positive correlation between the sputtering cross section with a 19 eV-threshold and specimen temperature, which provides theoretical support for the temperature-dependency of the climb motion.

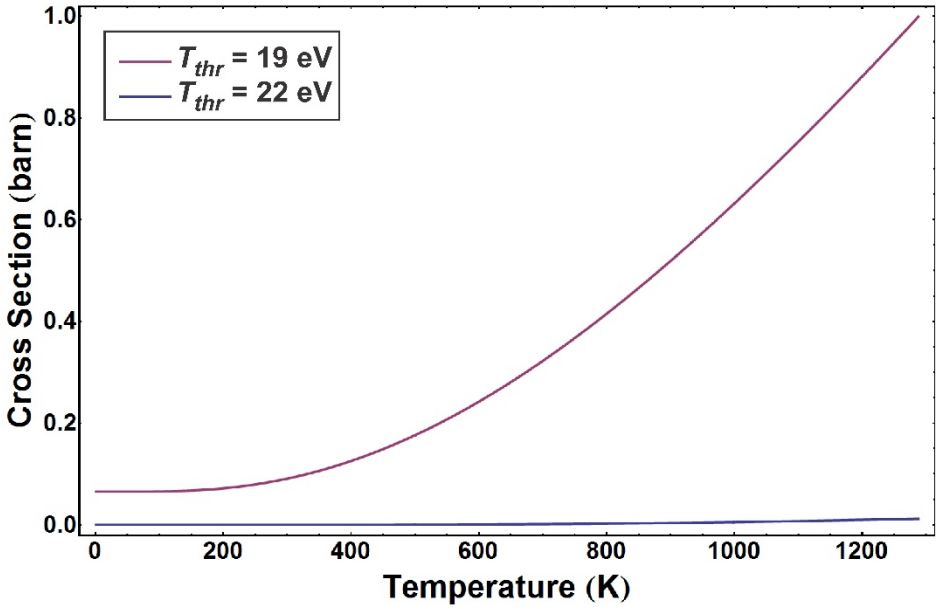

Figure 5-5. Dependence of carbon displacement cross section on temperature where sputtering threshold energy is 22 eV (blue) and 19 eV (red).

Table 5-1. Comparison of Displacement Cross Sections at Three Different Temperatures Where Thresholds Are 19 and 22 eV, Respectively

Temperature (K)		**293**	**773**	**973**
Sputtering Cross Section (barn)	T_{thr}**=19 eV**	0.0893	0.390	0.602
	T_{thr}**= 22 eV**	1.43×10^{-4}	5.84×10^{-3}	1.62×10^{-2}

5.2.3 Complex migration motions for dislocations

The higher frequency of dislocation motions at elevated temperatures allows more opportunity to study the detailed structural change of a dislocation in a migration process. It is observed that in the majority of cases the dislocation migration at elevated temperatures is still accomplished by basic glide and climb steps. However, in rare cases, the 5-7 dislocation reconfigures into a complex defect structure as an intermediate state during the migration process. A basic glide step is normally done by a SW bond rotation of two neighboring carbon atoms in the heptagon. However, at

500 °C, a complex glide step is observed in which two carbon atoms next to the dislocation core (highlighted in red in Figure 5-6d) underwent a SW rotation in the first place, forming a 555-777 defect structure (Figure 5-6e), which is reported to have a lower formation energy in carbon nanotubes. [142] The defect can be regarded as the assembly of 5-7 dislocation and a SW defect, or three adjacent dislocation cores. With the SW defect on the left side unwound, the dislocation shifted two lattices away from its original position. The same process has been reported by Lehtinen *et al.* in the TEM imaging of graphene at room temperature using a higher beam current density of 1×10^8 e s^{-1} nm^{-2}. [139]

The climb process could occur in a similar way at 700 °C by generating a complex defect as an intermediated structure. In Figure 5-7, a SW rotation next to the dislocation core first took place (Figure 5-7d), forming a defect structure (Figure 5-7e) which could be seen as the assembly of a 5-7 dislocation and an inversed-Stone–Wales (ISW) defect (the 7557 structure in the dashed ellipse). After the removal of the highlighted carbon dimer in Figure 5-7e, the defect eventually annealed back to a normal dislocation core, as shown in Figure 5-7c,f. The whole process is equivalent to one basic glide plus one basic climb step.

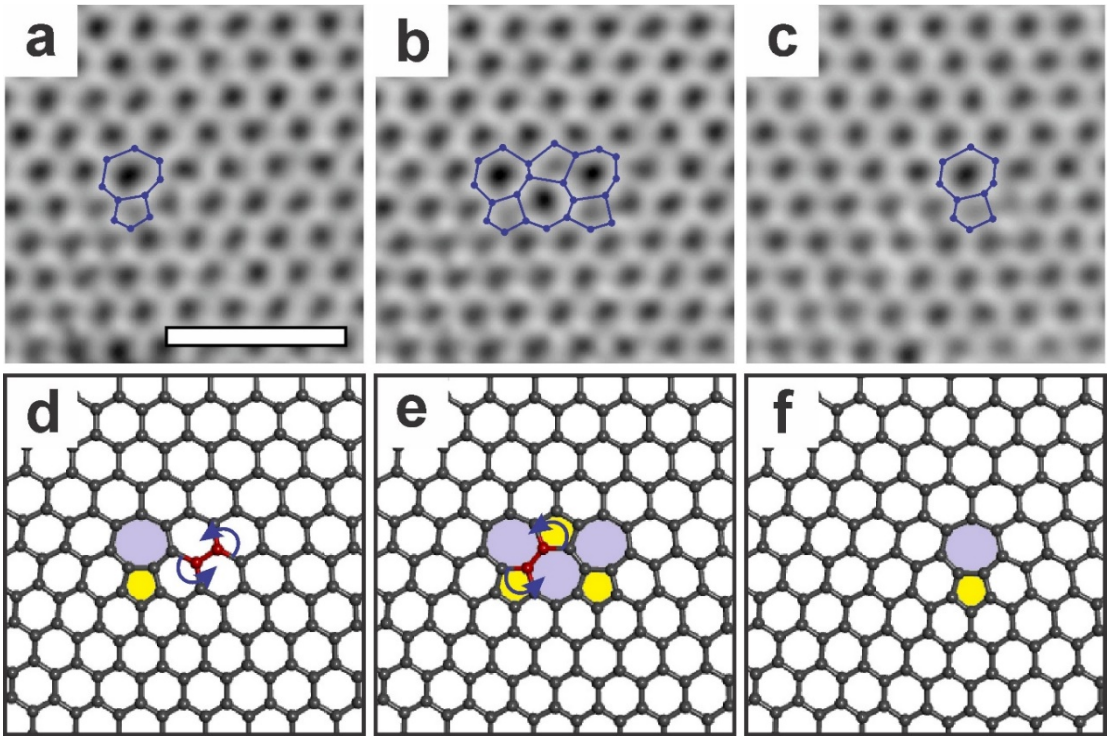

Figure 5-6. Complex glide of a dislocation in graphene at 500 °C. (a) AC-TEM image of a pentagon–heptagon configured dislocation core. (b) A SW rotation next to the dislocation leads to the formation of three adjacent dislocation cores. (c) The SW defect on the left side is relaxed, leaving a dislocation two lattice away from its original place. (d–f) Atomic models corresponding to the TEM images. The scale bar in panel a is 1 nm. The color scheme in the atomic models represents the number of carbon atoms in each ring, with 5 = yellow and 7 = blue.

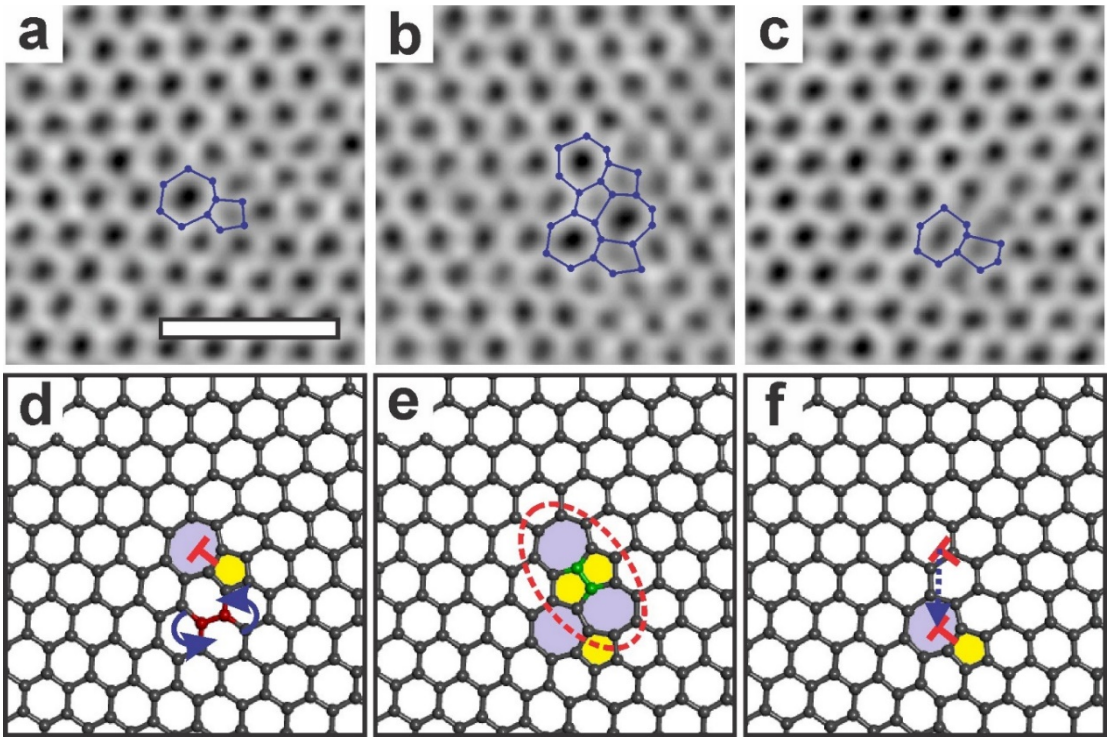

Figure 5-7. Complex migration of a dislocation at 700 °C. (a) Gaussian-filtered AC-TEM image of a 5-7 dislocation. (b) An evolved dislocation structure following a SW rotation. (c) The removal of a carbon dimer transforms the structure back to a 5-7 dislocation. (d–f) Atomic models corresponding to panel a–c. Bonds that undergo a SW rotation in the next panel are highlighted in red and by the blue arrows. Atoms to be removed are highlighted in green. The scale bar in panel a is 1 nm. The color scheme in the atomic models represents the number of carbon atoms in each ring, with 5 = yellow and 7 = blue.

The energy barrier for this process is calculated using DFT. The result is shown by the blue curve in Figure 5-8, with two different possible pathways as a comparison. It is revealed that a bond rotation next to the dislocation core needs to overcome an energy barrier 1.27 eV higher than the bond rotation associated with a basic glide step. On the other hand, the energy barrier for evaporation of the highlighted dimer in the 7557-57 defect in Figure 5-6e is 1.12 eV lower than a basic climb motion. This is in accordance with the previous work which reported the instability and a relatively short lifetime of an ISW defect under electron irradiation. [116] The total formation energy of the system does not change much after the bond rotation but is increased by 12 – 13 eV after the dimer sputtering, which explains why the bond rotation is more frequently observed in this experiment than atom displacement.

Figure 5-9 and 5-10 are two examples showing more complex evolution of dislocations under electron irradiation at 700 °C. A dislocation core in Figure 5-9 a first underwent carbon dimer sputtering in the pentagon, leading to the formation of a 5-77-5 defect (Figure 5-9b). A further SW rotation transformed the structure into an irregular configuration consisting of three pentagons and three heptagons as is shown in Figure 5-9c. The defect subsequently relaxed to the 5-7 configuration and migrated to its position in Figure 5-9d. A probable order of four SW rotations for this transformation is illustrated schematically by the atomic models in Figure 5-9g–j.

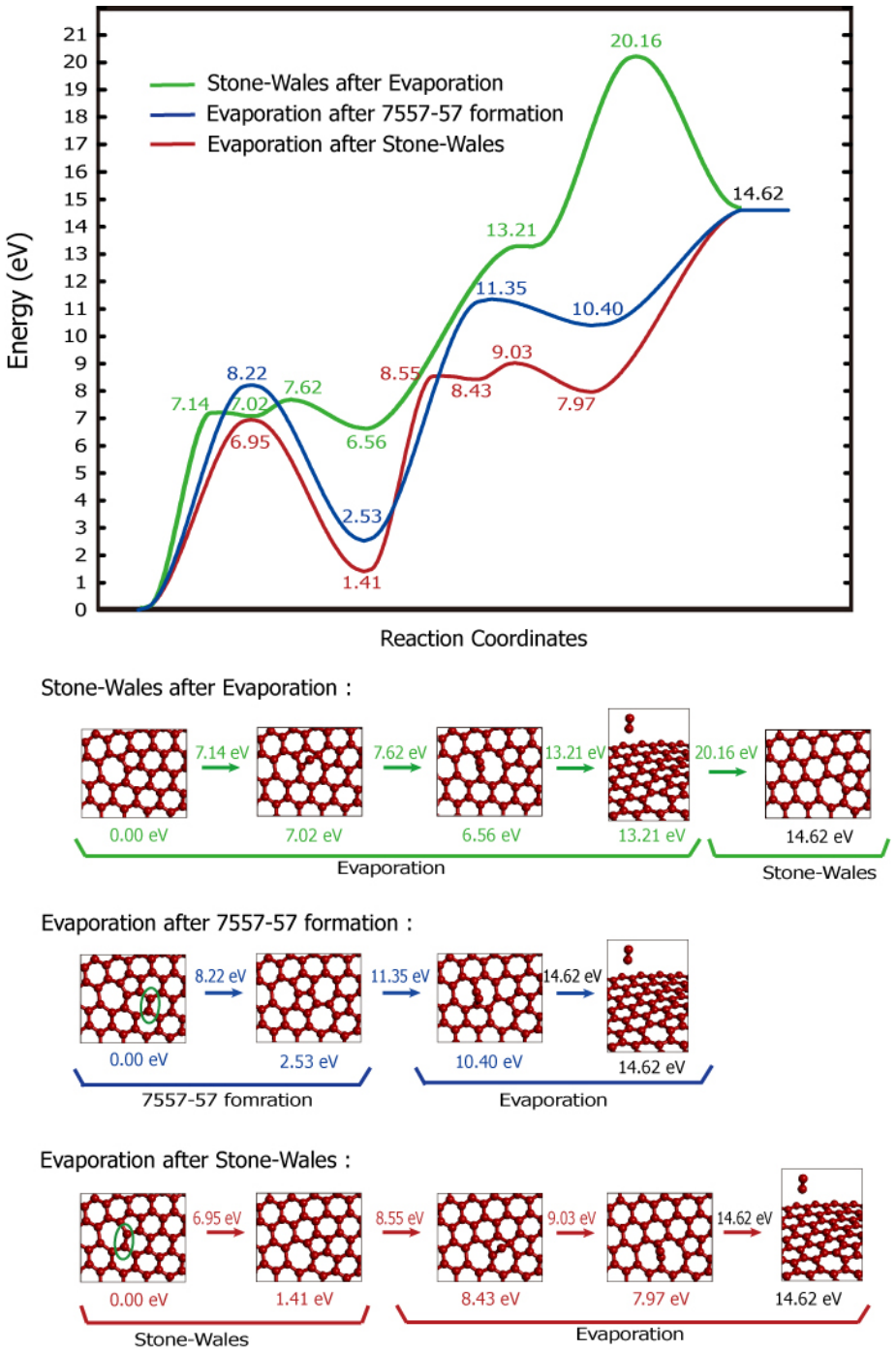

Figure 5-8. Density functional theory (DFT) simulations showing the energy barrier of different pathways for the structural change in Figure 5-7. The green curve indicates the pathway in which a SW rotation in the heptagon occurs before the evaporation of a carbon dimer and the red curve otherwise. The mechanism observed in Figure 5-7 is indicated by the

blue curved line. The simulation results are provided by Professor Gun-Do Lee's group from Seoul National University.

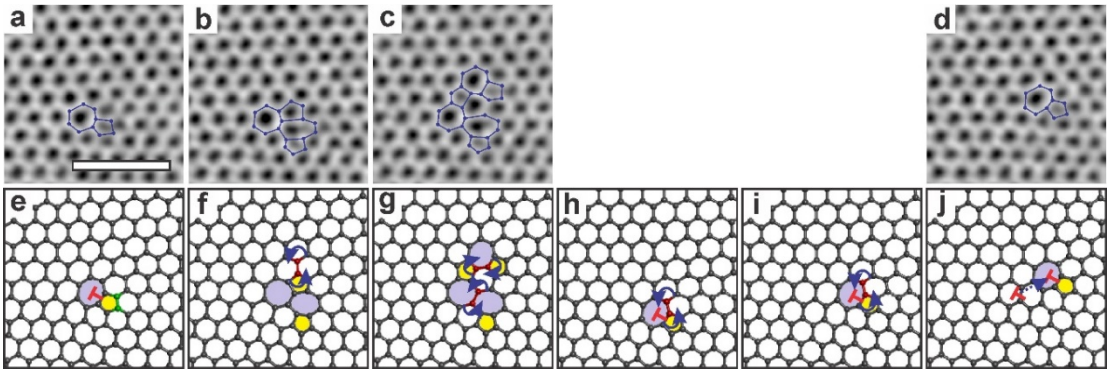

Figure 9. Another example showing a complex migration process at 700 °C. (a) Filtered AC-TEM image of a dislocation core. (b) A 5-77-5 defect after the sputtering of two atoms in the pentagon. (c) An irregular defect structure after two SW rotations, before annealing to the 5-7 dislocation in (d) *via* a few more rotations. (e–g, j) Atomic models for the corresponding TEM images. (g–j) A probable path way for the detailed structure reconfiguration between the defects in panel c and d. The scale bar in panel a is 1 nm.

In Figure 5-10, one climb step accomplished by the successive sputtering of two nonadjacent carbon atoms is observed. The migration process started from the formation of a 5-8-5 divacancy next to the dislocation (Figure 5-10a). The defect then evolved into a metastable configuration with bridging atoms (Figure 5-10c), following the sputtering of one single carbon atom highlighted in green in Figure 5-10h. It has been previously proposed that under-coordinated carbon atoms in bridging positions play a role in stabilizing odd numbered vacancies under electron irradiation. [102] After the removal of a further atom in Figure 5-10i, the defect reconfigured into the same structure in Figure 5-10h. The atomic models in Figure 5-10h–j can also be regarded as a climb step for the 7-55-8-5 configured dislocation. Afterward, the dislocation transformed to a 5-77-5 structure (Figure 5-10e) before finally quenched to the 5-7 configuration (Figure 5-10f). The reconfiguration between Figure 5-10d

and Figure 5-10e cannot be achieved by merely SW rotations. Figure 5-10j–m suggests a possible pathway, in which bonds with red crosses in Figure 5-10j broke initially, followed by the rotation of the red bonds (Figure 5-10k) and their rebonding with the under-coordinated carbon atoms.

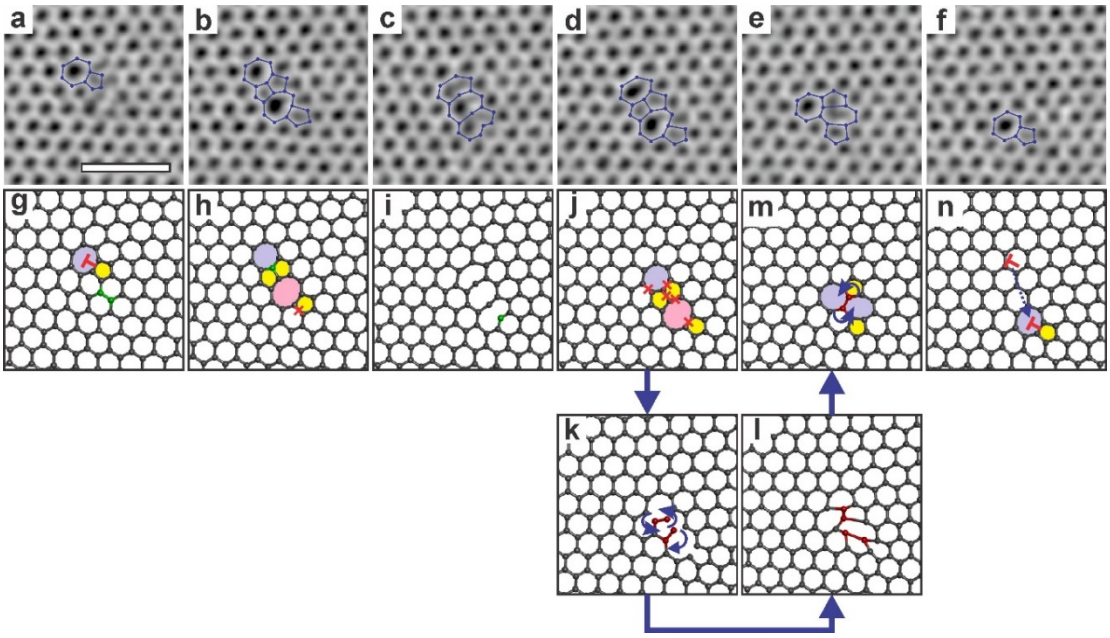

Figure 5-10. Complex migration of a dislocation at 700 °C *via* the formation of an intermediate structure with bridging atoms. (a) AC-TEM image showing an isolated dislocation core. (b) A 5-8-5 divacancy formed next to the dislocation. (c) The removal of a carbon atom leads to the formation of a defect with bridging atoms. (d) A further atoms is sputtered, yielding to the same defect in panel b. (e) A 5-77-5 defect formed after breakage and rotation of bonds. (f) A finally quenched dislocation core. (g–j, m, n) Atomic models corresponding to the TEM images. (j–m) A possible pathway for the structural change between panels d and e. The scale bar in panel a is 1 nm.

5.2.4 Large-scale jump of dislocations

Apart from the step by step random walk, large-scale jumps of a dislocation are also observed between sequential frames. Figure 5-11a shows a large jump of a dislocation at 500 °C, over a distance of 2.9 nm. The mechanisms for the large jump are likely to

be different from the theories discussed above, as the migration rate is at least 100 times higher. The migration distance is equivalent to 12 basic glide and 1 basic climb steps. It is worth noting that the glide direction for the dislocation in Figure 5-3 is randomly distributed, while the large motion consists a dozen of glide steps toward the same direction. Thus, this large migration movement is more likely driven by the Peierls stress resulting from the different thermal expansion between the graphene sheet and Si_3N_4 substrate at elevated temperatures.[202] Further work is still required to gain a deeper understanding of this phenomenon. Figure 5-11c–f gives two more cases at 800 °C, indicating the long-distance glide at 500 °C is not an isolated event.

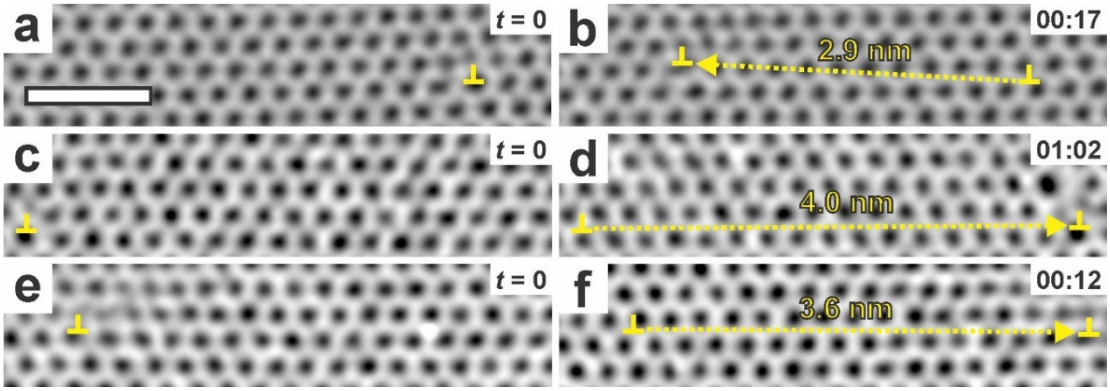

Figure 5-11. AC-TEM images showing the long-distance glide steps of a dislocation. (a and b) Two consecutive frames taken at 500 °C with a time interval of 17 s, showing a large glide motion of a dislocation core over 2.9 nm. (c–f) Two more examples of the large glide motions taken at 800 °C, where the time interval is 62 and 12 s and jump distance is 4.0 and 3.6 nm, respectively. The scale bar in panel a is 1 nm.

5.3 Conclusion

This chapter investigates the atomic-scale configuration and motion of dislocations in graphene as a function of temperature, using an *in situ* heating holder within an AC-TEM operated at 80 kV. An increase in the specimen temperature accelerates both glide and climb motions, revealing for the first time temperature driven dynamics of dislocation cores at the atomic level. Instead of the basic glide and climb processes, the dislocation migration sometimes takes the form of a complex defect as a metastable structure. The instantaneous slip of a dislocation over more than 10 lattices in the heated graphene shows substantial dynamics are occurring in the system that might be active by applying stress fields to change the strain. By presenting the detailed study on high temperature stability of dislocations in graphene, this work may provide insights into future studies in defect-related nanoengineering and property modification in graphene.

Chapter 6

In Situ Atomic Level Dynamics of Heterogeneous Nucleation and Growth of Graphene From Inorganic Nanoparticle Seeds

6.1 Introduction

Chemical vapor deposition (CVD) of graphene on Cu substrates has been a promising method to synthesize large area graphene with industrial scalability. [29,177,203–206] Graphene domains nucleate on the Cu surface and grow larger as precursor feedstock is supplied until they eventually merge together to form a continuous polycrystalline film. [207] The formation of graphene domains can be either from heterogeneous and homogeneous nucleation processes. Heterogeneous nucleation involves using seeds, often particles, to lower the precursor concentration threshold for nucleation to occur compared to homogeneous nucleation. [162,208] Understanding these initial nucleation processes of graphene domains is critical for developing new synthetic strategies for CVD growth of high quality graphene continuous films. Previous results have shown that individual graphene domains can be single crystals, but in some cases are polycrystalline. [29,162,209–211] Having polycrystallinity from a single domain region significantly increases the number of grain boundaries (GB) in the final continuous films of graphene as the domains merge together.

The GBs can impact the mechanical, electrical, and chemical properties of graphene. [47,124,156–163] The atomic structure of dislocations and GBs in graphene has been investigated in both experimental and theoretical calculations, primarily for the potential application in device fabrication and nanoengineering. [56,128,139,140,150,187,191,212–215] In 1988, Albrecht *et al*. reported the observation of tilted GBs in graphite using scanning tunneling microscopy (STM). [216] It was not until many years later that the atomic structure comprised of arrangements of pentagon-heptagon (5-7) edge dislocations was revealed by high resolution transmission electron microscopy (TEM) experiments. [129] Similar results were later achieved by multiple TEM and STM observations. [151–153] The formation of 5-8-5 linear GBs has also been reported in polycrystalline graphene grown on Ni (111) substrate due to the strong graphene-substrate interaction. [109] Experimental studies of the atomic level migration of a GB using an aberration-corrected TEM (AC-TEM) revealed migration mediated by bond rotations, however *ab initio* theoretical calculations indicate that GBs can also migrate by evaporation of a carbon dimer. [152,155] After high temperature annealing (600 °C), curved and aperiodic GBs in CVD grown graphene reconstruct into straighter and periodic forms. [153] *In situ* experiments within a TEM at high temperatures of 2000 K by Joule heating found carbon adsorbates on monolayer graphene transformed into polycrystalline graphene domains separated by GBs. [154]

Prior work using AC-TEM to study *in situ* growth of graphene has shown that carbon can attach to pre-existing edges of graphene to further continue its growth. Liu *et al*. reported the *in situ* growth of a second-layer graphene inside a AC-TEM from the step

edge of an existing domain under beam irradiation. [217–221] The crystallinity and growth rate of the newly grown area were shown to be temperature dependent, with single silicon atoms located at the step edge suggested to act as a catalyst for the second layer of graphene growth from hydrocarbons. [152] Homogenous nucleation of small graphene seeds is often studied by STM and can reveal the transition from a molecular disordered cluster to small crystalline fragments of sp^2 carbon. [222] However, there are hardly any atomic level studies related to heterogeneous nucleation of graphene domains from seeds, such as metal nanoparticles.

In this chapter, an *in situ* heating holder within an AC-TEM is utilized to study the heterogeneous nucleation and growth of graphene from metal nanoparticles seeds. The growth of the graphene domain size in regards to the site-specific addition of carbon atoms and the GB transformations that underpin the increase in crystallinity of the domains are also studied. The initial graphene was synthesized by ambient pressure CVD method using melted copper on molybdenum substrate as the catalyst as described in Chapter 3.The graphene sheet was subsequently transferred onto a Si_3N_4 grid designed for *in situ* high temperature TEM experiments (DENSsolutions). The heating holder allows the accurately control of specimen temperature from room temperature to 800 °C and capture detailed real-time dynamics.

6.2 Results and discussion

6.2.1 *In situ* growth of a second layer of graphene

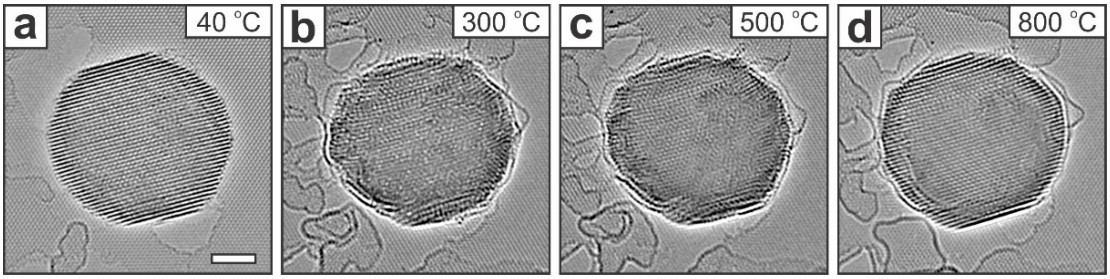

Figure 6-1. AC-TEM images of a Au nanoparticle sitting on a multilayer graphene sheet in the temperature range between 40 and 800 °C. The scale bar in panel a is 3 nm.

Monolayer graphene was first heated up to 800 ˚C inside the TEM using the *in situ* heating holder (Figure 6-1a), which causes the amorphous carbon surface adsorbates to evaporate and reveal the lattice structure of graphene. This effect has also been described with more detail in previous experiments. [195,223] However, an increase in the specimen temperature causes the metal nanoparticles to be encapsulated with carbon "graphitic" shells. [224] Figure 6-1a shows a nanoparticle with radius of ~ 10 nm at room temperature supported on a multilayer graphene sheet. Energy-dispersive X-ray spectroscopy (EDX) taken on the nanoparticle shows they are Au (Figure 6-2). The Si atoms from contamination during the CVD growth and transfer process may also be present in the nanoparticle. When the temperature is raised to 300 °C, the nanoparticles start to get encapsulated by few-layered graphene fragments as shown in Figure 6-1b. No apparent change happens to the core-shell structure when the specimen temperature is further increased to 500 and 800 °C (Figure 6-1c,d). Early research has shown that the melting point of Au nanocluster drops below 800 °C when the particle radius is < 3 nm. [225] Accordingly, the Au nanoparticle with ~ 5 nm diameter in

Figure 6-3a appears amorphous and partially evaporated when the specimen is heated to 800 °C, thus revealing the boundary of the carbon shell and the particle before melting. 600 °C was found to be the optimal temperature where hydrocarbons attach to the seed and begin to slowly grow graphene. At 800 °C, the rate of graphene growth basically reached an equilibrium with the etching of edge atoms and the formation of a secondary layer of graphene is limited.

According to the classical nucleation theory, heterogeneous nucleation is much more commonly observed as oppose to homogeneous nucleation and the reaction process is also much faster due to the lower nucleation energy barrier. In the case of the *in situ* high temperature graphene growth in the AC-TEM, electron beam irradiation of the pristine monolayer graphene area did not lead to the formation of a secondary layer of graphene on top. However, around the Au particles a secondary layer of graphene nucleates swiftly and continues to grow at 600 °C. Figure 6-3a–d shows a time series of secondary layer growth with the underlying monolayer graphene removed from image using a mask filter in the Fourier transform, similar to those shown in Figure 6-5 and 6-7. The growth rate is shown in Figure 6-3e by plotting the area of the secondary layer with time for all 39 frames over 8 min 41 s. Excluding the odd first point, the results exhibit an excellent linear relationship. The growth rate obtained from the slope of the linear equation is 0.14 nm^2/s. This relatively slow growth rate enables the dynamic study of the growth frontier.

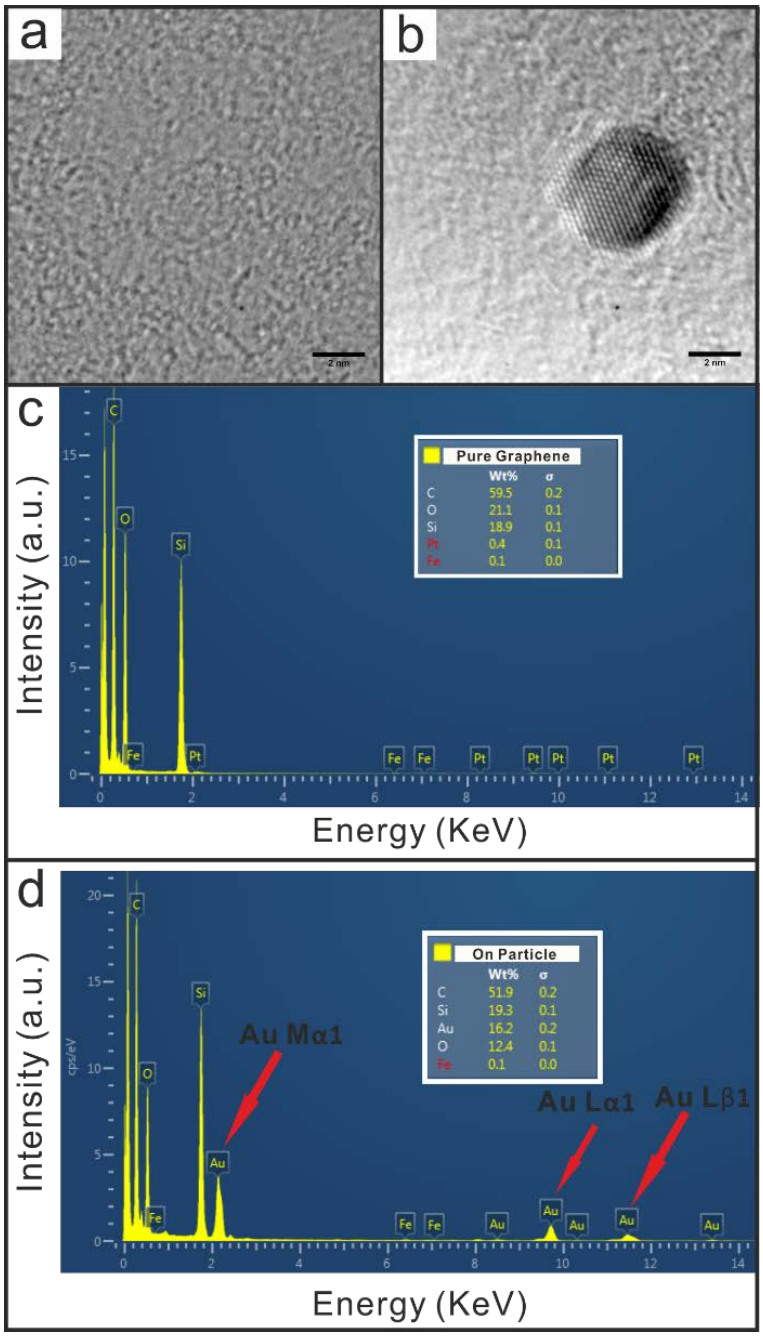

Figure 6-2. EDX characterization of nanocrystals on graphene sheet. (a) TEM image of monolayer graphene covered with amorphous carbon adsorbates at room temperature. (b) TEM image of a nanocrystal sitting on top of the amorphous carbon. (c, d) EDX spectrums of the areas shown in (a) and (b), with the weight percentage and standard deviation listed in the insets. The scale bars in panel a and b are 2 nm.

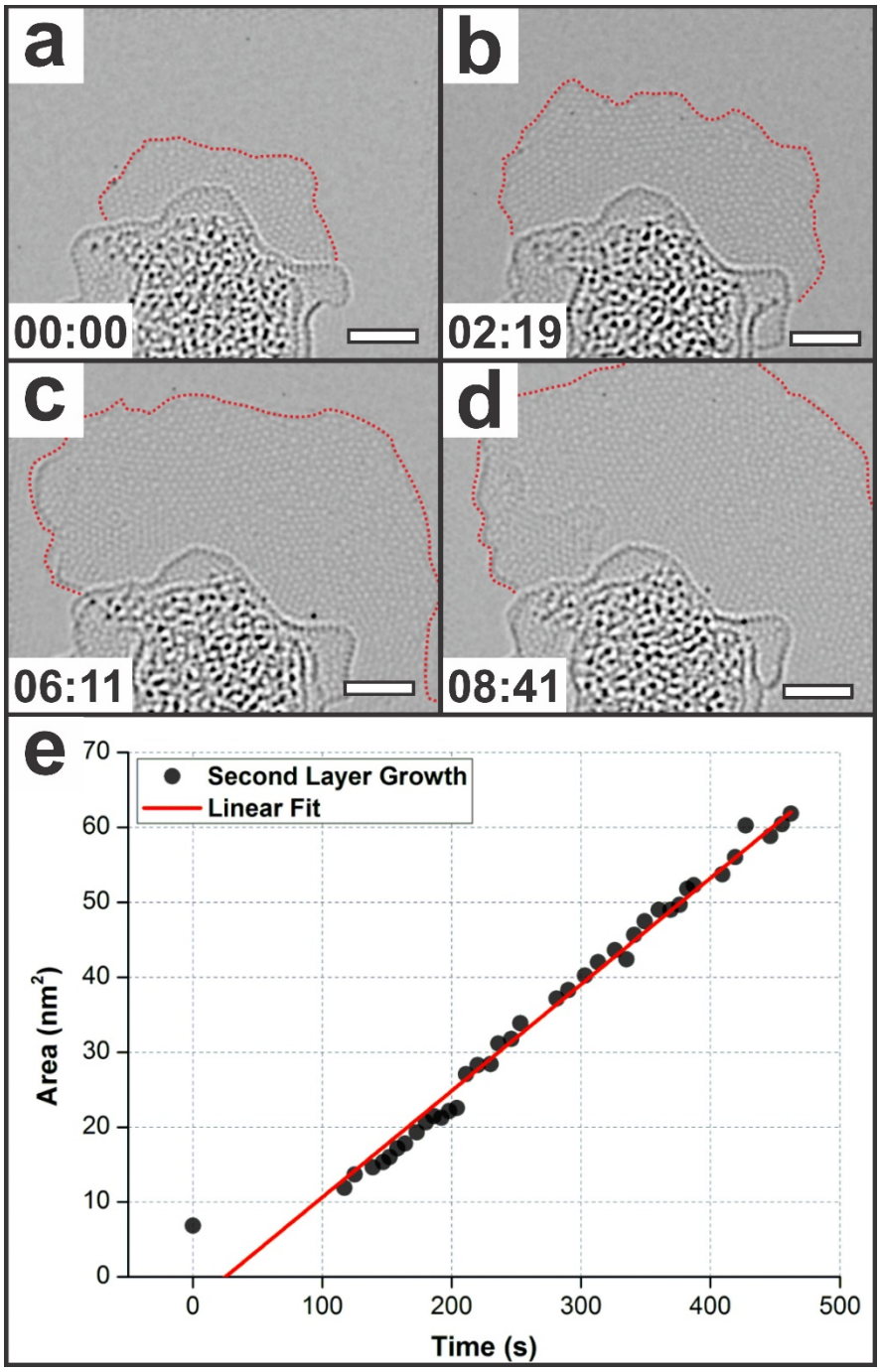

Figure 6-3. (a–d) Time series of AC-TEM images showing the growth of a secondary graphene layer from surface adsorbate attachment. The frontier for the second layer is shown by the red dotted lines. The underlying monolayer graphene has been removed from the images using a filter mask in the Fourier transform. All scale bars = 3nm. (e) The area for the as-grown second layer is plotted against time.

6.2.2 Mechanism for second layer growth

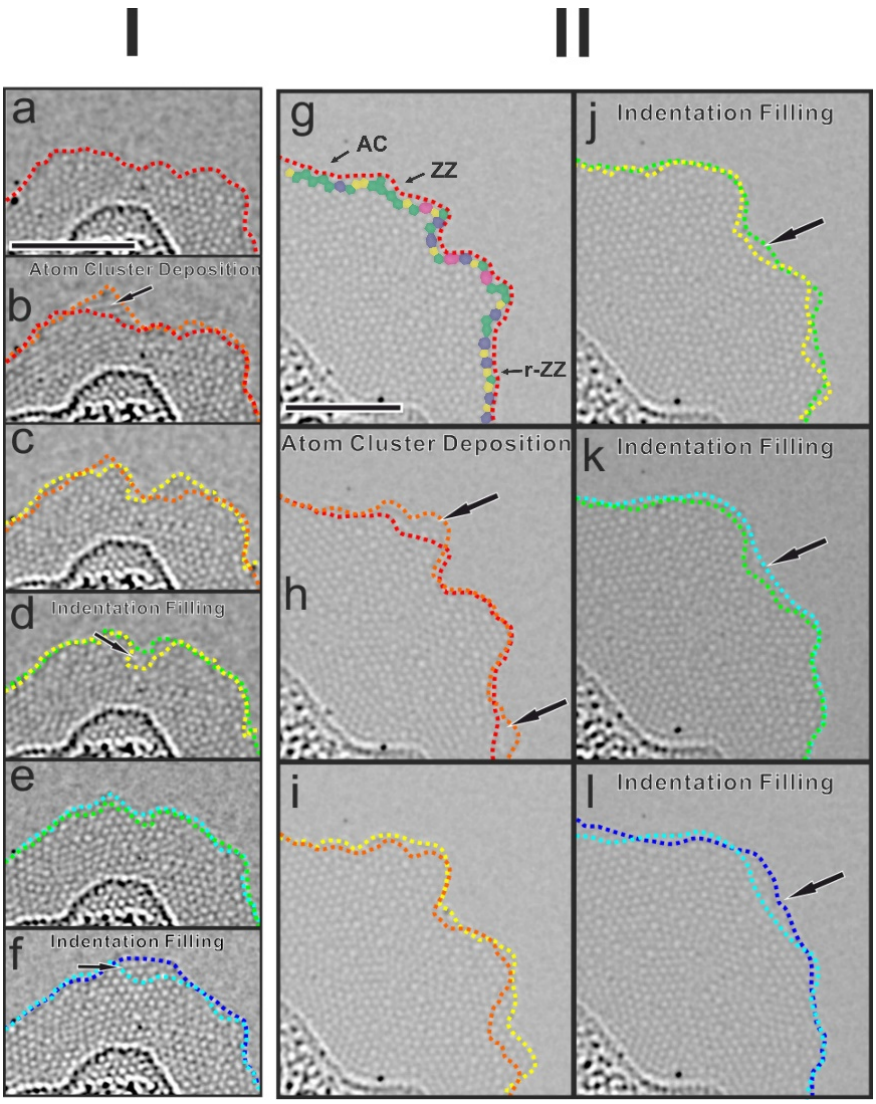

Figure 6-4. Two different examples, (a–f) and (g–l), showing *in situ* atomic level dynamics of the graphene edge growth. The time series of AC-TEM images show the cluster addition of C atoms to the edges of amorphous graphene domains. Time between frames is ~ 10 s. The perimeters are color coded differently to allow visual comparison between the two consecutive frames. The color scheme in panel g represents the number of carbon atoms in each ring at the edge, with 5 = yellow, 6 = green, 7 = blue and 8 = pink. All scale bars = 3 nm. The underlying monolayer graphene has been removed by a filter mask in the Fourier transform.

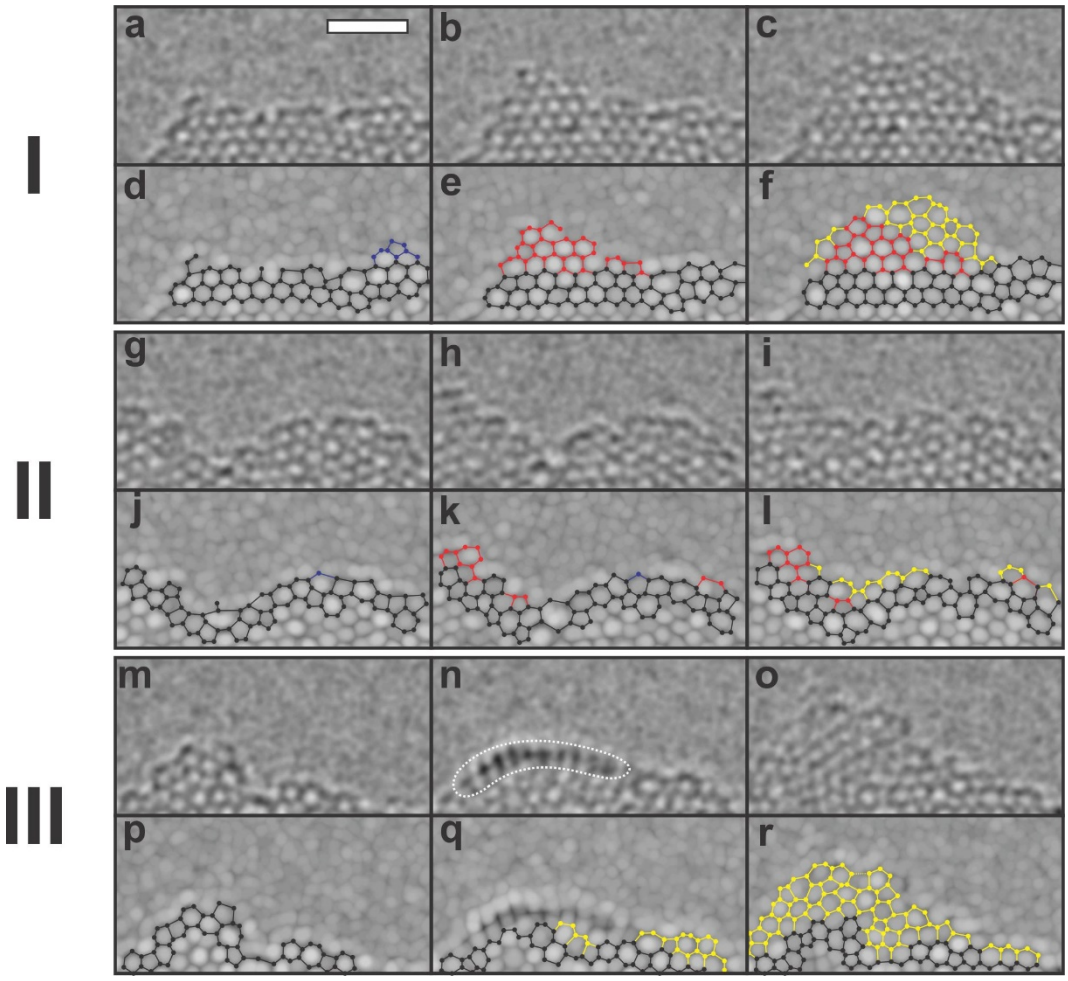

Figure 6-5. Another three sets of sequential AC-TEM images showing the edge growth and reconstruction of the second layer of graphene at higher magnification: (a–c) carbon cluster deposition. (g–i) indentation filling. (m–o) back-folding of the edge. Time between frames is ~ 10 s. (d–f),(j–l) and (p–r) Corresponding maximum filtered images with original edges colored in black. Atoms attached to the edge in next frames are colored in red and yellow. Edge atoms to be etched are highlighted in blue. The scale bar in panel a is 1 nm.

The growth front is carefully studied to gain a deeper understanding of how the domain gradually expands its size atom by atom. At first glance, the advance of the growth front is accomplished by alternate “carbon cluster deposition” and “indentation filling”, shown in Figure 6-4. For example, in Figure 6-4a–f, where the time series of AC-TEM images are examined, a cluster of atoms adds onto the pre-existing graphene to continue

the growth process, indicated by the arrow Figure 6-4b. This leads to the roughening of the edge in this local region and subsequent frames show that further atom cluster deposition fills in around this to smooth the edge back out. This process of "indentation filling" is highlighted in Figure 6-4d,f and a second example is presented in Figure 6-4g–l.

Here, the theory for the *in situ* growth of the second layer of graphene is discussed. The dependence of growth rate on temperature, beam current density and residual hydrocarbon gas pressure has been well investigated in Liu *et al*.'s previous research. The experiment in this chapter was carried out under similar conditions and the obtained growth rate (0.14 nm^2/s) in Figure 6-3 is also comparable to their results. However, apart from the zigzag (ZZ), armchair (AC) and reconstructed zigzag (r-ZZ) edges, the growth front also contains certain amount of nonperiodic structure and even some octagons (Figure 6-4g), which leads to poorer crystallinity of the top graphene layer compared with the previous work. The crystallinity and atomic structure of the second layer will be discussed with more detail in Figure 6-8. Here, two possible explanations are provided which are (i) the carbon shells in Figure 6-3 acting as the initial seeds for the *in situ* growth are not well crystallized and show lots of nonhexagonal rings indicative of amorphous 2D carbon or highly defective graphene, which could give rise to similar atomic structure in the newly grow area around it, or (ii) the hydrocarbon gas concentration near the Au nanoparticle is slightly oversaturated, resulting the increase desorption rate of carbon adatoms and the lack of time to form a periodic and low energy edge structure. Research on CVD graphene

growth has shown that the growth limiting step for the reaction is the attachment of carbon adatom species to the graphene edge and the rate of this step can be given by:

$$R \propto \exp\left(-\frac{E_{\mathrm{b}}}{k_{\mathrm{B}}\mathrm{T}}\right)$$

where E_{b} is the free energy barrier, k_{B} is the Boltzmann constant and T is the experimental temperature. [207] The energy barriers to attach carbon adatoms to a pristine ZZ and AC edge are 2.19 and 2.47 eV respectively. [226] The stability of r-ZZ edge lies between them. [227] Thus, it is energetically favorable to first incorporate carbon atoms onto the ZZ and r-ZZ edge when the growth front is smooth, which matches the observation shown in Figure 6-4g and h (carbon cluster deposition).

Figure 6-5a–c shows examples at higher magnification where carbon clusters containing 32 and 39 atoms are successively attached to the ZZ edge of graphene in the next two consecutive frames. The added carbon atoms may come from the edge structure colored in blue in Figure 6-5a, which is subsequently etched under electron irradiation, indicating that the reconfiguration of newly attached structure also takes place during the growth process. When the curvature of the growth front exceeds a certain value, filling the indentation sites becomes preferable since the decrease in surface energy partially compensates the barrier, which is also experimentally observed in Figure 6-4d–f, j–l and Figure 6-5g–i. This provides theoretical basis of why the *in situ* graphene growth is an alternating process of ‘carbon cluster deposition’ and ‘indentation filling’, rather than a uniform process in all directions by single atom attachment at all edge sites.

6.2.3 Back-folding of a second layer of graphene

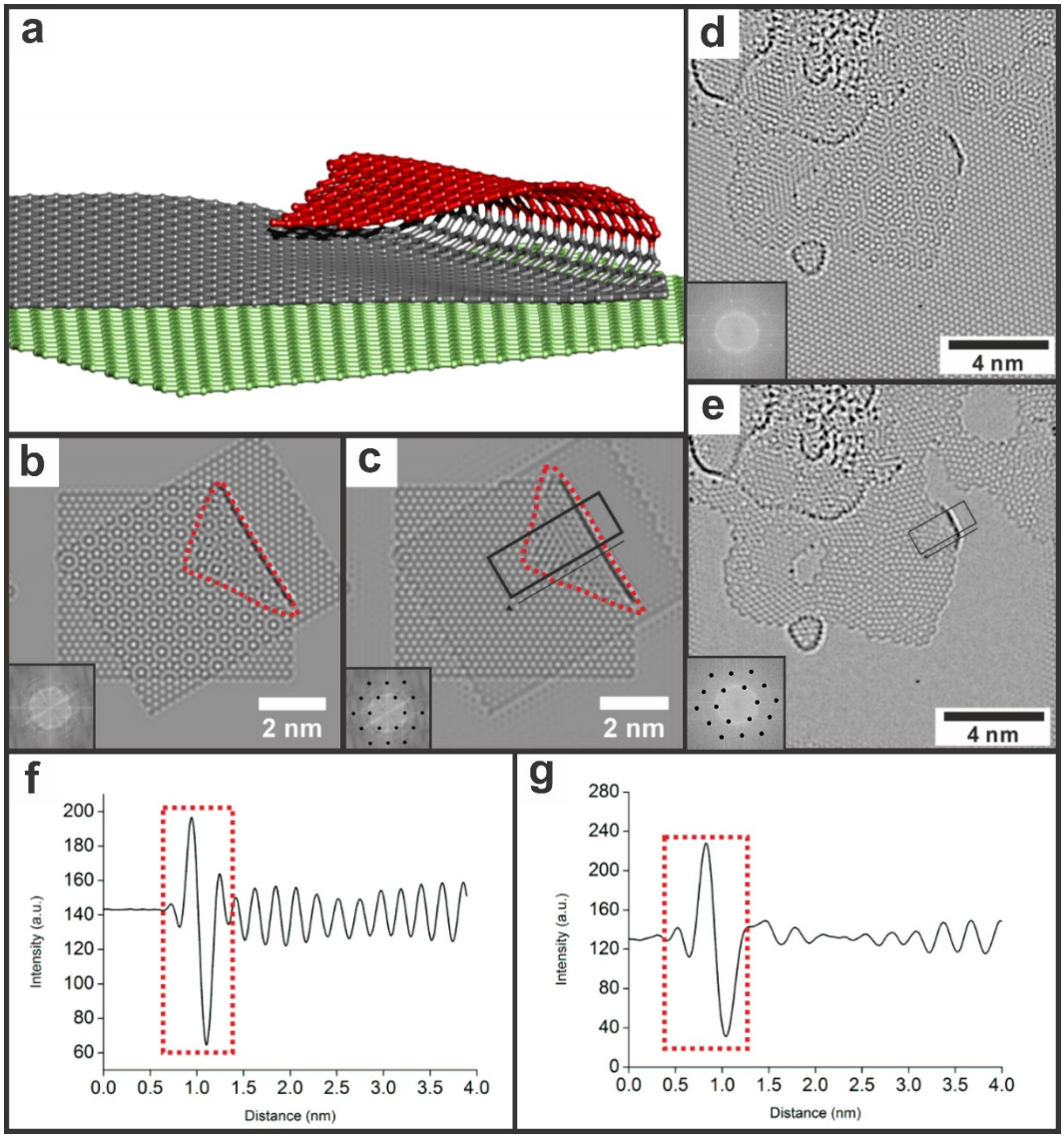

Figure 6-6. Back-folding of the secondary layer of graphene. (a) Schematic illustration of the secondary layer of graphene being folded back. (b) Multislice image simulation of the atomic model in (a) with - 2 nm defocus and 6 nm defocus spread. The inset shows the FFT of the simulated image. (c) Reconstructed images from the FFT negative mask, shown in the respective inset. (d) An AC-TEM image of bilayer graphene with folded edge. (e) Reconstructed image from the FFT negative mask in the respective inset. (f,h) Intensity profiles taken from the boxed regions in (c) and (e) along the direction indicated by the arrows.

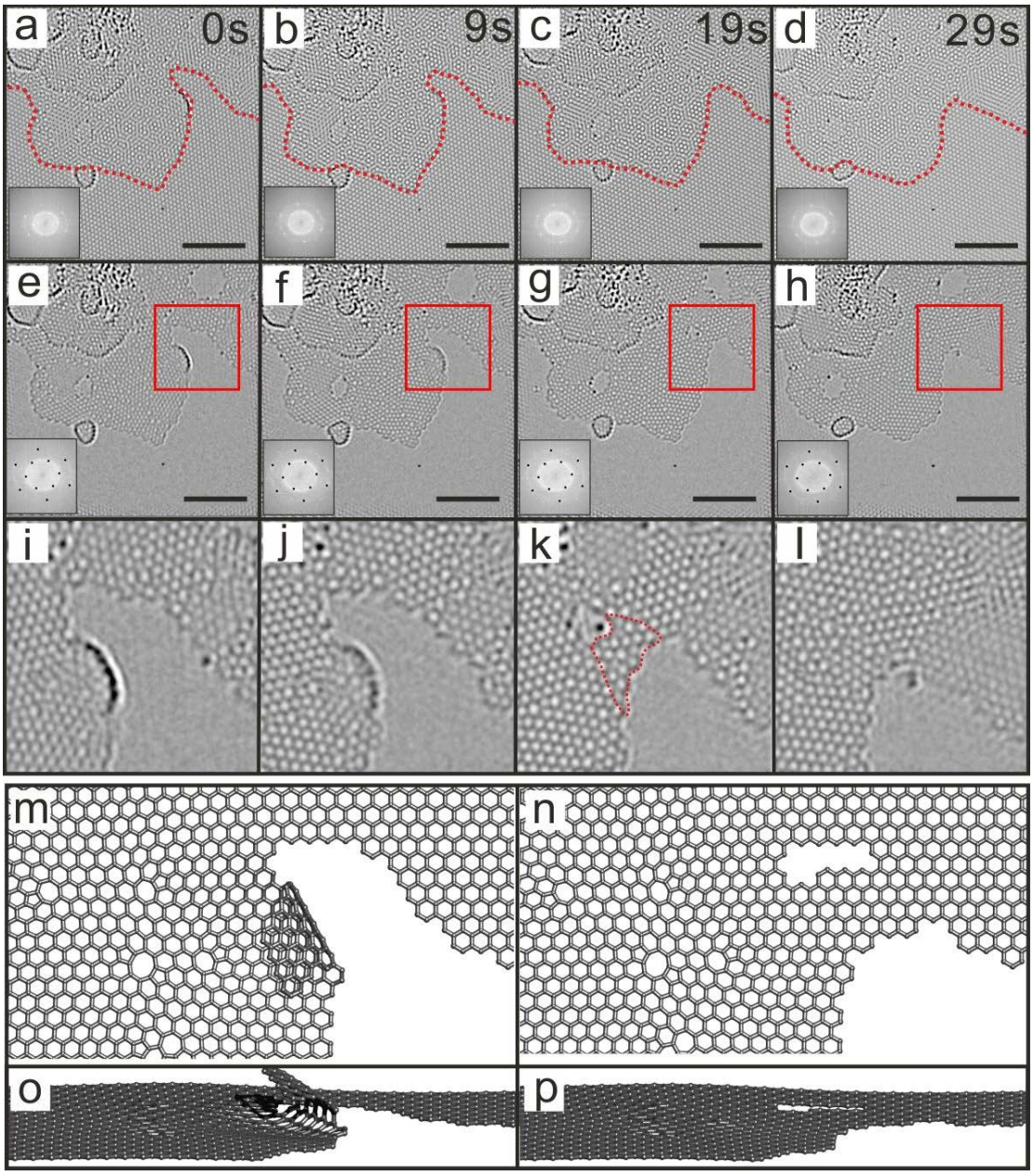

Figure 6-7. Dynamics of an unfolding graphene layer at 800 °C. (a–d) Time series of AC-TEM images showing a secondary layer of graphene initially grown at 600 °C and then examined at 800 °C. The FFTs are shown in the respective insets. (e–h) Reconstructed images from the FFT negative mask shown in the respective insets. (i–l) Magnified AC-TEM images taken from the red boxed regions in (e–h) to highlight the unfolding dynamics. (m–p) Front and side views of the atomic models before and after unfolding. All scale bars = 4 nm.

During the growth process, the increased contrast at the growth front due to back-folding compared to other edge regions is repeatedly observed, as shown in Figure 6-5m–o with the white dashed area. The temperature is than increased from 600 °C to 800 °C to slow down the growth rate so that the atomic configuration of the edges and the crystallization from amorphous to sp^2 could be investigated. Figure 6-6a is the side view of an atomic model of a back-folded secondary layer of graphene, with corresponding multislice image simulations shown in Figure 6-6b. A red dashed line in Figure 6-6b indicates the back-folded region. It is apparent that the contrast along the folding pleat increases dramatically. In order to quantify this, an image is reconstructed from the fast Fourier transform (FFT) using an exclusion mask for the set of hexagonal spots associated with the underlying graphene (inset in Figure 6-6c).

A boxed line profile, Figure 6-6f, was taken from the black rectangle highlighted region along the direction shown with a black arrow in Figure 6-6c. Figure 6-6d shows an AC-TEM image of a region of secondary layer graphene, whose presence is evident from the Moiré pattern. The reconstructed image in Figure 6-6e excludes the signal from the bottom graphene layer, leaving only the secondary layer graphene for analysis. A boxed line profile figure is also taken from the black boxed region along the arrowed direction, and the result is presented in Figure 6-6g. The red dashed box highlights the region with apparent enhanced contrast, accordant with what is observed in the multislice image simulation in Figure 6-6f. As have been previously reported, the increase in contrast originates from multiple atoms under the projection of electron beam along the back-fold. [135,144] However, it is difficult to determine whether the

secondary layer of graphene is folded back or just bonded to the first graphene layer, as both introduce an increase in contrast.

Studying the dynamics of the back folded region of the secondary layer of graphene provides further insights into the structure. Figure 6-7a–d contains a time series of AC-TEM images with red dashed lines highlighting the frontier of the secondary layer and shown in the inset. Figure 6-7e–h shows reconstructed images from the negative masked FFT shown in the insets. Red rectangles highlight the areas of interest, which are magnified and shown in Figure 6-7i–l respectively. Figure 6-7i shows a dark contrast line that was previously discussed originating from back-folding or possibly bonding to the bottom layer. In this time series study, it could be observed that the darker contrast along the edge in Figure 6-7j fades away in the subsequent two frames (Figure 6-7k,l), an area of extra graphene extends out where there used to be the darker contrasted boarder over the course of just 10 s. This indicates the extra area came from the unfolding of the folded area. The red dashed line in Figure 6-7k highlights the extra region formed in the unfolding process. Figure 6-7m–p demonstrates this process with atomistic models: with Figure 6-7m showing the folded model and Figure 6-7n showing the structure after unfolding. Figures 6-7o,p shows the side views of the two models respectively. This study of the edge dynamics of the secondary layer of graphene confirms the darker contrast arises from back-folding rather than edge bonding.

6.2.4 Crystallization of a second layer of graphene

Once the graphene domains reach a certain size, crystallization begins to be a dominant structural factor. The small graphene domains are initially highly polycrystalline and then begin to improve their ordering at high temperatures, achieving a better sp^2 structure and Figure 6-8 shows this in detail for the elevated temperature of 800 °C. The data set in total consists of 72 AC-TEM images taken over 34 min 7 s. Figure 6-8a shows the same image as Figure 6a but in higher magnification in order to examine the atomic scale lattice configuration. The image is then filtered using a mask in the FFT to eliminate the underlying monolayer graphene and reconstructed (Figure 6-8b), then maximum filtered (Figure 6-8c) for better visualization of nonhexagonal rings. Yellow circles in Figure 6-8b highlight heavier atoms (probably Au) trapped in graphene and at the edge. Unlike previous reports, the newly formed graphene is neither fully crystalline nor purely amorphous. In Figure 6-8d the crystalline area in the image is shaded with color, and the nonhexagonal rings are marked by the dashed polygons. It is apparent that a large proportion of the top layer is comprised of well-crystallized graphene grains. However, the lattice orientation of each grain is randomly distributed, and the grain size is in the nanoscale, from 1 to 2 nm. There is also a large amount of pentagons and heptagons and several octagons at the boundary of the grains. The majority of the GBs can be regarded as highly aperiodic and curved 5-7 dislocation strings. This result is similar to the TEM images taken by Westenfelder *et al*. at 1000 K for graphene transformed from amorphous carbon. [154]

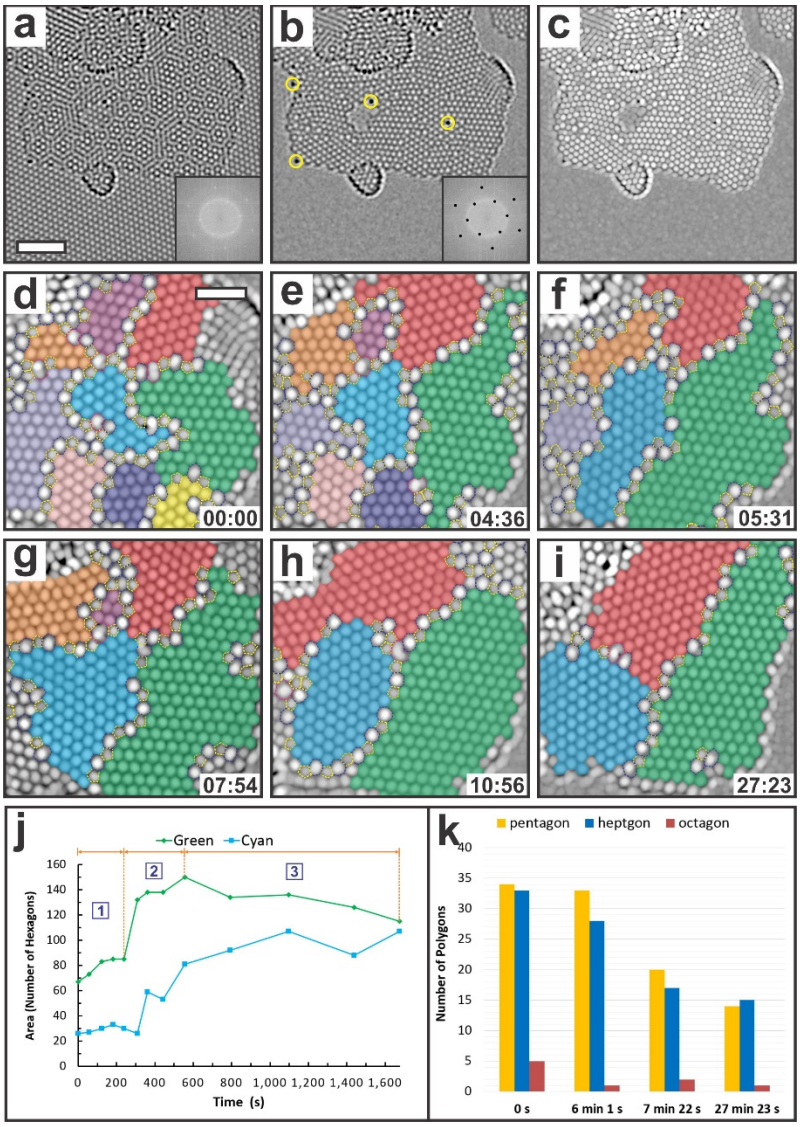

Figure 6-8. Crystallization of the as-grown graphene layer over time at 800 °C. (a–c) Image processing details: (a) Cropped from Figure 6-7a and then magnified with the inset showing its FFT; (b) reconstructed image from FFT negative mask shown in the inset showing the top graphene layer; and (c) maximum filtered image of (b). (d–i) Six time series frames showing the growth and coalescence of graphene grains, overlaid with false colors. The pentagon, heptagon, and octagon in the GBs are indicated by the dashed yellow, blue, and pink polygons, respectively. (j) Two trend lines representing the size change of the grains shade in blue and cyan as a function of time. (k) Statistics of non-hexagonal rings in the GBs. Topological defects within the grain or at the edge are not included. The scale bars in panel a and d are 2 and 1 nm, respectively.

As discussed in Chapter 5, both glide and climb motions for dislocation in graphene can be significantly accelerated at temperatures above 500 °C under 80 kV electron irradiation. Therefore, as expected, subsequent migration of GBs and crystallization of nanosized grains was observed over time. Figure 6-8d–i shows a time series of AC-TEM images of the crystallization with the images processed the same way as Figure 6-8c. A dozen graphene grains have merged into 3 larger ones with sizes of 2–5 nm in the first 11 min. Sinuous GBs with high curvature tend to reconstruct into a more symmetric and straight shape over the whole time period. The growth rates for the domains shaded in green and cyan are plotted in Figure 6-8j as the form of the number of undistorted hexagons within the domain versus time. The growth process for both grains is discontinuous. Take the grain shaded in green for example, despite the apparent shape reconfiguration of GBs in the first 4 min (Figure 6-8d and e), the grain size does not change much (Stage 1, T1). A sudden change in the grain size took place between 4 and 9 min by consuming smaller grains colored in purple and yellow (Stage 2, T2). No more grain merging is observed afterward, but the movement of GBs continues at a much slower rate, leading to the gradual shrinkage of grain size in the next 19 min (Stage 3, T3). The evolution of the cyan grain is similar. The statistics in Figure 6-8k shows that significant reduction in nonhexagonal rings occurs between 6 min 1 s and 7 min 22 s, approximately the same period when the coalescence took place.

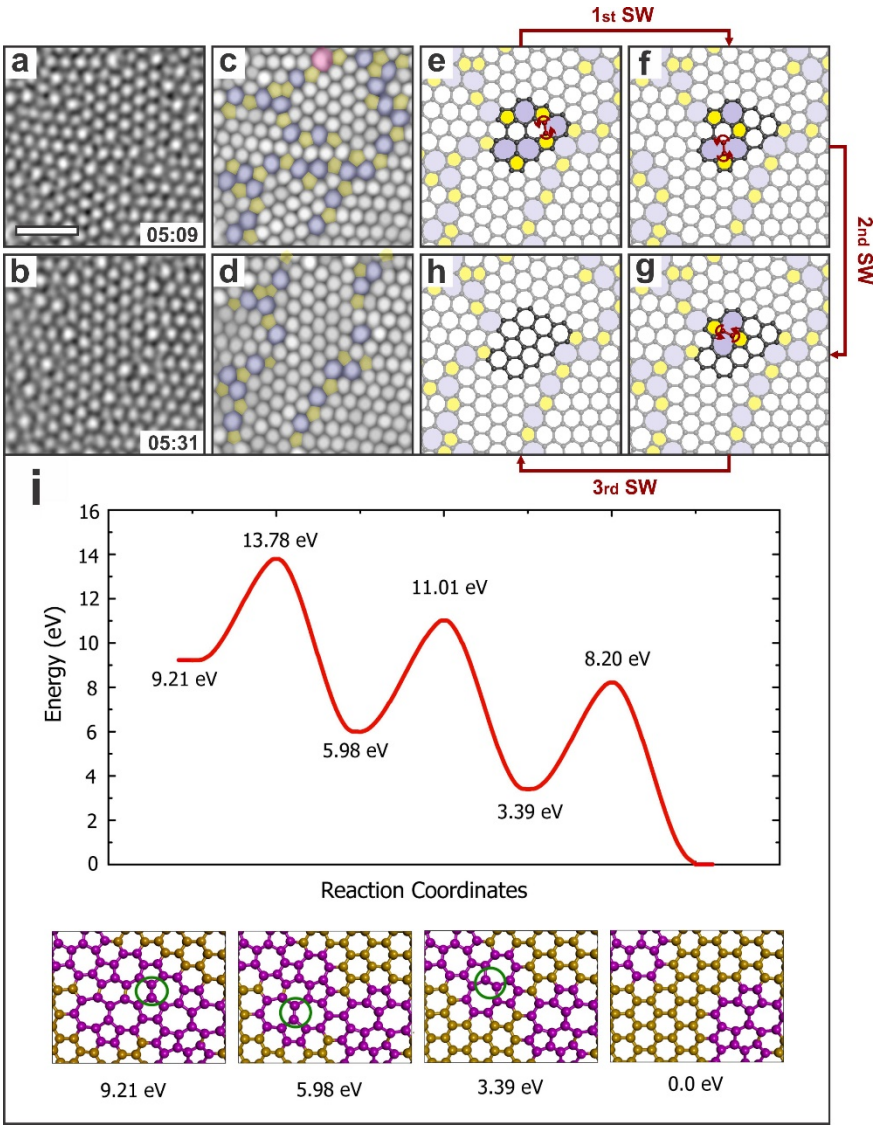

Figure 6-9. The merging of two grains *via* three bond rotations. (a,b) FFT reconstructed AC-TEM images showing the atomic structure of the second layer of graphene at 5 min 9 and 22 s later. (c,d) Maximum filtered images calculated from (a,b) with nonhexagonal rings shaded in color. (e,h) Atomic models corresponding to (a) and (b). (e–h) A probable pathway for the detailed structural change between the GBs in (a) and (b) suggested by high temperature TBMD simulations. The arrows and atoms highlighted in red indicate the bond undergoes a SW bond rotation in the next panel. The color scheme in the maximum filtered images and atomic models represents the number of carbon atoms in each ring, with 5 = yellow and 7 = blue. (i) DFT calculated energy barrier for the pathway shown in (e–h), performed by Professor Gun-Do Lee's group from Seoul National University. The scale bar in panel a is 1 nm.

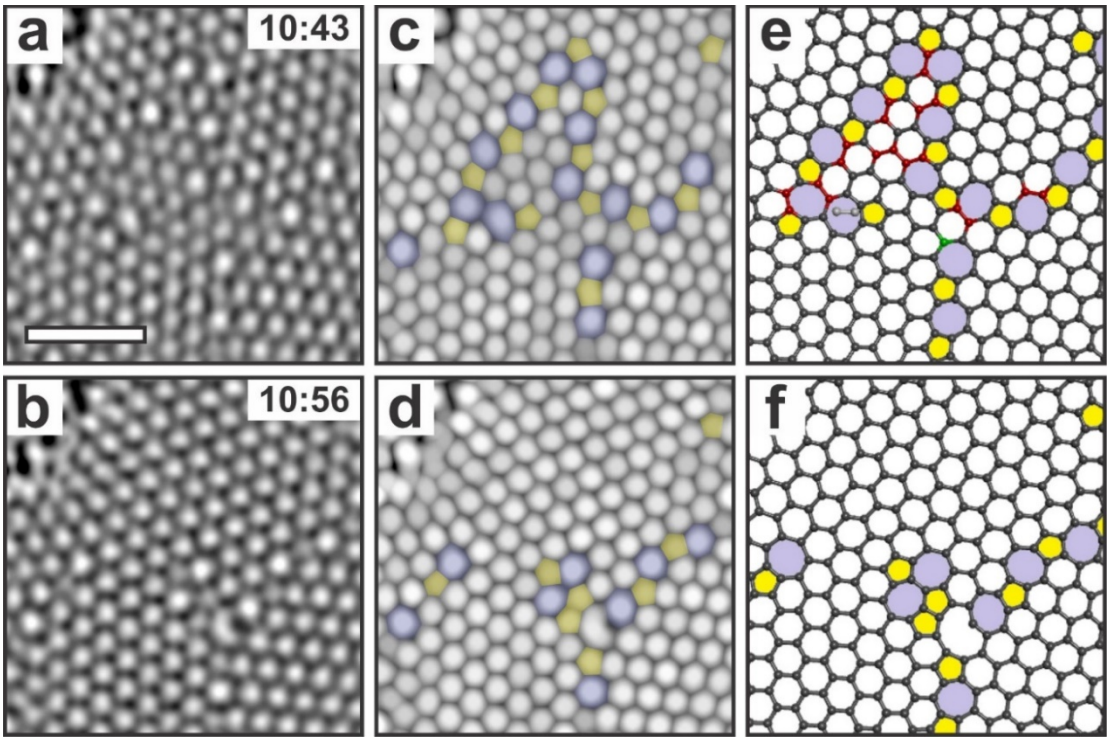

Figure 6-10. Another example showing the merging of two grains mainly through several bond rotations happen in a short span of time. (a,b) FFT reconstructed AC-TEM images. (c,d) Maximum filtered images. (e, f) Atomic models. In panel e, bonds to be rotated in next 13 s are highlighted in red; atoms to be evaporated are indicated in green. Carbon adatoms are highlighted in white. The structural change from panel a to b is accomplished by 10 bond rotations, removing carbon atom and incorporating two carbon adatoms into graphene lattice. The scale bar in panel a is 1 nm.

In Figure 6-9, the coalescence of grains colored in cyan and pink in Figure 6-8e is examined at the atomic level. The structural change between Figure 6-9a and b is accomplished by three sequential SW bond rotations within 22 s, as schematically illustrated in the atomic models shown in Figure 6-9e–h. It is found that the bond rotations are initiated at the junction of three highly curved GBs, where there is a high density of nonhexagonal rings (Figure 6-9a,c and e). It has been shown that bond rotation and atom loss are more likely to occur in the defective area under electron beam irradiation due to a lower sputtering cross section. [139] Chapter 5 shows that

such a phenomenon becomes more pronounced at elevated temperatures. In Figure 6-9i, the energy barriers for all three rotations are calculated to be 4.57, 5.03, and 4.81 eV, respectively; all significantly lower than the energy required to form a SW defect (9–10 eV) or dislocation glide (6.95 eV). [76,96,228] The energy for each bond rotation to reverse back is more than 3 eV higher. This explains why the GBs unwound so rapidly in T2, and that the temporal resolution of imaging in this thesis was insufficient to capture any intermediate structure. As a consequence of the structural reconfiguration in Figure 6-9a–h, the total energy of the second layer of graphene is decreased by 9.21 eV with the curvature of GBs greatly reduced, as shown in Figure 6-9b,d and h, which is in agreement with previous research indicating that the driving force for GB migration energetically favors decreasing GB length and curvature. [152] Another similar example is given in Figure 6-10 where 10 bonds rotate in a time span of 13 s leading to the incorporation of a small graphene grain into a larger one.

Figure 6-11 shows how dislocation movement can play an important role in grain merging at the edge regions. The grains to be merged are the ones shaded in blue and green in Figure 6-8d. A carbon dimer was removed from the GB after 16 s, resulting in the 5-8-5-5-7 defect at the boundary, reconfiguring into a 5-7 edge dislocation and the 5^{o} angle mismatch in Figure 6-11a partly compensated (Figure 6-11b). The GB totally annihilates after another 17 s (Figure 6-11c). The individual steps for this transformation were not resolvable in current imaging conditions. Figure 6-11h–k shows a plausible pathway by forming an isolated dislocation core at the first instance (Figure 6-11i). The dislocation then disappears by gliding toward the edge along its

glide plane (indicated by the red arrow in Figure 6-11i) making the lattice mismatch eventually compensated.

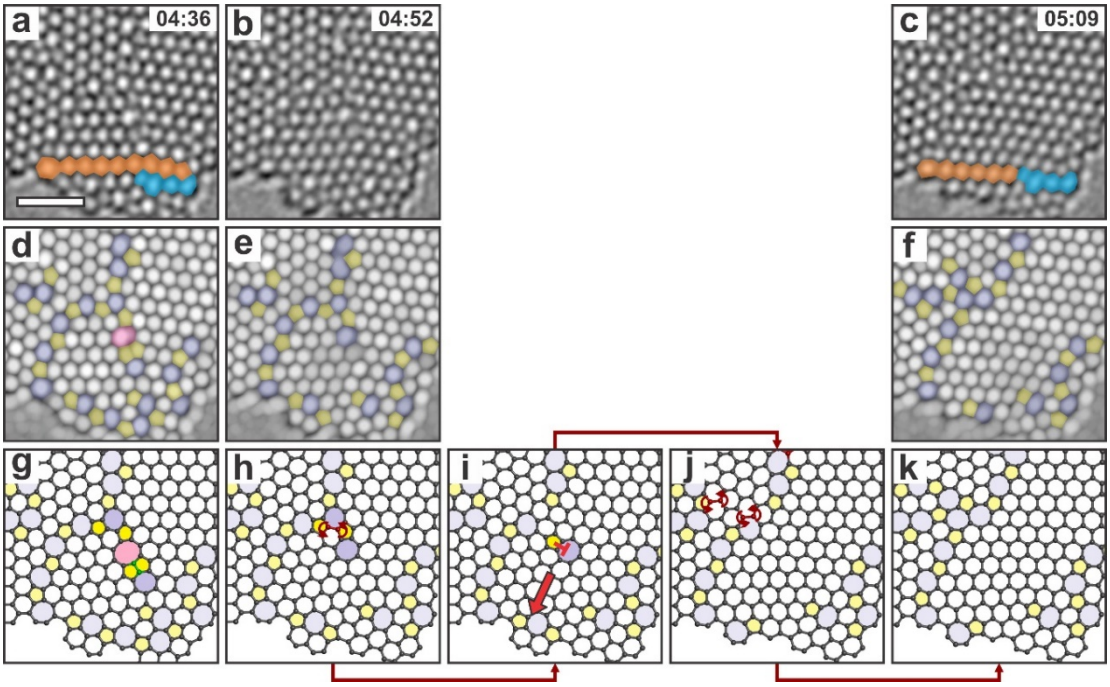

Figure 6-11. The coalescence of two grains *via* the slip of an edge dislocation toward the edge. (a) FFT reconstructed image of the second-layer graphene at 4 min 36 s, which loses a carbon dimer at GB in the next frame, shown in (b). (c) A following image showing annihilation of GB and merging of two grains at graphene edge. (d–f) Maximum filtered images of (a–c). (g,h,k) Atomic models of (a–c). (h–k) A possible path for the structural reconfiguration between panels b and c. A SW rotation first transforms the GB into an isolated pentagon–heptagon configured dislocation (i), which subsequently disappears by gliding to the edge. Bonds that undergo a SW rotation in the next frame are highlighted in red and by arrows. Atoms to be sputtered are highlighted in green. The color scheme in the maximum filtered images and atomic models represents the number of carbon atoms in each ring, with 5 = yellow, 7 = blue, and 8 = pink. The scale bar in panel a is 1 nm.

In Chapter 5, the interactions between dislocations and graphene edges are investigated and it is demonstrated to be energetically favorable for a dislocation to glide toward the edge of graphene, provided the distance is close enough. [193] The structural change between Figure 6-11j and k was accomplished by two further bond rotations.

Evidence to support this is highlighted in Figure 6-11a and c. Two rows of zigzag-oriented graphene lattice are colored in cyan and orange in Figure 6-11a for visual reference. They change into one zigzag row in Figure 6-11c which can only result from the slip behavior of an edge dislocation.

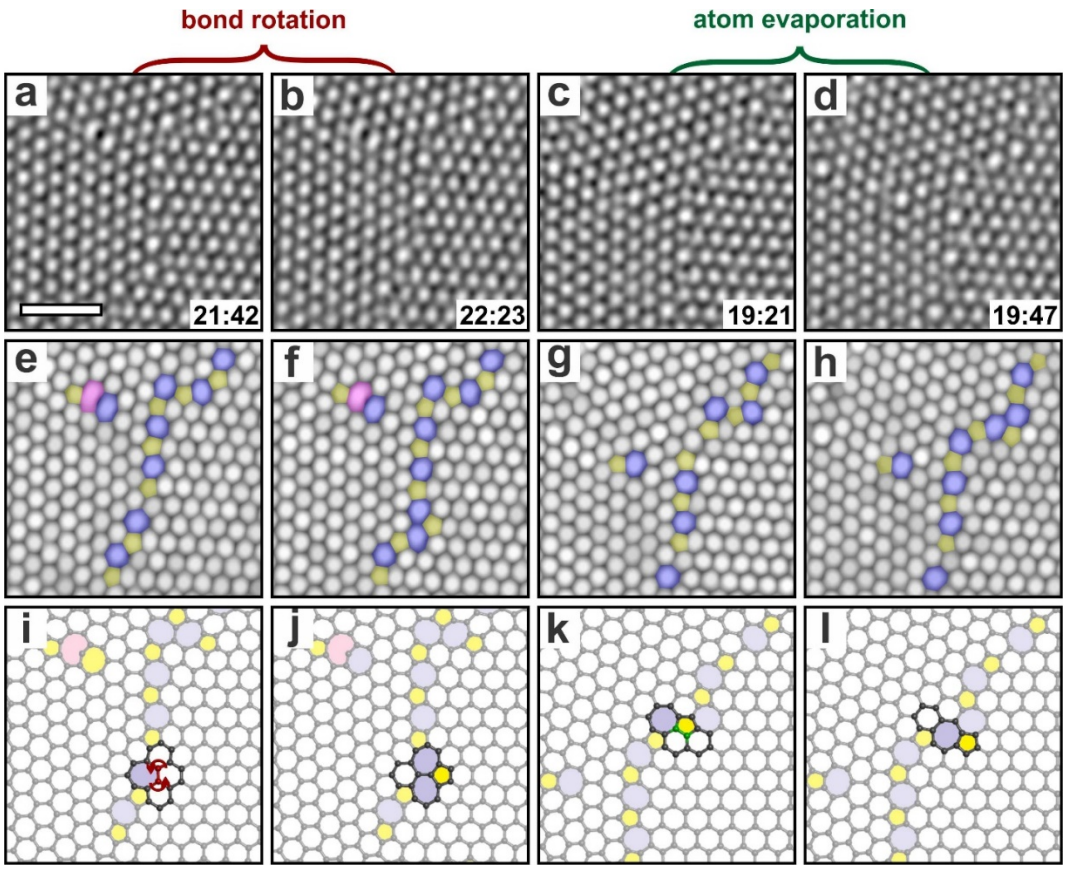

Figure 6-12. Bond rotation and dimer evaporation within the GB. (a, b) AC-TEM images showing a single bond rotation. (c, d) AC-TEM images of GB migration by sputtering a carbon dimer. (e–h) Maximum filtered images. (i–l) Atomic models. The scale bar in panel a is 1 nm.

After the first 11 min, the original nanosized grains merged to form three larger ones (colored in cyan, red, and green in Figure 6-8h). Instead of combining into an even larger grain, only occasional bond rotation and atom loss occurred in or near the GBs over the next 17 min (Figure 6-12), similar to the basic glide and climb step of a 5-7 dislocation core. [56] The relatively slow migration rate enables tracing the structural

change of the second layer atom by atom between each frame. In Figure 6-13, it is observed that the intermediate structure before a carbon dimer was completely sputtered from GB. The defect structure in Figure 6-13a remained stable for 35 s, before a carbon atom acquired enough energy in an electron collision to break two sp^2 bonds and rotate perpendicular to the graphene plane (Figure 6-13b). The magnified view and its corresponding multislice simulated TEM image on top of Figure 6-13b show that the vertically stacked carbon dimer has a higher intensity than other carbon atoms. The dimer was at last removed out of the graphene plane in another 32 s. Figure 6-14 shows a comparison between the energy barriers of two mechanisms to evaporate a carbon dimer. The flipping of the dimer first needs to overcome a barrier of 9.26 eV. The vertically stacked structure is surprising stable with the energy only 2.41 eV higher than ground state suggested by DFT calculation. The energy barriers to further evaporate the vertically stacked dimer are 2.75 and 2.2 eV respectively. Theoretically the two atoms may also be sputtered one after another but the energy required for this process is far higher (12.7 eV).

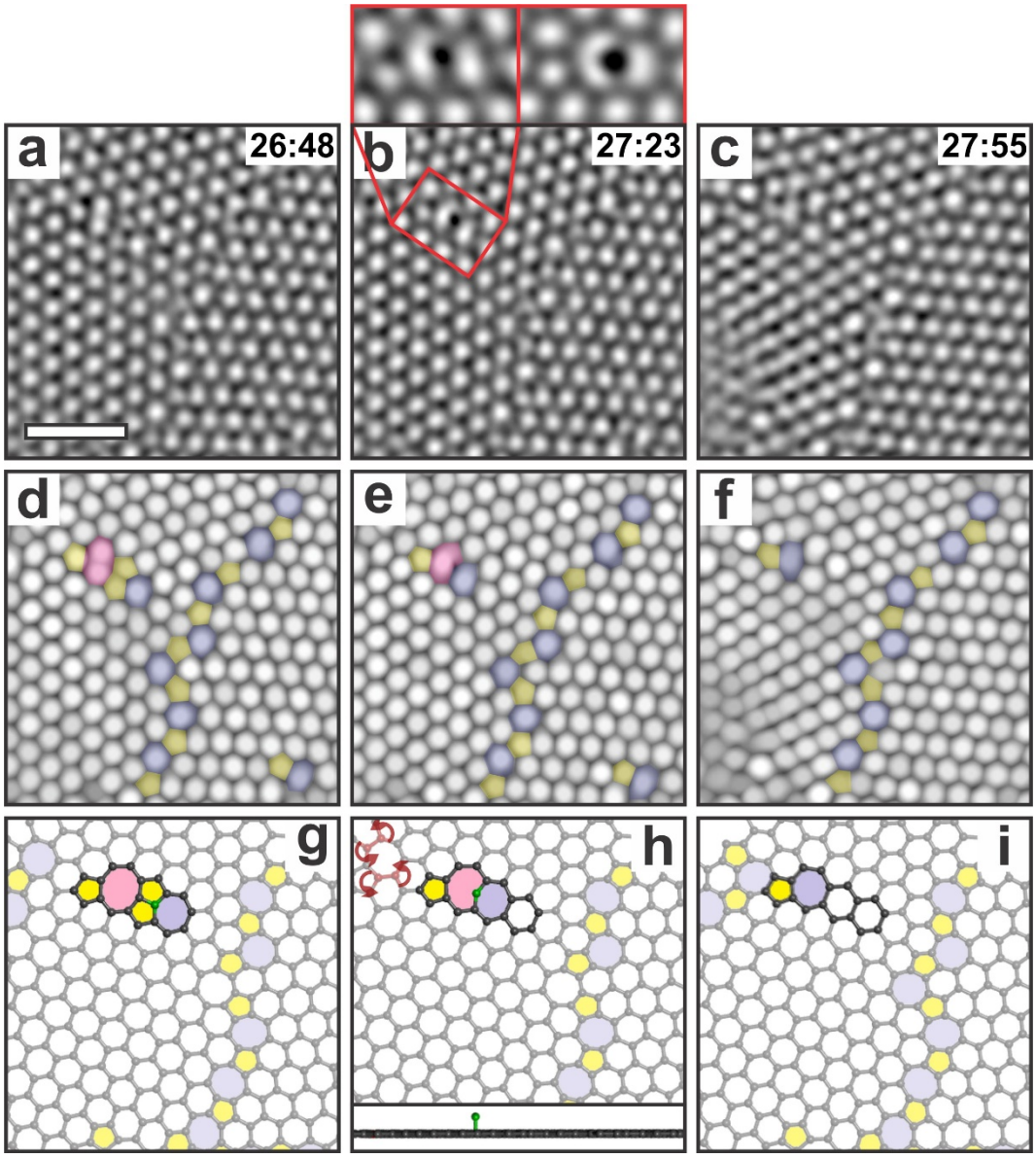

Figure 6-13. Evaporation of a carbon dimer in the GB. (a) FFT reconstructed AC-TEM images of the second-layer graphene at 26 min 48 s. (b) After 35 s, a carbon dimer in the GB is rotated perpendicular to the graphene plane. Magnified view of the flipping dimer is presented on top, along with the multislice simulated TEM image with - 2 nm defocus and 6 nm defocus spread, based on the atomic model in (g). (c) The dimer is eventually removed after another 22 s. (d–f) Maximum filtered images of (d–f). (g–i) Corresponding atomic models. The inset in (h) shows its side view. The scale bar in panel a is 1 nm.

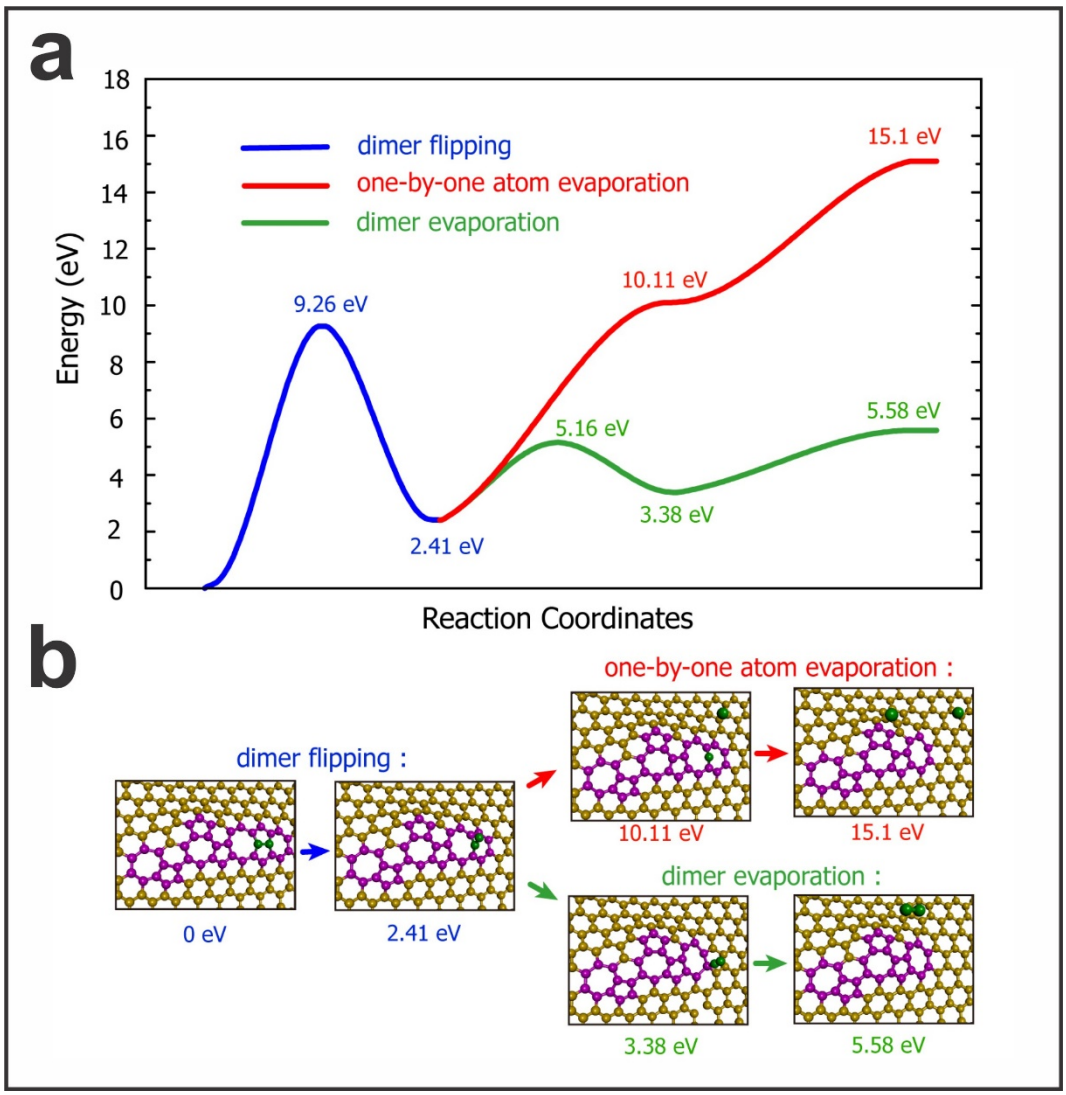

Figure 6-14. DFT calculated energy barriers of two mechanisms for the evaporation of a carbon dimer. (a) Energy curves for the dimer evaporation. In both pathways, the carbon dimer needs to first overcome a 9.26 eV barrier and get vertically stacked (blue curve). The energy barriers to subsequently sputter the dimer as a whole are 2.75 and 2.2 eV, respectively (green curve). The two carbon atoms may also be removed one after another which requires a total energy of 12.69 eV (red curve). (b) Atomic models and DFT calculated relative energies for the moments of dimer evaporation. The simulation results are provided by Professor Gun-Do Lee's group from Seoul National University.

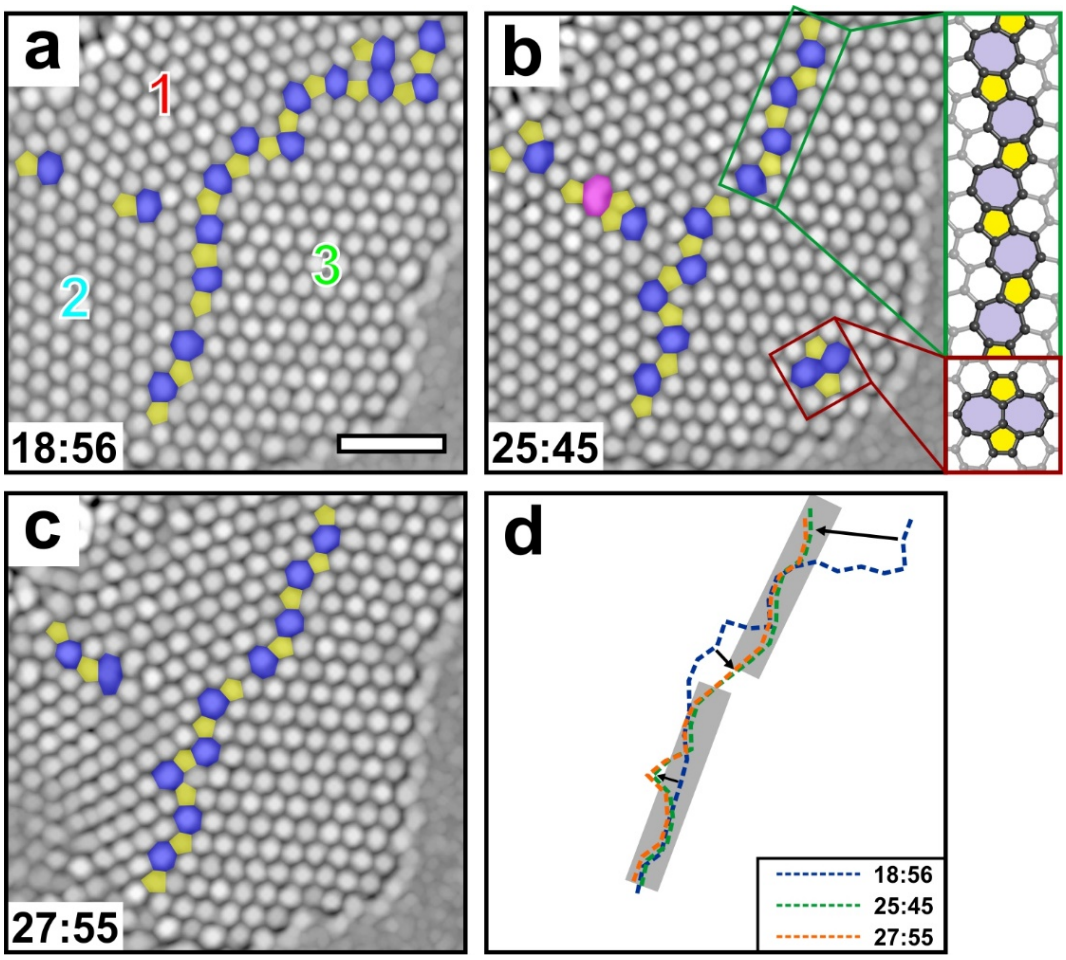

Figure 6-15. The stability of GBs. (a) Maximum filtered TEM images of the second-layer graphene at 18 min 56 s. (b) The same area imaged after 6 min 49 s, with atomic models of the GB between grain 1 and 3, and SW defect near the edge shown in the insets. (c) The same area imaged 2 min 10 s after (b). (d) Dashed lines showing the evolution of the high mismatch angle GB, which are drawn by connecting the central point of adjacent pentagons and heptagons at the boundary. The gray rectangles indicate the symmetric lines between grains. The migration direction of the GB is indicated by black arrows. The scale bar in panel a is 1 nm.

Here, the reason why the coalescence of grains is drastically reduced after 11 min is discussed. When the grain reaches a certain size, the GBs progressively evolve into a less meandering structure. As a consequence, there is no defect or edge nearby for the GB to interact with. The maximum energy an electron can impart to a carbon atom is ~ 19 eV in (80 kV accelerating voltage, 800 °C), which is not sufficient for a dislocation

to make a long distance motion. [228] Although a bond rotation could still be activated at the GB under 80 kV electron irradiation, it is not energetically favorable since the GB has evolved to a relatively straight and symmetric shape (green inset in Figure 6-15b). The rotated bond is more likely to quickly restore in another electron collision. In addition, it is discovered that the stability of GBs is dependent on the misorientation angles. Figure 6-15 shows images of a second-layer graphene taken after 18 min 56 s. The lattice orientations for the grains 1, 2, and 3 are 0°, 9°, and 38°. The GB between grains 1 and 2 is a low-tilted angle GB made of dislocations pointing to the same direction. The other two with 27° and 38° misorientation angles are high-angle tilt GBs. In total 9 bond rotations and 4 atoms lost were observed in or near the low-angle tilt boundary between grain 1 and 2 from 18 min 56 s to 27 min 55 s, while 8 bond rotations and only one dimer sputtering (shown in Figure 6-12) occurred in the high-angle GB. Considering the lengths of the GBs, it is apparent that the high-angle one possesses higher stability in the imaging condition of this thesis. This is consistent with the theory proposed by Liu *et al*. [229] As the dislocation density increases with the gain mismatch angle, the strain introduced by the dislocations partially cancels each other and the out-of-plane distortion caused by the GBs becomes smaller, which has been proven to be robust under electron irradiation. [139] It is worth noting that the top right part of the high-angle GB (Figure 6-15a) rotates from the edge to the symmetric line between two grains (gray rectangle in Figure 6-15d) in the first 6 min 49 s (migration direction shown in Figure 6-15d), which further straightens the GB. Once it configured into a linear and symmetric shape in Figure 6-15b, no structural change took place in the next 2 min 10 s. The SW defect (red inset in Figure 6-15b) appeared 4 times at the

edge of grain 3 during the same period, which has been experimentally confirmed to help alleviate the strain induced by the high-angle GB in Chapter 4 and enhance its stability.

6.3 Conclusion

This chapter investigates the *in situ* high-temperature growth of secondary layers of graphene using Au nanoparticles as seeds for heterogeneous nucleation within an AC-TEM. It is found that graphene starts to encapsulate the Au nanoparticle at temperatures above 300 °C and continues to grow the area under electron irradiation. 600 °C is the optimum temperature to grow a second layer of graphene within the *in situ* environment. The TEM chamber pressure is kept at ~ 10^{-5} Pa to maintain the TEM in a workable condition. An Au particle on clean and defect-free graphene was particularly chosen for the growth experiment, as the contamination coming from the graphene synthesis and transfer process may significantly increase the local hydrocarbon gas pressure and directly lead to the formation of amorphous carbon. The mechanism for growth front propagation is found to be an alternate process of carbon cluster deposition and indentation filling. A detailed study of the edge reveals that the occasionally observed dark contrasted lines arise from back-folding of the second layer. Further increasing the temperature to 800 °C slows down growth but accelerates the crystallization of as-grown graphene. The secondary layer starts as highly polycrystalline, but improves its ordering under the combined effect of beam irradiation and increased thermal energy. Large grains grow at the expense of smaller ones *via* multiple bond rotations occurring almost simultaneously. The coalescence of grains near the edge further involves the

interaction between GB and edge. The merging of grains stopped when the grain reached a certain size. Afterward the GB migration is dominated by single glide and climb motions of dislocations. This sheds light on how nanoparticle impurities on the surface of graphene could seed multilayer regions during CVD growth of graphene.

Chapter 7

In Situ High Temperature Atomic Level Studies of Large Closed Grain Boundary Loops in Graphene

7.1 Introduction

Defects in graphene have a great impact on its exceptional electronic, mechanical and chemical properties. [1,5,9,230,231] Compared with other defects, grain boundaries (GBs) have attracted much more attention recently since their presence is inevitable in polycrystalline graphene synthesized by chemical vapor deposition (CVD). The atomic structure of GBs in graphene has been revealed by multiple TEM and STM studies, which is, in most cases, a chain of adjacent pentagon-heptagon dislocation cores. [129,151–153,216] Lahiri *et al*. has also found 5-8-5 configured linear GB in graphene, the formation of which is due to the strong interaction with Ni (111) substrate. [109] Most often GBs in graphene are classified as symmetric and asymmetric. GBs in CVD synthesized graphene are often highly asymmetric and meandering, which could reconstruct into periodic and symmetric forms after thermal annealing or electron irradiation. [154,228] Theoretic calculations have shown that the symmetric GB in graphene increases its mechanical strength and introduces magnetism. [124,156,232] Yazyev *et al*. have reported the presence of a well-defined transport gap across a particular asymmetric graphene GB. [163] These studies suggest that the GB is a

promising candidate for graphene defect nanoengineering and nanoscale device fabrication.

However, there is also a third type of GB where the pentagon-heptagon pairs are end-to-end connected, generating a loop with inner honeycomb lattice rotated, known as the closed GB loop. To date very few research efforts have been devoted to investigating such defect in either theory or experiment. Kurasch *et al*. have observed GB loops with 1–2 nm diameters and have shown that their structural change is mediated by bond rotations with both real-time TEM observation and Monte Carlo simulation. [152] The presence of such defect in graphene is also predicted to decrease the thermal conductivity of the material. [233] However, the formation dynamics of the GB loop still remains mysterious. Its stability and detailed structural evolution also need to be confirmed by further experiment.

In this Chapter the atom-by-atom transformations associated with large closed loop GB defects is examined using high temperature *in situ* AC-TEM. Monolayer graphene was synthesized by ambient pressure CVD method on a melted copper substrate as described in Chapter 3. The sample was then transferred onto a heating chip designed for *in situ* temperature controlled TEM experiments up to 900 °C. AC-TEM imaging was performed at an accelerating voltage of 80 kV utilizing an image corrector, which allows Ångstrom resolution imaging of the topological defects in graphene.

7.2 Results and Discussion

7.2.1 Formation of GB loop

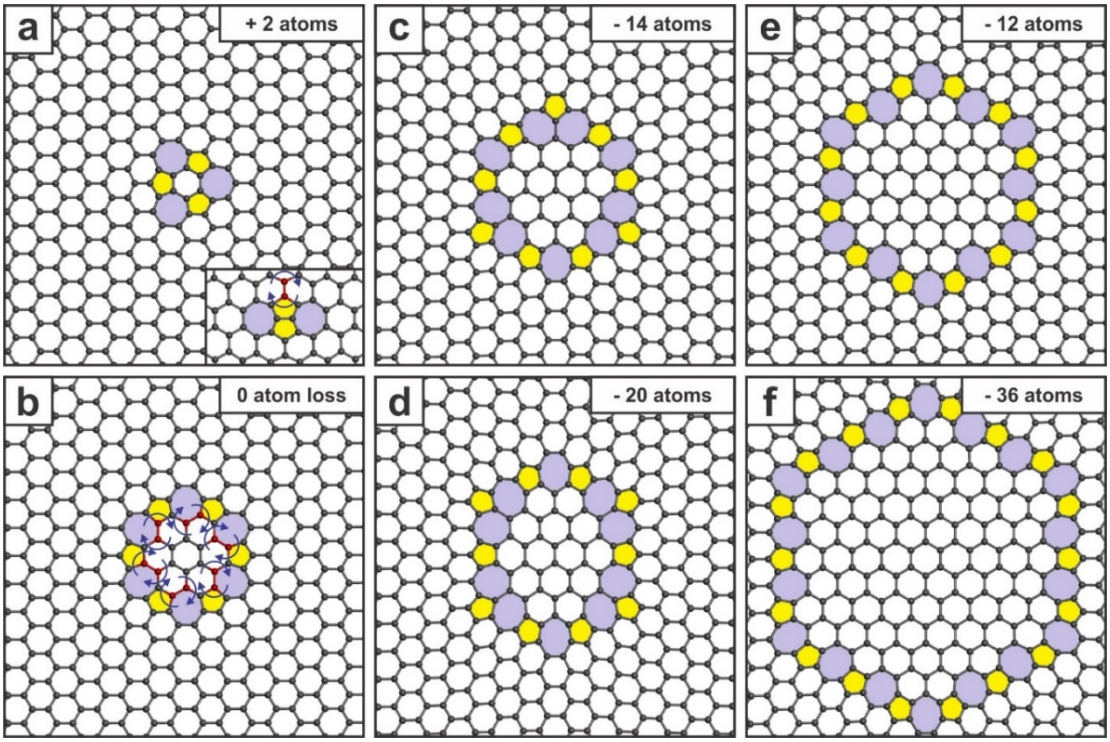

Figure 7-1. Atomic models of multiple closed GB loop defects with different sizes and symmetries. (a) A blister defect with 2 additional carbon atoms incorporated into the graphene lattice. (b) The most commonly observed closed GB defect containing a seven-hexagon core rotated by 30° . (c) Three-fold symmetric closed GB loop defect with 14 atoms lost. (d) Two-fold symmetric closed GB loop with 20 atoms removed from the lattice. (e,f) Two six-fold symmetric closed GB with 10 and 36 carbon atoms lost, respectively.

Figure 7-1 illustrates several different closed GB loop defects constructed of adjacent 5-7 dislocations, with the number of additional or subtractive atoms required in their formation processes. Figure 7-1a is the smallest carbon excess-atom defect with two additional atoms incorporated into the graphene lattice. The three-fold symmetric defect contains one hexagon in the core rotated by 30° with respect to the bulk lattice, surrounded by a triad of 5-7 edge dislocations. [116] This defect can be transformed

from an inverse Stone-Wales defect *via* a single bond rotation, as shown in the inset in Figure 7-1a. [120] Previous research has shown that excess-atom defects are energetically unfavorable under electron irradiation and the additional atoms easily get sputtered. [116] The flower-like defect containing a seven-hexagon core in Figure 7-1b has been reported in a large number of HR-TEM studies, which can be relaxed by 6 SW bond rotations. [73,152,154] It has been proposed to have relatively good stability with a low formation energy of 7.0 eV (obtained from DFT calculations) while the activation energy for a SW rotation in pristine graphene is 9 – 10 eV. [76,96] However, it becomes difficult for the graphene lattice to stay zero density deficit when creating GB loops with larger sizes. In Figure 7-1c–e, 3–fold, 2–fold and 6–fold symmetric GB loops containing 12, 14 and 31 rotated hexagons respectively are identified. The formation of each defect involves the removal 10–20 carbon atoms from pristine graphene lattice. In addition, with the increase in the loop perimeter more subtractive atoms are also required, as shown in Figure 7-1e and f.

Experimentally, large closed GB loops were occasionally found within the graphene lattice after heating to high temperature. Focused electron beam irradiation of pristine graphene areas at elevated temperatures of 500 °C is also used to artificially create large closed GB loops in graphene to study. This is based on similar methods to create defects in graphene at room temperature and partial dislocations at high temperatures of 800 °C. [73,234] AC-TEM images of two different closed GB loop structures are shown in Figure 7-2. The GB loop in Figure 7-2a contains 34 rotated hexagons within the defect, which is significantly larger than prior reports. Compared with the models

presented in Figure 7-1, the experimentally observed GB loops in Figure 7-2 are less symmetric and regular in shape, and are often accompanied with other point defects.

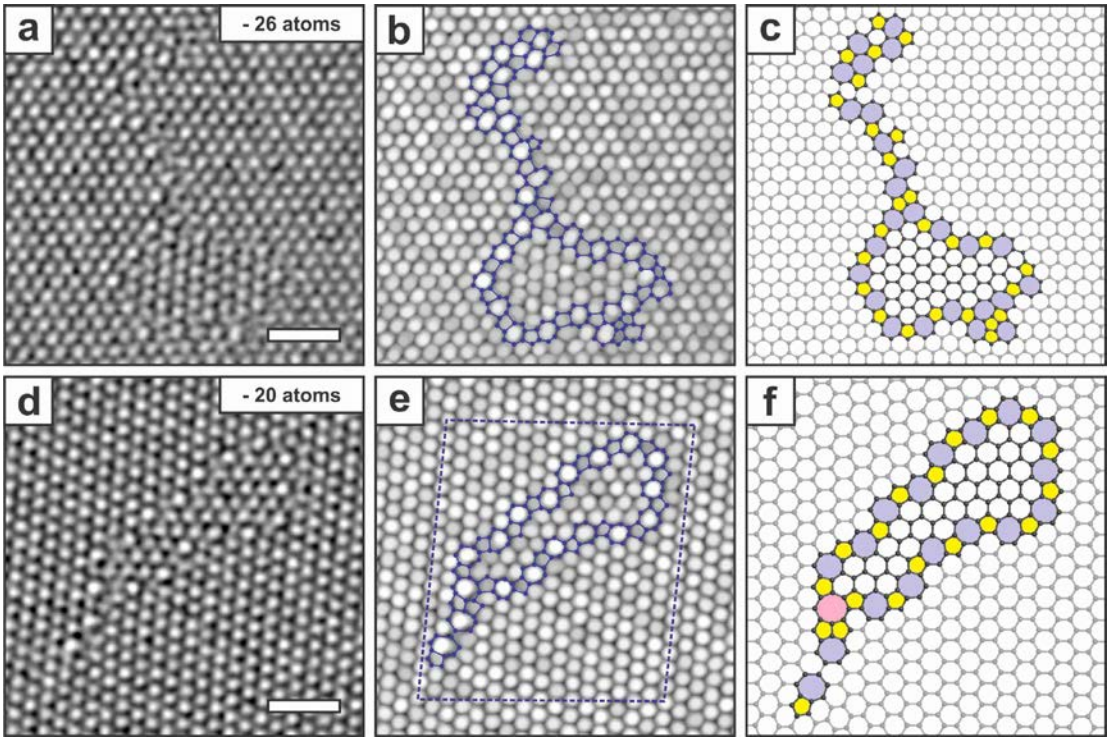

Figure 7-2. Two closed GB loops observed in monolayer graphene. (a,d) Gaussian filtered AC-TEM images of two closed grain boundary loops, the formation of which requires the removal of 26 and 20 atoms respectively. (b,e) Maximum filtered images calculated from (a,d) with non-hexagonal rings highlighted in blue. The Burger's circuit around the defect in panel e is marked by a dashed parallelogram. (c,f) Accompanying atomic models of (a,d) with the color scheme indicating the number of carbon atoms in each ring: 5 = yellow, 7 = blue and 8 = pink. Scale bars in panel a and d are 1 nm.

In rare cases, octagonal rings and distorted hexagonal rings are also found within the boundary loop. In Figure 7-2b and e, a closed circuit is drawn around the defect to measure their Burger's vectors, which represent the magnitude and direction of dislocation-induced lattice deformation. The Burger's vectors for both GB loops are found to be 0, indicating there is no unpaired dislocation inside the defect, which makes it possible for me to determine that 26 and 20 atoms are sputtered in the formation

processes of the GB loops in Figure 7-2. The detailed mechanisms of how this kind of defect is produced are not yet fully uncovered by experimental observations. The GB loop in Figure 7-2a is found in graphene at 500 °C without any focused electron beam irradiation and is likely to be an intrinsic defect coming from the CVD growth process or from the high temperature heating process. At room temperature, the defects act as anchors for the surface carbon contamination and this prevents their identification by AC-TEM. However, heating the sample to elevated temperatures above 500 °C, typically mobilizes the contamination and eventually causes it to evaporate off the surface of graphene and leave the clean lattice structure beneath for AC-TEM imaging. The defect in Figure 7-2b is created by exposing the pristine graphene to the focused electron beam for 1 min at 500 °C. At room temperature, defect structures with more than 20 atoms loss resulted from prolonged focused beam exposure typically lead to nano-sized pores. The carbon atoms at the edge are under-coordinated and have a tendency to reconstruct into saturated vacancy structures. Previous research has suggested that the displacement cross section for carbon atoms in graphene increases with temperature. It is particularly apparent in the defective area when temperature is above 500 °C. Therefore, a higher frequency of structural changes driven by bond rotations or atom evaporation is expected at elevated temperatures (≥500 °C). [228] Figure 7-3 reveals a possibility of how large GB loops can be formed using a focused electron beam at elevated temperatures. The beam is first focused within a 10-nm diameter spot to significantly increase the beam current density. The exposure time can be varied for the purpose to create different types of defects. After that the beam is expanded back to image the graphene lattice. Figure 7-3a shows an example where a

sub-nanopore and a multivacancy were initially generated by the sputtering damage at 800 °C. The increased thermal energy together with beam irradiation enable rapid reconfiguration of the defect into a structure with lower formation energy. [228] As shown in Figure 7-3, the multivacancy connected to the sub-nanopore after 4 min 35 s (Figure 7-3b) and then filled the pore after another 6 mins, yielding a GB loop defect with almost all carbon atoms saturated (Figure 7-3c). This helps explains why the closed GB loop with size shown in Figure 7-2 is more likely to be observed at temperatures above 500 °C, as the defects at room temperature lack the sustainable energy supply to restructure.

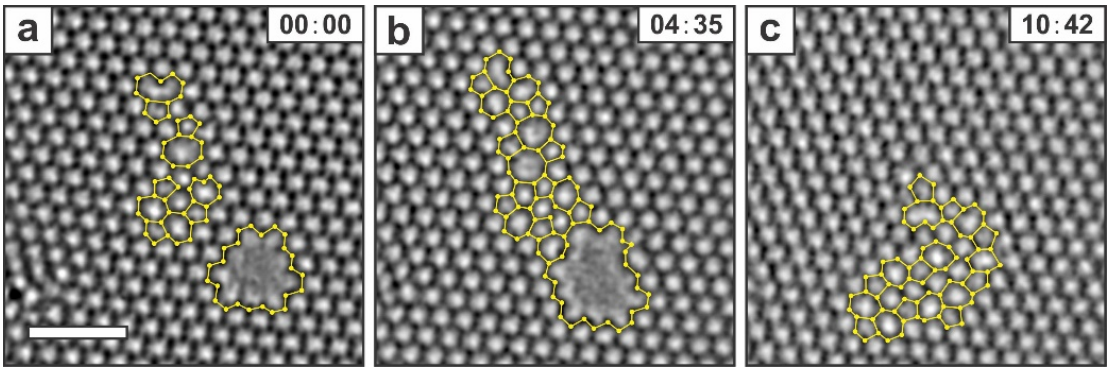

Figure 7-3. Time series of AC-TEM images showing the coalescence of a multivacancy and a sub-nanometer pore in monolayer graphene. (a) A multivacancy and a sub-nanometer pore are created by sputtering damage under electron irradiation. (b) Two defects get attached. (c) The vacancy and the pore get further merged, yielding a GB loop containing 6 hexagons. Non-hexagonal rings and dangling bonds are marked by yellow balls and sticks in all panels. The scale bar in panel a is 1 nm.

7.2.2 Evolution of GB at 500 °C

The image sequence in Figure 7-4 shows the structural evolution of the GB loop, initially shown in Figure 7-2d, from creation to annihilation. The rate of structural change is significantly accelerated at 500 °C, which facilitates this research. [228] The

data set in total consists of 130 frames recorded over 28 min 8 s. The acquisition interval between two consecutive frames is ~ 10–15 s. The GB loop was changing frequently throughout the transformation process. Structural reconfiguration was typically observed between two consecutive images, as seen from the time line chart of loop size in Figure 7-4q. The GB loop was relatively stable between 2 min 4 s and 7 min 42 s, as indicated by the larger blue ellipse in Figure 7-4q. This is probably due to the presence of the partial-dislocation like "tail" (Figure 7-2b). Previous research has shown that partial-dislocations incur less out-of-plane distortions than perfect dislocations. [234] Thus, the "tail" in Figure 7-2b may help to accommodate the rippling introduced by the GB loop and reduce the displacement threshold for atoms within the defect. At around 8 min, the defect split into two separate loops as shown in Figure 7-4c. Images showing their subsequent structural evolution are presented in Figure 7-4d–j and Figure 7-4k–p respectively. The loop at the bottom left in Figure 7-4c first evolved into an extend line defect made up of a string of non-hexagonal rings, as shown in Figure 7-4k. The line defect then got gradually unwound in the next 8 min and reconstructed into a 5-7 dislocation at 18 min 4 s, which then rapidly moved out of the imaging area within 12 s (Figure 7-4p). The loop at the top right of Figure 7-3c, however, maintained the closed loop configuration for quite some time. It first continued to grow larger and attained the maximum size at around 19 min. Thereafter, the defect started to shrink until it reached a "double-flower" configuration as shown in Figure 7-4h. The double flower defect is the assembly of two flower defects illustrated by the model in Figure 7-1b which was robust under beam irradiation. After being stable for 2 min ± 13 s, it was observed to unwind into a single flower defect *via*

6 bond rotations (Figure 7-4i). Soon afterwards the single flower defect also quenches *via* bond rotations.

The result in Figure 7-4 may give the impression that the closed GB loop defect is fully relaxed to pristine lattice after a nearly 30 min of continuous beam exposure at 500 °C. However, examination a wider region of the area after the final frame showed that two dislocation cores far apart from each other were left (Figure 7-5a). Taking into account the dislocations in the bottom left of Figure 7-4o (position indicated by Figure 7-5b inset), the five dislocations can be regarded as two pairs with their slip planes indicated by the blue and orange lines in Figure 7-5b. By counting the number of slip planes between the parallel lines, it is able to tell that 110 carbon atoms have been removed to generate these two dislocation pairs. Since there are possibly other undetected dislocations (such as the one paired with the 5-7 dislocation in the upper inset in Figure 7-5b) and the dislocations in the insets could make further climb motions after migrating out of the imaging region, 110 is the minimum number of missing atoms. Therefore, the majority of atom losses occurs during the shape evolution process. This is also confirmed in the frame-by-frame structural study in Figure 7-6, where the structural reconfiguration of the GB loop is not only driven by bond rotations as previously reported (Figure 7-6a,b). [152] Occasional carbon dimer evaporation within the defect is also inevitable under 80 kV electron irradiation (Figure 7-6c,d). Previous work has demonstrated that a dislocation in graphene is a very stable form of defect. [56,140,143] It can only annihilate by combining with an opposite dislocation or migrate to the edge of graphene (See Chapter 4 for details). Thus, it can be concluded that isolated dislocations are the terminal state of a GB loop.

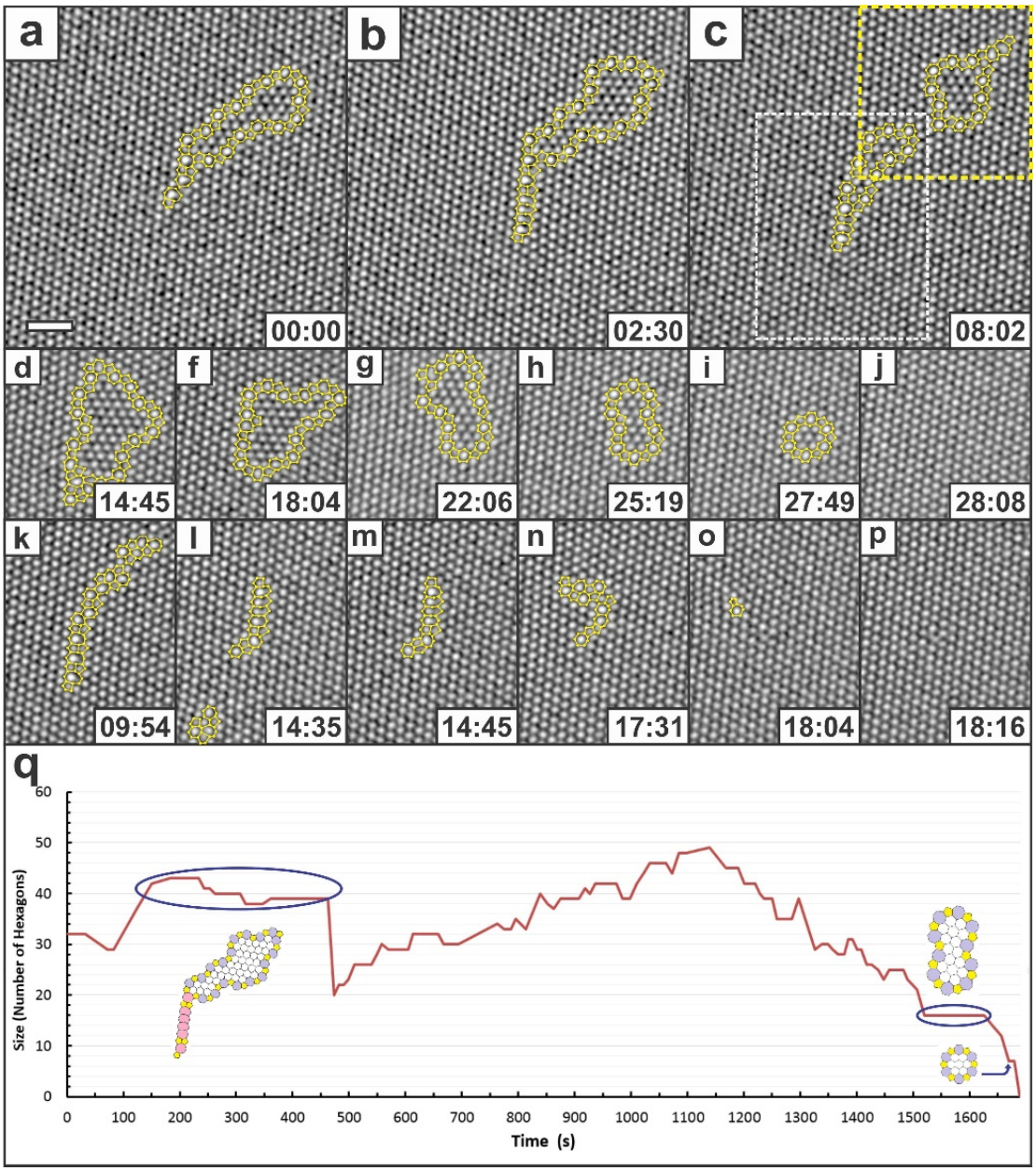

Figure 7-4. Structural evolution of the closed GB loop shown in Figure 7-2d at 500 °C. (a–c) Three time series frames showing the structural change of a GB loop in 8 min 2 s. In panel c, the initial GB loop splits into two smaller ones. The unwinding processes for both of them are presented in (d–j) and (k–p). (q) Line chart indicating the size change of the GB loop with time by counting the number of undistorted hexagons within the defect. The scale bar in panel a is 1 nm.

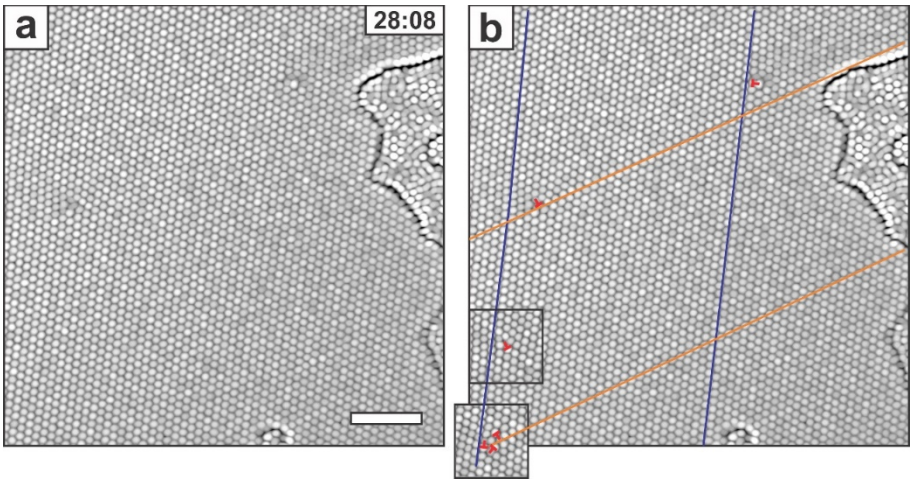

Figure 7-5. Maximum filtered AC-TEM image showing the final state of the GB loop shown in Figure 7-4 after 28 min 8 s beam irradiation. (a) Maximum filtered AC-TEM image. (b) Same TEM image as (a) with dislocations and their slip planes highlighted and overlapping insets showing the image of the same area at 18 min 4 s (upper) and 14 min 35 s (bottom), respectively. The scale bar in panel a is 2 nm.

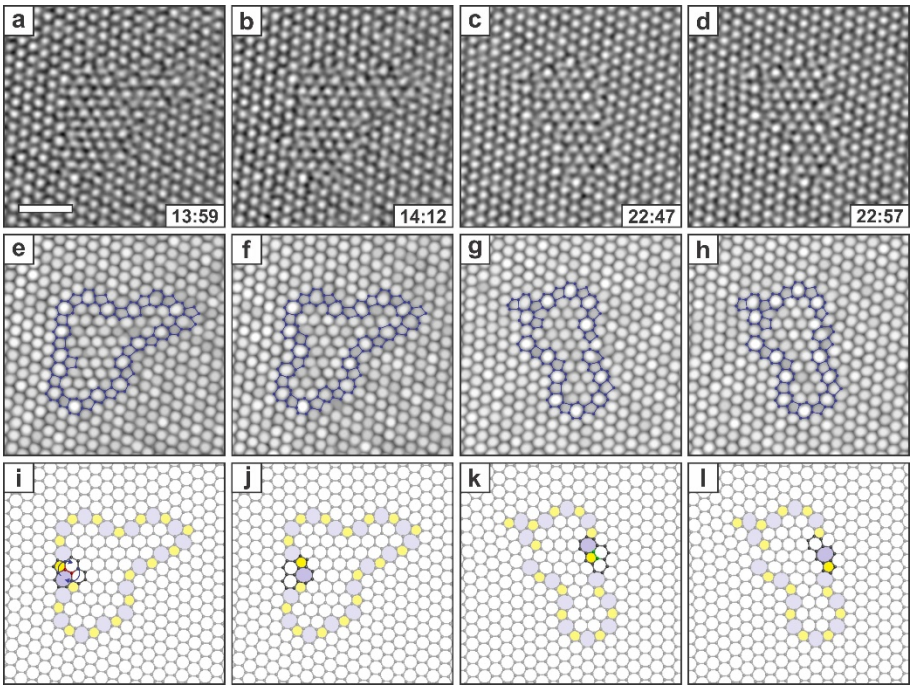

Figure 7-6. Structural change of the GB loop driven by bond rotation and carbon evaporation. (a,b) Bond rotation. (c,d) Carbon dimer evaporation. (e–h) Maximum filtered images. (i–l) Atomic models with atoms to be rotated highlighted in red and atoms to be sputtered colored in green. The scale bar in panel a is 1 nm.

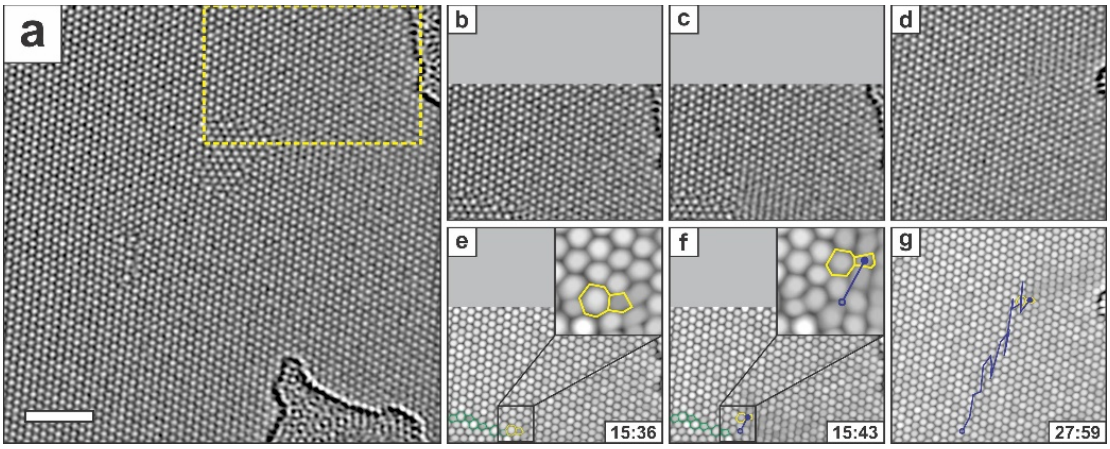

Figure 7-7. Ejection of a 5-7 dislocation during the unwinding process of the GB loop. (a) AC-TEM image showing the same GB loop as in Figure 4 at 15 min 36 s with the top right area cropped by the dashed box and presented in (b). (b–d) Time sequential images showing the separation of a 5-7 dislocation from the loop. (e–g) Maximum filtered images of (b–d), with the magnified view of the dislocation shown in the inset. The trajectory of the dislocation over the whole time period is presented in (g). The scale bar in panel a is 2 nm.

In Figure 7-7 the origin of the dislocation observed in the top right corner of Figure 7-5 is examined. The dislocation was initially a part of the GB (colored in yellow in Figure 7-7e), before being detached from the loop by migrating northeastwards (Figure 7-7c,f). This motion is equivalent to a basic glide plus basic climb steps. After that it continued migrating as an isolated dislocation *via* both bond rotation and atom evaporation just as previously reported. [56,139] The migration path over the next 12 min and 18 s is illustrated in Figure 7-7g. The results in Chapter 5 have suggested that it is of equal probability for a dislocation to glide along both directions in the slip plane, if there is no other defect nearby for the dislocation to interact with. [228] However, in Figure 7-7 it is apparent that the dislocation is inclined to glide away from GB loop, indicating that there may be a mutually exclusive interaction between them.

7.2.3 Evolution of GB at 800 °C

The process through which the GB loop in Figure 7-2a was observed to unwind is shown in Figure 7-8. The specimen temperature was maintained at 500 °C in the beginning. The “tail” of the defect (Figure 7-8a) was first relaxed within 4 min 47 s. The GB loop was relatively stable in the next 3 min 33 s with only minor structural changes taking place in the meantime (Figure 7-8b,c). Increasing the temperature to 800 °C afterwards resulted in the accelerated shape evolution of the defect, shown in Figure 7-8g–i. Figure 7-8g is not as clearly resolved as other images since the structural change happened so quickly, leaving insufficient time to adjust the thermal-expansion induced focus change. But the shape of the GB loop can still be recognized from the contrast inversion between the pristine lattice and the rotated one inside the loop. Similar to the observation at 500 °C, the defect separated into two smaller loops (Figure 7-8h), which reconfigured into a flower defect and a line defect respectively in Figure 7-8i. Both of them were observed to annealed back to pristine lattice in 8 min 11 s (Figure 7-8g–i and 7-9). It is also worth noticing that the Burger’s vector for the defect was initially 0 and became (1, 0) after the disappearance of the “tail” and was back to 0 again after the splitting into two parts (Figure 7-8l). One reasonable speculation is that the line defect attached to the GB loop in Figure 7-8a reconstructed into an isolated dislocation which soon after jumped out of the imaging area. Figure 7-8c and i there could be another dislocation emission event like in Figure 7-7, thus giving rise to the changes in the Burger’s vector.

In Figure 7-9, the structure and stability of the line defect cropped in Figure 7-8i is studied by showing time series frames at higher magnification. The line defect is

actually the assembly of 5 excess-atom defects with the atomic structure shown in Figure 7-1a. Prior work on excess-atom defects have been limited to smaller point defect structures with no observations of line defect made of carbon excess-atom. This long line excess-atom defect is unexpected since the graphene lattice keeps losing atoms over the imaging period as a result of irradiation damage. The 5 added carbon dimers were observed to be sputtered one after another in Figure 7-9. Robertson et al. have demonstrated that excess-atom defects are energetically unfavorable under 80 kV electron irradiation and the life time for high-order excess-atom defects (containing 4/6 additional atoms) is on a ~ 30 s time scale at room temperature. [116] However, in this work, the elimination of the line defect takes place in a deliberate manner at 800 °C and the average life span of each single excess-atom defect is ca. 112 s. If further considering that the sputtering of carbon atom is far more likely to occur at 800 °C than at room temperature, [228] it can be concluded that the stability of excess-atom defect is enhanced by generating a string of them, which makes its application in graphene defect nanoengineering more promising.

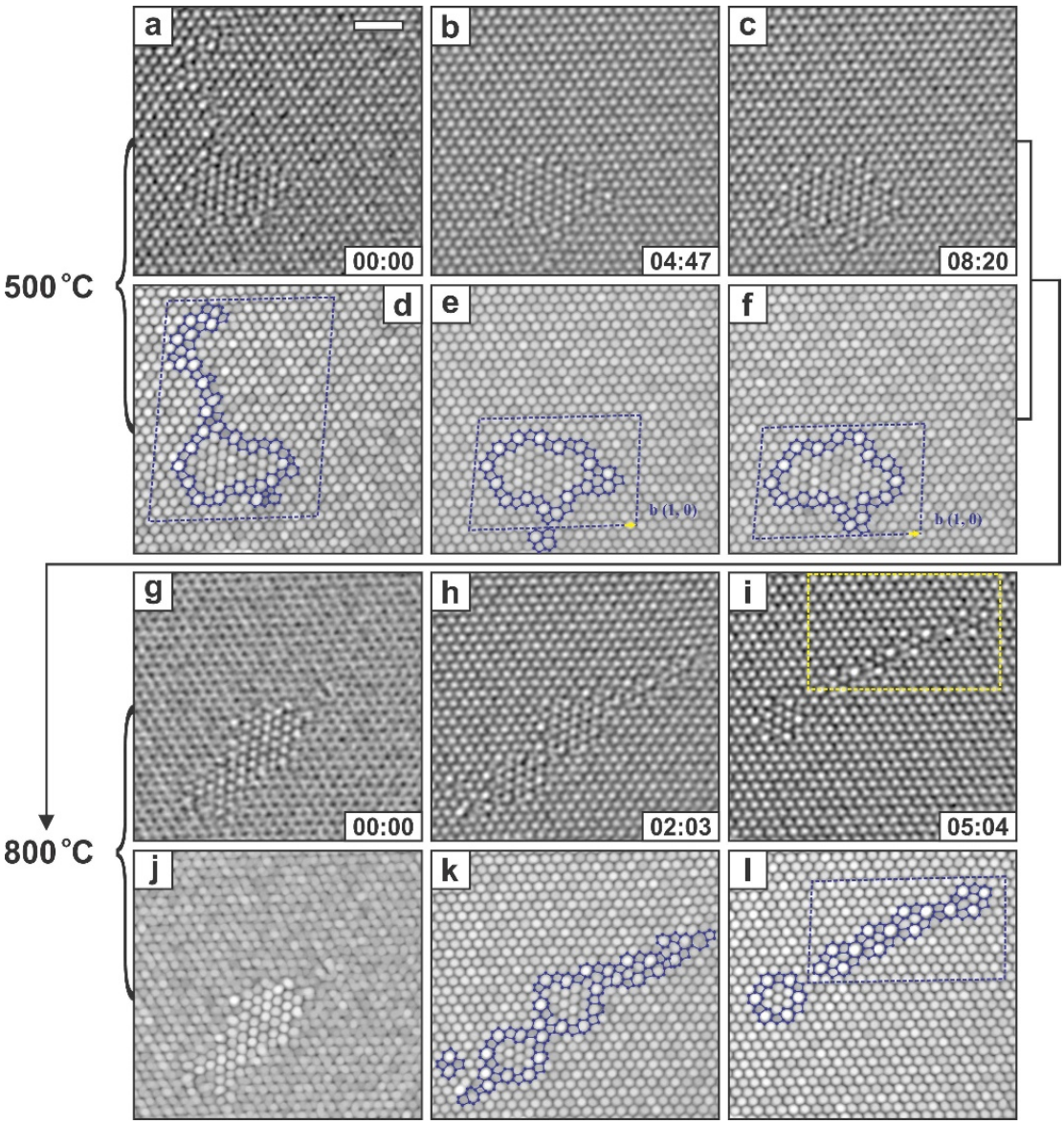

Figure 7-8. Time series of AC-TEM images showing the evolution of the GB loop from Figure 7-2a. (a–c,g–i) Gaussian filtered images. The temperature was increased from 500 °C to 800 °C between panel c and g. (d–f,j–k) Maximum filtered images with non-hexagonal rings, Burger's circuit and Burger's vector marked. The scale bar in panel a is 1 nm.

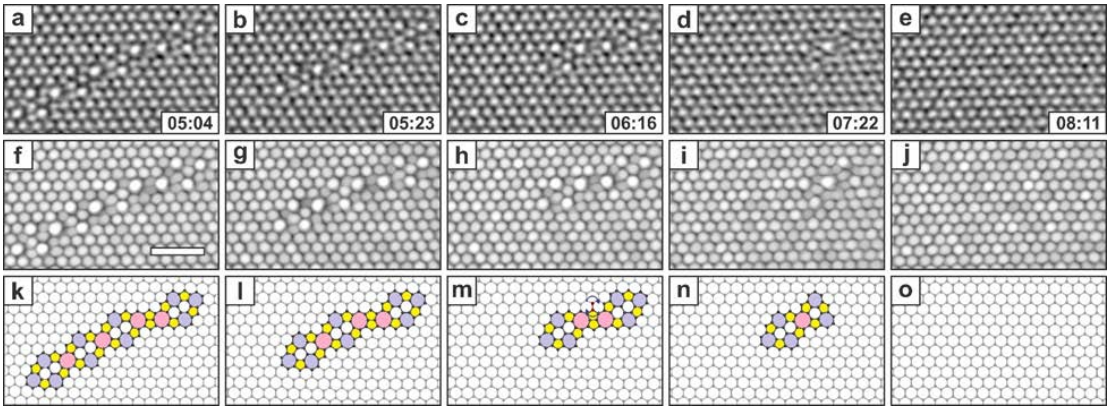

Figure 7-9. Evolution of a line defect assembled by carbon excess-atom defects. (a−e) Gaussian filtered AC-TEM images. Panel a shows magnified view of the cropped area in Figure 7-8i. (f−j) Maximum filtered images. (k−o) Corresponding atomic models. The scale bar in panel f is 1 nm.

7.3 Conclusion

In summary, high temperature *in situ* AC-TEM is used in this chapter to investigate the formation, evolution and annihilation of large closed GB loop defects in graphene with atomic resolution. It is shown that the unwinding of GB loop is accompanied with splitting into smaller loops and the emission of 5-7 dislocations. The GB loop can never be fully relaxed under beam irradiation with the final state being isolated dislocations nanometers away from one another. During the evolution process the formation of a line defect consisting of several adjacent excess-atom defects has been discovered, which is relatively robust even at 800 °C. It is also indicated that the flower defect consisting of 6 bond rotations in graphene could be produced by the unwinding of more complicated defect clusters, indicating that it originates from a top down change of larger closed loop structures into smaller ones, rather than from the bottom up by direct bond rotations. With all these results, this chapter aims to provide insights into the stability and dynamics of high order defects in graphene at elevated temperatures.

Chapter 8

Conclusions, and Future Outlook

8.1 Thesis summary

This doctorate thesis aims to provide a comprehensive and profound understanding of the atomic configuration and behavior of one-dimension defects (dislocation and GBs) in graphene, with the help of Oxford's state-of-the-art aberration-corrected high resolution transmission electron microscope and various advanced image analysis techniques. It can be divided into the following four broad areas of focus: (i) interactions between a 5-7 dislocation and the edge of graphene; (ii) high temperature behavior of isolated dislocations in graphene; (iii) *in situ* heterogeneous nucleation of graphene from Au nanoparticles; (iv) high temperature studies of a particular type of GB – GB loop.

8.2 Overall conclusions

The application of graphene's exceptional electronic properties is often hindered by the topological defects within the lattice. Also, some defects can be artificially introduced into graphene to tailor its properties for targeted applications. The modern AC-TEM system is particularly suited to investigating the structure and behavior of graphene

defects with single atom sensitivity. Recent advances in *in situ* microscopy further enables these studies at elevated temperatures.

The first part of the investigation was designed for the purpose of understanding the interaction between a 5-7 configured dislocation and the edge of graphene. In Chapter 4, it is demonstrated that when a dislocation is located near an edge, a decrease in the rippling and increase of the in-plane rotation occurs. The increased in-plane rotation near the edge causes bond rotations at the edge of graphene to reduce the overall strain in the system. Dislocations were highly stable and remained fixed in their position even when located within a few lattice spacings from the edge of graphene. These results show detailed information about the behavior of dislocations in 2D materials and the strain properties that result.

The use of a heating holder enables *in situ* heating experiments up to 800 °C performed in Chapter 5, 6 and 7. As described in Chapter 5, the control of temperature enables the differentiation of electron beam induced effects and thermally driven processes. At room temperature, the dynamics of dislocation behavior is driven by the electron beam irradiation at 80 kV; however at higher temperatures, increased movement of the dislocation is observed and provides evidence for the influence of thermal energy to the system. An analysis of the dislocation movement shows both climb and glide processes, including new complex pathways for migration and large nanoscale rapid jumps between fixed positions in the lattice. The improved understanding of the high temperature dislocation movement provides insights into annealing processes in graphene and the behavior of defects with increased heat.

In Chapter 6, the heterogeneous growth of graphene from Au nanoparticles in an AC-TEM is investigated. Heating monolayer graphene to an elevated temperature of 800 °C removes the majority of amorphous carbon adsorbates and leaves a clean surface. The aggregation of Au impurity atoms into nanoparticle clusters that are bound to the surface of monolayer graphene cause inhomogeneous nucleation of secondary graphene layers from carbon feedstock present within the microscope chamber. This enables the *in situ* study of heterogeneous nucleation and growth of graphene at the atomic level. In Chapter 6, it is shown that the growth mechanism consists of alternating C cluster attachment and indentation filling to maintain a uniform growth front of lowest energy. Back-folding of the graphene growth front is observed, followed by a reversal process that involves it flipping over and reattaching to the surrounding region. How the highly polycrystalline graphene seed evolves with time into a higher order crystalline structure is also indicated using a combination of AC-TEM and tight-binding molecular dynamics (TBMD) simulations. This helps understand the detailed lowest energy step-by-step pathways associated with GB migration and crystallization processes. The motion of the GB is discontinuous and mediated by both bond rotation and atom evaporation, supported by density functional theory calculations and TBMD. These results provide insights into the formation of crystalline seed domains that are generated during bottom-up graphene synthesis.

Finally, the configuration and dynamics of GB loops in graphene is examined at the atomic level in Chapter 7. Temperatures up to 800 °C are used to accelerate dynamic evolution of the defect clusters, increasing bond rotation and atomic addition/loss. As demonstrated in Chapter 7, the large closed GB loops relax under electron beam

irradiation into several isolated dislocations far apart from each other. Line defects composed of several adjacent excess-atom clusters can be found during the reconfiguration process. Dislocation ejection from the closed GB loops are seen in real time and are shown to help the reduction in loop size. These results show detailed information about the stability and behavior of large GB loops in 2D materials that have importance in the high temperature processing of these materials.

8.3 Future outlook

However, there is still much to learn about the dynamics of defects in graphene, such as the long-distance jump of dislocations in Chapter 5. The dynamics studies in this thesis is subjected to the scale of exposure time (0.5 – 2 s) and interval time (5 – 15 s) of image capturing. The future advance in CCD camera and anti-drifting technique will permit analysis of graphene defects with higher temporal resolution and more detailed dynamics. *In situ* electrical measurement can also be performed inside the TEM to experimentally correlate the presence of defects to the deviation of graphene electronic properties. Moreover, the studies of graphene defects in this thesis can be replicated to other 2D materials (*i.e.* h-BN, TMDCs) as the 2D family is rapidly expanding in recent years. The Z-contrast techniques in STEM will facilitate the atomic-scale imaging of binary 2D materials by providing atomic number related contrast.

References

[1] Novoselov, K. S.; Geim, A. K.; Morozov, S. V; Jiang, D.; Zhang, Y.; Dubonos, S. V; Grigorieva, I. V; Firsov, A. A. Electric Field Effect in Atomically Thin Carbon Films. *Science* **2004**, *306*, 666–669.

[2] Geim, A. K.; Novoselov, K. S. The Rise of Graphene. *Nat. Mater.* **2007**, *6*, 183–191.

[3] Nair, R. R.; Blake, P.; Grigorenko, A. N.; Novoselov, K. S.; Booth, T. J.; Stauber, T.; Peres, N. M. R.; Geim, A. K. Fine Structure Constant Defines Visual Transparency of Graphene. *Science* **2008**, *320*, 1308.

[4] Bonaccorso, F.; Colombo, L.; Yu, G.; Stoller, M.; Tozzini, V.; Ferrari, a. C.; Ruoff, R. S.; Pellegrini, V. Graphene, Related Two-Dimensional Crystals, and Hybrid Systems for Energy Conversion and Storage. *Science* **2015**, *347*, 1246501.

[5] Lee, C.; Wei, X.; Kysar, J. W.; Hone, J. Measurement of the Elastic Properties and Intrinsic Strength of Monolayer Graphene. *Science* **2008**, *321*, 385–388.

[6] Ghosh, S.; Bao, W.; Nika, D. L.; Subrina, S.; Pokatilov, E. P.; Lau, C. N.; Balandin, A. a. Dimensional Crossover of Thermal Transport in Few-Layer Graphene. *Nat. Mater.* **2010**, *9*, 555–558.

[7] Cai, W. W.; Moore, A. L.; Zhu, Y. W.; Li, X. S.; Chen, S. S.; Shi, L.; Ruoff, R. S. Thermal Transport in Suspended and Supported Monolayer Graphene Grown by Chemical Vapor Deposition. *Nano Lett.* **2010**, *10*, 1645–1651.

[8] Lau, C. N.; Bao, W.; Velasco, J. Properties of Suspended Graphene Membranes. *Mater. Today* **2012**, *15*, 238–245.

[9] Castro Neto, A. H.; Peres, N. M. R.; Novoselov, K. S.; Geim, A. K. The Electronic Properties of Graphene. *Rev. Mod. Phys.* **2009**, *81*, 109–162.

[10] Rao, C. N. R.; Biswas, K.; Subrahmanyam, K. S.; Govindaraj, A. Graphene, the New Nanocarbon. *J. Mater. Chem.* **2009**, *19*, 2457–2469.

[11] Katsnelson, M. I.; Novoselov, K. S.; Geim, A. K. Chirial Tunnelling and the Klein Paradox in Graphene. *Nat. Phys.* **2006**, *2*, 620–625.

[12] Du, X.; Skachko, I.; Andrei, E. Y.; Barker, A. Approaching Ballistic Transport in Suspended Graphene. *Nat. Nanotechnol.* **2008**, *3*, 491–495.

[13] Bolotin, K. I.; Sikes, K. J.; Jiang, Z.; Klima, M.; Fudenberg, G.; Hone, J.; Kim, P.; Stormer, H. L. Ultrahigh Electron Mobility in Suspended Graphene. *Solid State Commun.* **2008**, *146*, 351–355.

[14] Novoselov, K. S.; Geim, A. K.; Morozov, S. V; Jiang, D.; Katsnelson, M. I.;

Grigorieva, I. V; Dubonos, S. V; Firsov, A. A. Two-Dimensional Gas of Massless Dirac Fermions in Graphene. *Nature* **2005**, *438*, 197–200.

[15] Shytov, A.; Rudner, M.; Gu, N.; Katsnelson, M.; Levitov, L. Atomic Collapse, Lorentz Boosts, Klein Scattering, and Other Quantum-Relativistic Phenomena in Graphene. *Solid State Commun.* **2009**, *149*, 1087–1093.

[16] Hummers, W. S.; Offeman, R. E. Preparation of Graphitic Oxide. *J. Am. Chem. Soc.* **1958**, *80*, 1339.

[17] Dreyer, D. R.; Park, S.; Bielawski, C. W.; Ruoff, R. S. The Chemistry of Graphene Oxide. *Chem. Soc. Rev.* **2010**, *39*, 228–240.

[18] Badami, D. V. Graphitization of α-Silicon Carbide. *Nature* **1962**, *193*, 569–570.

[19] Wu, Z.-S.; Ren, W.; Gao, L.; Liu, B.; Jiang, C.; Cheng, H.-M. Synthesis of High-Quality Graphene with a Pre-Determined Number of Layers. *Carbon* **2009**, *47*, 493–499.

[20] Van Bommel, A. J.; Crombeen, J. E.; Van Tooren, A. LEED and Auger Electron Observations of the SiC(0001) Surface. *Surf. Sci.* **1975**, *48*, 463–472.

[21] Varchon, F.; Feng, R.; Hass, J.; Li, X.; Nguyen, B. N.; Naud, C.; Mallet, P.; Veuillen, J.-Y.; Berger, C.; Conrad, E. H.; et al. Electronic Structure of Epitaxial Graphene Layers on SiC: Effect of the Substrate. *Phys. Rev. Lett.* **2007**, *99*, 126805.

[22] May, J. W. Platinum Surface LEED Rings. *Surf. Sci.* **1969**, *17*, 267–270.

[23] Somani, P. R.; Somani, S. P.; Umeno, M. Planer Nano-Graphenes from Camphor by CVD. *Chem. Phys. Lett.* **2006**, *430*, 56–59.

[24] Eizenberg, M.; Blakely, J. M. Carbon Monolayer Phase Condensation on Ni(111). *Surf. Sci.* **1979**, *82*, 228–236.

[25] Wintterlin, J.; Bocquet, M. L. Graphene on Metal Surfaces. *Surf. Sci.* **2009**, *603*, 1841–1852.

[26] Batzill, M. The Surface Science of Graphene: Metal Interfaces, CVD Synthesis, Nanoribbons, Chemical Modifications, and Defects. *Surf. Sci. Rep.* **2012**, *67*, 83–115.

[27] Arco, L. De; Zhang, Y. Synthesis, Transfer, and Devices of Single-and Few-Layer Graphene by Chemical Vapor Deposition. *IEEE Trans. Nanotechnol.* **2009**, *8*, 135–138.

[28] Zhang, Y.; Gomez, L.; Ishikawa, F. N.; Madaria, A.; Ryu, K.; Wang, C.; Badmaev, A.; Zhou, C. Comparison of Graphene Growth on Single-Crystalline and Polycrystalline Ni by Chemical Vapor Deposition. *J. Phys. Chem. Lett.* **2010**, *1*, 3101–3107.

[29] Li, X.; Cai, W.; An, J.; Kim, S.; Nah, J.; Yang, D.; Piner, R.; Velamakanni, A.;

Jung, I.; Tutuc, E.; et al. Large-Area Synthesis of High-Quality and Uniform Graphene Films on Copper Foils. *Science* **2009**, *324*, 1312–1314.

[30] Kim, K. S.; Zhao, Y.; Jang, H.; Lee, S. Y.; Kim, J. M.; Ahn, J.-H.; Kim, P.; Choi, J.-Y.; Hong, B. H. Large-Scale Pattern Growth of Graphene Films for Stretchable Transparent Electrodes. *Nature* **2009**, *457*, 706–710.

[31] Reina, A.; Jia, X.; Ho, J.; Nezich, D.; Son, H.; Bulovic, V.; Dresselhaus, M. S.; Jing, K. Large Area, Few-Layer Graphene Films on Arbitrary Substrates by Chemical Vapor Deposition. *Nano Lett.* **2009**, *9*, 30–35.

[32] Wofford, J. M.; Nie, S.; McCarty, K. F.; Bartelt, N. C.; Dubon, O. D. Graphene Islands on Cu Foils: The Interplay between Shape, Orientation, and Defects. *Nano Lett.* **2010**, *10*, 4890–4896.

[33] Han, G. H.; Güneş, F.; Bae, J. J.; Kim, E. S.; Chae, S. J.; Shin, H. J.; Choi, J. Y.; Pribat, D.; Lee, Y. H. Influence of Copper Morphology in Forming Nucleation Seeds for Graphene Growth. *Nano Lett.* **2011**, *11*, 4144–4148.

[34] Luo, Z.; Lu, Y.; Singer, D. W.; Berck, M. E.; Somers, L. A.; Goldsmith, B. R.; Johnson, A. T. C. Effect of Substrate Roughness and Feedstock Concentration on Growth of Wafer-Scale Graphene at Atmospheric Pressure. *Chem. Mater.* **2011**, *23*, 1441–1447.

[35] Geng, D.; Wu, B.; Guo, Y.; Huang, L.; Xue, Y.; Chen, J.; Yu, G.; Jiang, L.; Hu, W.; Liu, Y. Uniform Hexagonal Graphene Flakes and Films Grown on Liquid Copper Surface. *Proc. Natl. Acad. Sci.* **2012**, *109*, 7992–7996.

[36] Wu, Y. A.; Fan, Y.; Speller, S.; Creeth, G. L.; Sadowski, J. T.; He, K.; Robertson, A. W.; Allen, C. S.; Warner, J. H. Large Single Crystals of Graphene on Melted Copper Using Chemical Vapor Deposition. *ACS Nano* **2012**, *6*, 5010–5017.

[37] An, H.; Lee, W.-J.; Jung, J. Graphene Synthesis on Fe Foil Using Thermal CVD. *Curr. Appl. Phys.* **2011**, *11*, S81–S85.

[38] Sutter, E.; Albrecht, P.; Sutter, P. Graphene Growth on Polycrystalline Ru Thin Films. *Appl. Phys. Lett.* **2009**, *95*, 133109.

[39] Liu, S. M. W. and Y. H. P. and X. W. and H. W. and Q. N. M. and H. W. T. and X. L. Z. and W. T. Z. and Y. C. Synthesis of Graphene on a Polycrystalline Co Film by Radio-Frequency Plasma-Enhanced Chemical Vapour Deposition. *J. Phys. D. Appl. Phys.* **2010**, *43*, 455402.

[40] Rut'kov, E. V; Kuz'michev, A. V; Gall', N. R. Carbon Interaction with Rhodium Surface: Adsorption, Dissolution, Segregation, Growth of Graphene Layers. *Phys. Solid State* **2011**, *53*, 1092–1098.

[41] Müller, F.; Grandthyll, S.; Zeitz, C.; Jacobs, K.; Hüfner, S.; Gsell, S.; Schreck, M. Epitaxial Growth of Graphene on Ir(111) by Liquid Precursor Deposition. *Phys. Rev. B* **2011**, *84*, 75472.

[42] Kwon, S. Y.; Ciobanu, C. V.; Petrova, V.; Shenoy, V. B.; Bareño, J.; Gambin, V.; Petrov, I.; Kodambaka, S. Growth of Semiconducting Graphene on Palladium. *Nano Lett.* **2009**, *9*, 3985–3990.

[43] Gao, T.; Xie, S.; Gao, Y.; Liu, M.; Chen, Y.; Zhang, Y.; Liu, Z. Growth and Atomic-Scale Characterizations of Graphene on Multifaceted Textured Pt Foils Prepared by Chemical Vapor Deposition. *ACS Nano* **2011**, *5*, 9194–9201.

[44] Oznuluer, T.; Pince, E.; Polat, E. O.; Balci, O.; Salihoglu, O.; Kocabas, C. Synthesis of Graphene on Gold. *Appl. Phys. Lett.* **2011**, *98*, 183101.

[45] Zhang, Y.; Zhang, L.; Zhou, C. Review of Chemical Vapor Deposition of Graphene and Related Applications. *Acc. Chem. Res.* **2013**, *46*, 2329–2339.

[46] Liu, Y.; Zou, X.; Yakobson, B. I. Dislocations and Grain Boundaries in Two-Dimensional Boron Nitride. *ACS Nano* **2012**, *6*, 7053–7058.

[47] Yazyev, O. V; Louie, S. G. Electronic Transport in Polycrystalline Graphene. *Nat. Mater.* **2010**, *9*, 806–809.

[48] Compagnini, G.; Giannazzo, F.; Sonde, S. Ion Irradiation and Defect Formation in Single Layer Graphene. *Carbon* **2009**, *47*, 3201–3207.

[49] Nordlund, K.; Keinonen, J.; Mattila, T. Formation of Ion Irradiation Induced Small-Scale Defects on Graphite Surfaces. *Phys. Rev. Lett.* **1996**, *77*, 699–702.

[50] Hirsch, P. B.; Horne, R. W.; Whelan, M. J. Direct Observations of the Arrangement and Motion of Dislocations in Aluminium. *Philos. Mag.* **1956**, *1*, 677–684.

[51] Hirsch, P.; Cockayne, D.; Spence, J.; Whelan, M. 50 Years of TEM of Dislocations: Past, Present and Future. *Philos. Mag.* **2006**, *86*, 4519–4528.

[52] Iijima, S.; Allpress, J. G. Structural Studies by High-Resolution Electron Microscopy: Tetragonal Tungsten Bronze-Type Structures in the System Nb2O5-WO3. *Acta Crystallogr. Sect. A* **1974**, *30*, 22–29.

[53] Sinclair, R.; Dutkiewicz, J. Lattice Imaging of the B19 Ordering Transformation and Interfacial Structures in Mg3Cd. *Acta Metall.* **1977**, *25*, 235–249.

[54] Krivanek, O. L.; Isoda, S.; Kobayashi, K. Lattice Imaging of a Grain Boundary in Crystalline Germanium. *Philos. Mag.* **1977**, *36*, 931–940.

[55] Warner, J. H.; Mukai, M.; Kirkland, A. I. Atomic Structure of ABC Rhombohedral Stacked Trilayer Graphene. *ACS Nano* **2012**, *6*, 5680–5686.

[56] Warner, J. H.; Margine, E. R.; Mukai, M.; Robertson, A. W.; Giustino, F.; Kirkland, A. I. Dislocation-Driven Deformations in Graphene. *Science* **2012**, *337*, 209–212.

[57] Batson, P. E.; Dellby, N.; Krivanek, O. L. Sub-Ångstrom Resolution Using Aberration Corrected Electron Optics. *Nature* **2002**, *418*, 617–620.

[58] Egerton, R. F.; Li, P.; Malac, M. Radiation Damage in the TEM and SEM. *Micron* **2004**, *35*, 399–409.

[59] Egerton, R. F.; McLeod, R.; Wang, F.; Malac, M. Basic Questions Related to Electron-Induced Sputtering in the TEM. *Ultramicroscopy* **2010**, *110*, 991–997.

[60] Smith, B. W.; Luzzi, D. E. Electron Irradiation Effects in Single Wall Carbon Nanotubes. *J. Appl. Phys.* **2001**, *90*, 3509–3515.

[61] Susi, T.; Kotakoski, J.; Arenal, R.; Kurasch, S.; Jiang, H.; Skakalova, V.; Stephan, O.; Krasheninnikov, A. V.; Kauppinen, E. I.; Kaiser, U.; et al. Atomistic Description of Electron Beam Damage in Nitrogen-Doped Graphene and Single-Walled Carbon Nanotubes. *ACS Nano* **2012**, *6*, 8837–8846.

[62] Banhart, F. The Formation of a Connection between Carbon Nanotubes in an Electron Beam. *Nano Lett.* **2001**, *1*, 329–332.

[63] Crespi, V.; Chopra, N.; Cohen, M.; Zettl, A.; Louie, S. Anisotropic Electron-Beam Damage and the Collapse of Carbon Nanotubes. *Phys. Rev. B* **1996**, *54*, 5927–5931.

[64] Zobelli, A.; Gloter, A.; Ewels, C. P.; Seifert, G.; Colliex, C. Electron Knock-on Cross Section of Carbon and Boron Nitride Nanotubes. *Phys. Rev. B* **2007**, *75*.

[65] Krasheninnikov, A. V.; Banhart, F.; Li, J. X.; Foster, A. S.; Nieminen, R. M. Stability of Carbon Nanotubes under Electron Irradiation: Role of Tube Diameter and Chirality. *Phys. Rev. B: Condens. Matter Mater. Phys.* **2005**, *72*.

[66] Meyer, J. C.; Eder, F.; Kurasch, S.; Skakalova, V.; Kotakoski, J.; Park, H. J.; Roth, S.; Chuvilin, A.; Eyhusen, S.; Benner, G.; et al. Accurate Measurement of Electron Beam Induced Displacement Cross Sections for Single-Layer Graphene. *Phys. Rev. Lett.* **2012**, *108*.

[67] Kotakoski, J.; Santos-Cottin, D.; Krasheninnikov, A. V. Stability of Graphene Edges under Electron Beam: Equilibrium Energetics versus Dynamic Effects. *ACS Nano* **2012**, *6*, 671–676.

[68] Garaj, S.; Hubbard, W.; Reina, A.; Kong, J.; Branton, D.; Golovchenko, J. A. Graphene as a Subnanometre Trans-Electrode Membrane. *Nature* **2010**, *467*, 190–193.

[69] Rodriguez-Manzo, J. A.; Banhart, F. Creation of Individual Vacancies in Carbon Nanotubes by Using an Electron Beam of 1 Å Diameter. *Nano Lett.* **2009**, *9*, 2285–2289.

[70] Fischbein, M. D.; Drndić, M. Electron Beam Nanosculpting of Suspended Graphene Sheets. *Appl. Phys. Lett.* **2008**, *93*, 113107.

[71] Krasheninnikov, A. V; Banhart, F. Engineering of Nanostructured Carbon Materials with Electron or Ion Beams. *Nat. Mater.* **2007**, *6*, 723–733.

[72] Lusk, M. T.; Carr, L. D. Nanoengineering Defect Structures on Graphene. *Phys. Rev. Lett.* **2008**, *100*.

[73] Robertson, A. W.; Allen, C. S.; Wu, Y. A.; He, K.; Olivier, J.; Neethling, J.; Kirkland, A. I.; Warner, J. H. Spatial Control of Defect Creation in Graphene at the Nanoscale. *Nat. Commun.* **2012**, *3*, 1144.

[74] Stone, A. J.; Wales, D. J. Theoretical Studies of Icosahedral C60 and Some Related Species. *Chem. Phys. Lett.* **1986**, *128*, 501–503.

[75] Ma, J.; Alfè, D.; Michaelides, A.; Wang, E. Stone-Wales Defects in Graphene and Other Planar sp2-Bonded Materials. *Phys. Rev. B* **2009**, *80*, 33407.

[76] Li, L.; Reich, S.; Robertson, J. Defect Energies of Graphite: Density-Functional Calculations. *Phys. Rev. B* **2005**, *72*, 184109.

[77] Meyer, J. C.; Kisielowski, C.; Erni, R.; Rossell, M. D.; Crommie, M. F.; Zettl, A. Direct Imaging of Lattice Atoms and Topological Defects in Graphene Membranes. *Nano Lett.* **2008**, *8*, 3582–3586.

[78] Banhart, F.; Kotakoski, J.; Krasheninnikov, A. V. Structural Defects in Graphene. *ACS Nano* **2011**, *5*, 26–41.

[79] Peng, X.; Ahuja, R. Symmetry Breaking Induced Bandgap in Epitaxial Graphene Layers on SiC. *Nano Lett.* **2008**, *8*, 4464–4468.

[80] Robertson, A. W.; Montanari, B.; He, K.; Allen, C. S.; Wu, Y. A.; Harrison, N. M.; Kirkland, A. I.; Warner, J. H. Structural Reconstruction of the Graphene Monovacancy. *ACS Nano* **2013**, *7*, 4495–4502.

[81] Ugeda, M. M.; Brihuega, I.; Guinea, F.; Gómez-Rodríguez, J. M. Missing Atom as a Source of Carbon Magnetism. *Phys. Rev. Lett.* **2010**, *104*, 96804.

[82] Gass, M. H.; Bangert, U.; Bleloch, A. L.; Wang, P.; Nair, R. R.; Geim, A. K. Free-Standing Graphene at Atomic Resolution. *Nat. Nanotechnol.* **2008**, *3*, 676–681.

[83] Lu, A.; Pan, B. Nature of Single Vacancy in Achiral Carbon Nanotubes. *Phys. Rev. Lett.* **2004**, *92*, 105504.

[84] Rossato, J.; Baierle, R. J.; Fazzio, A.; Mota, R. Vacancy Formation Process in Carbon Nanotubes: First-Principles Approach. *Nano Lett.* **2005**, *5*, 197–200.

[85] Berber, S.; Oshiyama, A. Reconstruction of Mono-Vacancies in Carbon Nanotubes: Atomic Relaxation vs. Spin Polarization. *Phys. B Condens. Matter* **2006**, *376*, 272–275.

[86] Lehtinen, P.; Foster, A.; Ma, Y.; Krasheninnikov, A.; Nieminen, R. Irradiation-Induced Magnetism in Graphite: A Density Functional Study. *Phys. Rev. Lett.* **2004**, *93*, 187202.

[87] Ewels, C.; Telling, R.; El-Barbary, A.; Heggie, M.; Briddon, P. Metastable Frenkel Pair Defect in Graphite: Source of Wigner Energy? *Phys. Rev. Lett.*

2003, *91*, 25505.

[88] El-Barbary, A.; Telling, R.; Ewels, C.; Heggie, M.; Briddon, P. Structure and Energetics of the Vacancy in Graphite. *Phys. Rev. B* **2003**, *68*, 144107.

[89] Krasheninnikov, A. V.; Lehtinen, P. O.; Foster, A. S.; Nieminen, R. M. Bending the Rules: Contrasting Vacancy Energetics and Migration in Graphite and Carbon Nanotubes. *Chem. Phys. Lett.* **2006**, *418*, 132–136.

[90] Tang, M.; Colombo, L.; Zhu, J.; de la Rubia, T. Intrinsic Point Defects in Crystalline Silicon: Tight-Binding Molecular Dynamics Studiesof Self-Diffusion, Interstitial-Vacancy Recombination, and Formation Volumes. *Phys. Rev. B* **1997**, *55*, 14279–14289.

[91] Maier, K.; Peo, M.; Saile, B.; Schaefer, H. E.; Seeger, a. High–temperature Positron Annihilation and Vacancy Formation in Refractory Metals. *Philos. Mag. A* **1979**, *40*, 701–728.

[92] Yazyev, O. V.; Helm, L. Defect-Induced Magnetism in Graphene. *Phys. Rev. B* **2007**, *75*.

[93] Topsakal, M.; Aktürk, E.; Sevinçli, H.; Ciraci, S. First-Principles Approach to Monitoring the Band Gap and Magnetic State of a Graphene Nanoribbon via Its Vacancies. *Phys. Rev. B: Condens. Matter Mater. Phys.* **2008**, *78*.

[94] Wang, H.; Wang, Q.; Cheng, Y.; Li, K.; Yao, Y.; Zhang, Q.; Dong, C.; Wang, P.; Schwingenschlögl, U.; Yang, W.; et al. Doping Monolayer Graphene with Single Atom Substitutions. *Nano Lett.* **2012**, *12*, 141–144.

[95] Kotakoski, J.; Krasheninnikov, A. V.; Kaiser, U.; Meyer, J. C. From Point Defects in Graphene to Two-Dimensional Amorphous Carbon. *Phys. Rev. Lett.* **2011**, *106*, 105505.

[96] Kim, Y.; Ihm, J.; Yoon, E.; Lee, G.-D. Dynamics and Stability of Divacancy Defects in Graphene. *Phys. Rev. B* **2011**, *84*, 75445.

[97] Lee, G. Do; Wang, C. Z.; Yoon, E.; Hwang, N. M.; Kim, D. Y.; Ho, K. M. Diffusion, Coalescence, and Reconstruction of Vacancy Defects in Graphene Layers. *Phys. Rev. Lett.* **2005**, *95*.

[98] Kotakoski, J.; Meyer, J. C.; Kurasch, S.; Santos-Cottin, D.; Kaiser, U.; Krasheninnikov, A. V. Stone-Wales-Type Transformations in Carbon Nanostructures Driven by Electron Irradiation. *Phys. Rev. B* **2011**, *83*, 245420.

[99] Chen, Q.; Robertson, A. W.; He, K.; Gong, C.; Yoon, E.; Lee, G.-D.; Warner, J. H. Atomic Level Distributed Strain within Graphene Divacancies from Bond Rotations. *ACS Nano* **2015**, *9*, 8599–8608.

[100] Banhart, F. Irradiation Effects in Carbon Nanostructures. *Reports Prog. Phys.* **1999**, *62*, 1181–1221.

[101] Kotakoski, J.; Mangler, C.; Meyer, J. C. Imaging Atomic-Level Random Walk

of a Point Defect in Graphene. *Nat. Commun.* **2014**, *5*, 3991.

[102] Robertson, A. W.; Lee, G.-D.; He, K.; Yoon, E.; Kirkland, A. I.; Warner, J. H. The Role of the Bridging Atom in Stabilizing Odd Numbered Graphene Vacancies. *Nano Lett.* **2014**, *14*, 3972–3980.

[103] Kotakoski, J.; Krasheninnikov, A. V.; Nordlund, K. Energetics, Structure, and Long-Range Interaction of Vacancy-Type Defects in Carbon Nanotubes: Atomistic Simulations. *Phys. Rev. B* **2006**, *74*.

[104] Dai, X. Q.; Zhao, J. H.; Xie, M. H.; Tang, Y. N.; Li, Y. H.; Zhao, B. First-Principle Study of Magnetism Induced by Vacancies in Graphene. *Eur. Phys. J. B* **2011**, *80*, 343–349.

[105] Faccio, R.; Mombrú, A. W. Magnetism in Multivacancy Graphene Systems. *J. Phys. Condens. Matter* **2012**, *24*, 375304.

[106] Dai, X. Q.; Zhao, J. H.; Xie, M. H.; Tang, Y. N.; Li, Y. H.; Zhao, B. First-Principle Study of Magnetism Induced by Vacancies in Graphene. *Eur. Phys. J. B* **2011**, *80*, 343–349.

[107] Robertson, A. W.; Lee, G.-D.; He, K.; Yoon, E.; Kirkland, A. I.; Warner, J. H. Stability and Dynamics of the Tetravacancy in Graphene. *Nano Lett.* **2014**, *14*, 1634–1642.

[108] Robertson, A. W.; Warner, J. H. Atomic Resolution Imaging of Graphene by Transmission Electron Microscopy. *Nanoscale* **2013**, *5*, 4079–4093.

[109] Lahiri, J.; Lin, Y.; Bozkurt, P.; Oleynik, I. I.; Batzill, M. An Extended Defect in Graphene as a Metallic Wire. *Nat. Nanotechnol.* **2010**, *5*, 326–329.

[110] Botello-Méndez, A. R.; Declerck, X.; Terrones, M.; Terrones, H.; Charlier, J. C. One-Dimensional Extended Lines of Divacancy Defects in Graphene. *Nanoscale* **2011**, *3*, 2868–2872.

[111] Alexandre, S. S.; Lúcio, A. D.; Neto, A. H. C.; Nunes, R. W. Correlated Magnetic States in Extended One-Dimensional Defects in Graphene. *Nano Lett.* **2012**, *12*, 5097–5102.

[112] Robertson, A. W.; Lee, G.-D.; He, K.; Gong, C.; Chen, Q.; Yoon, E.; Kirkland, A. I.; Warner, J. H. Atomic Structure of Graphene Subnanometer Pores. *ACS Nano* **2015**, *9*, 11599–11607.

[113] Tsetseris, L.; Pantelides, S. T. Adatom Complexes and Self-Healing Mechanisms on Graphene and Single-Wall Carbon Nanotubes. *Carbon* **2009**, *47*, 901–908.

[114] Lee, Y.; Kim, S.; Tománek, D. Catalytic Growth of Single-Wall Carbon Nanotubes: An Ab Initio Study. *Phys. Rev. Lett.* **1997**, *78*, 2393–2396.

[115] Lehtinen, P.; Foster, A.; Ayuela, A.; Krasheninnikov, A.; Nordlund, K.; Nieminen, R. Magnetic Properties and Diffusion of Adatoms on a Graphene

Sheet. *Phys. Rev. Lett.* **2003**, *91*, 17202.

[116] Robertson, A. W.; He, K.; Kirkland, A. I.; Warner, J. H. Inflating Graphene with Atomic Scale Blisters. *Nano Lett.* **2014**, *14*, 908–914.

[117] Lusk, M. T.; Carr, L. D. Creation of Graphene Allotropes Using Patterned Defects. *Carbon* **2009**, *47*, 2226–2232.

[118] Orlikowski, D.; Buongiorno Nardelli, M.; Bernholc, J.; Roland, C. Ad-Dimers on Strained Carbon Nanotubes: A New Route for Quantum Dot Formation? *Phys. Rev. Lett.* **1999**, *83*, 4132–4135.

[119] Sternberg, M.; Curtiss, L. A.; Gruen, D. M.; Kedziora, G.; Horner, D. A.; Redfern, P. C.; Zapol, P. Carbon Ad-Dimer Defects in Carbon Nanotubes. *Phys. Rev. Lett.* **2006**, *96*.

[120] Lusk, M. T.; Wu, D. T.; Carr, L. D. Graphene Nanoengineering and the Inverse Stone-Thrower-Wales Defect. *Phys. Rev. B* **2010**, *81*, 155444.

[121] Ewels, C. P.; Heggie, M. I.; Briddon, P. R. Adatoms and Nanoengineering of Carbon. *Chem. Phys. Lett.* **2002**, *351*, 178–182.

[122] Carpio, A.; Bonilla, L. L. Periodized Discrete Elasticity Models for Defects in Graphene. *Phys. Rev. B* **2008**, *78*.

[123] Chen, S.; Chrzan, D. C. Continuum Theory of Dislocations and Buckling in Graphene. *Phys. Rev. B* **2011**, *84*.

[124] Grantab, R.; Shenoy, V. B.; Ruoff, R. S. Anomalous Strength Characteristics of Tilt Grain Boundaries in Graphene. *Science* **2010**, *330*, 946–948.

[125] Bonilla, L. L.; Carpio, A. Driving Dislocations in Graphene. *Science* **2012**, *337*, 161–162.

[126] Cockayne, D. J. H.; Ray, I. L. F.; Whelan, M. J. Investigations of Dislocation Strain Fields Using Weak Beams. *Philos. Mag.* **1969**, *20*, 1265–1270.

[127] Zaretskii, A. V; Osipyan, Y. A.; Petrenko, V. F.; Strukova, G. K.; Khodos, I. I. The Isolated Partial and Dissociated Total Dislocations in Deformed ZnS Crystals. *Philos. Mag. A* **1983**, *48*, 279–285.

[128] Hashimoto, A.; Suenaga, K.; Gloter, A.; Urita, K.; Iijima, S. Direct Evidence for Atomic Defects in Graphene Layers. *Nature* **2004**, *430*, 17–20.

[129] Huang, P. Y.; Ruiz-Vargas, C. S.; van der Zande, A. M.; Whitney, W. S.; Levendorf, M. P.; Kevek, J. W.; Garg, S.; Alden, J. S.; Hustedt, C. J.; Zhu, Y.; et al. Grains and Grain Boundaries in Single-Layer Graphene Atomic Patchwork Quilts. *Nature* **2011**, *469*, 389–392.

[130] Meyer, J. C.; Kurasch, S.; Park, H. J.; Skakalova, V.; Künzel, D.; Gross, A.; Chuvilin, A.; Algara-Siller, G.; Roth, S.; Iwasaki, T.; et al. Experimental Analysis of Charge Redistribution due to Chemical Bonding by High-Resolution Transmission Electron Microscopy. *Nat. Mater.* **2011**, *10*, 209–215.

[131] Suenaga, K.; Koshino, M. Atom-by-Atom Spectroscopy at Graphene Edge. *Nature* **2010**, *468*, 1088–1090.

[132] Krivanek, O. L.; Chisholm, M. F.; Nicolosi, V.; Pennycook, T. J.; Corbin, G. J.; Dellby, N.; Murfitt, M. F.; Own, C. S.; Szilagyi, Z. S.; Oxley, M. P.; et al. Atom-by-Atom Structural and Chemical Analysis by Annular Dark-Field Electron Microscopy. *Nature* **2010**, *464*, 571–574.

[133] Warner, J. H.; Young, N. P.; Kirkland, A. I.; Briggs, G. A. D. Resolving Strain in Carbon Nanotubes at the Atomic Level. *Nat. Mater.* **2011**, *10*, 958–962.

[134] Warner, J. H.; Rümmeli, M. H.; Ge, L.; Gemming, T.; Montanari, B.; Harrison, N. M.; Büchner, B.; Briggs, G. A. D. Structural Transformations in Graphene Studied with High Spatial and Temporal Resolution. *Nat. Nanotechnol.* **2009**, *4*, 500–504.

[135] Liu, Z.; Suenaga, K.; Harris, P. J. F.; Iijima, S. Open and Closed Edges of Graphene Layers. *Phys. Rev. Lett.* **2009**, *102*.

[136] Amelinckx, S.; Delavignette, P. Dislocation Loops Due to Quenched-in Point Defects in Graphite. *Phys. Rev. Lett.* **1960**, *5*, 50–51.

[137] Delavignette, P.; Amelinckx, S. Dislocation Patterns in Graphite. *J. Nucl. Mater.* **1962**, *5*, 17–66.

[138] Roscoe, C.; Thomas, J. M. The Revelation of Small-Angle Boundaries and Forest Dislocations in Graphite Monocrystals. *Carbon* **1966**, *4*, 383–390.

[139] Lehtinen, O.; Kurasch, S.; Krasheninnikov, A. V.; Kaiser, U. Atomic Scale Study of the Life Cycle of a Dislocation in Graphene from Birth to Annihilation. *Nat. Commun.* **2013**, *4*, 2098.

[140] Jeong, B.; Ihm, J.; Lee, G.-D. Stability of Dislocation Defect with Two Pentagon-Heptagon Pairs in Graphene. *Phys. Rev. B* **2008**, *78*, 165403.

[141] Lee, S.; Hwang, G. S. Valence Force Field-Based Monte Carlo Bond-Rotation Method for the Determination of sp2-Bonded Carbon Structures. *J. Appl. Phys.* **2011**, *110*.

[142] Chen, S.; Ertekin, E.; Chrzan, D. C. Plasticity in Carbon Nanotubes: Cooperative Conservative Dislocation Motion. *Phys. Rev. B* **2010**, *81*, 155417.

[143] Lee, G.-D.; Yoon, E.; He, K.; Robertson, A. W.; Warner, J. H. Detailed Formation Processes of Stable Dislocations in Graphene. *Nanoscale* **2014**, *6*, 14836–14844.

[144] Meyer, J. C.; Geim, A. K.; Katsnelson, M. I.; Novoselov, K. S.; Booth, T. J.; Roth, S. The Structure of Suspended Graphene Sheets. *Nature* **2007**, *446*, 60–63.

[145] Wang, W. L.; Bhandari, S.; Yi, W.; Bell, D. C.; Westervelt, R.; Kaxiras, E. Direct Imaging of Atomic-Scale Ripples in Few-Layer Graphene. *Nano Lett.*

2012, *12*, 2278–2282.

[146] Kirilenko, D. A.; Dideykin, A. T.; Van Tendeloo, G. Measuring the Corrugation Amplitude of Suspended and Supported Graphene. *Phys. Rev. B* **2011**, *84*.

[147] Lui, C. H.; Liu, L.; Mak, K. F.; Flynn, G. W.; Heinz, T. F. Ultraflat Graphene. *Nature* **2009**, *462*, 339–341.

[148] Liu, Y.; Yakobson, B. I. Cones, Pringles, and Grain Boundary Landscapes in Graphene Topology. *Nano Lett.* **2010**, *10*, 2178–2183.

[149] Yakobson, B. I.; Ding, F. Observational Geology of Graphene, at the Nanoscale. *ACS Nano* **2011**, *5*, 1569–1574.

[150] Warner, J. H.; Fan, Y.; Robertson, A. W.; He, K.; Yoon, E.; Lee, G.-D. Rippling Graphene at the Nanoscale through Dislocation Addition. *Nano Lett.* **2013**, *13*, 4937–4944.

[151] An, J.; Voelkl, E.; Suk, J. W.; Li, X.; Magnuson, C. W.; Fu, L.; Tiemeijer, P.; Bischoff, M.; Freitag, B.; Popova, E.; et al. Domain (Grain) Boundaries and Evidence of "Twinlike" Structures in Chemically Vapor Deposited Grown Graphene. *ACS Nano* **2011**, *5*, 2433–2439.

[152] Kurasch, S.; Kotakoski, J.; Lehtinen, O.; Skákalová, V.; Smet, J.; Krill, C. E.; Krasheninnikov, A. V; Kaiser, U. Atom-by-Atom Observation of Grain Boundary Migration in Graphene. *Nano Lett.* **2012**, *12*, 3168–3173.

[153] Yang, B.; Xu, H.; Lu, J.; Loh, K. P. Periodic Grain Boundaries Formed by Thermal Reconstruction of Polycrystalline Graphene Film. *J. Am. Chem. Soc.* **2014**, *136*, 12041–12046.

[154] Westenfelder, B.; Meyer, J. C.; Biskupek, J.; Kurasch, S.; Scholz, F.; Krill, C. E.; Kaiser, U. Transformations of Carbon Adsorbates on Graphene Substrates under Extreme Heat. *Nano Lett.* **2011**, *11*, 5123–5127.

[155] Kim, D.; Kim, Y.; Ihm, J.; Yoon, E.; Lee, G.-D. Atomic-Scale Mechanism of Grain Boundary Motion in Graphene. *Carbon* **2015**, *84*, 146–150.

[156] Wei, Y.; Wu, J.; Yin, H.; Shi, X.; Yang, R.; Dresselhaus, M. The Nature of Strength Enhancement and Weakening by Pentagon–heptagon Defects in Graphene. *Nat. Mater.* **2012**, *11*, 759–763.

[157] Kotakoski, J.; Meyer, J. C. Mechanical Properties of Polycrystalline Graphene Based on a Realistic Atomistic Model. *Phys. Rev. B* **2012**, *85*, 195447.

[158] Rasool, H. I.; Ophus, C.; Zhang, Z.; Crommie, M. F.; Yakobson, B. I.; Zettl, A. Conserved Atomic Bonding Sequences and Strain Organization of Graphene Grain Boundaries. *Nano Lett.* **2014**, *14*, 7057–7063.

[159] Rasool, H. I.; Ophus, C.; Klug, W. S.; Zettl, A.; Gimzewski, J. K. Measurement of the Intrinsic Strength of Crystalline and Polycrystalline

Graphene. *Nat. Commun.* **2013**, *4*, 2811.

[160] Lee, G.-H.; Cooper, R. C.; An, S. J.; Lee, S.; van der Zande, A.; Petrone, N.; Hammerberg, A. G.; Lee, C.; Crawford, B.; Oliver, W.; et al. High-Strength Chemical-Vapor-Deposited Graphene and Grain Boundaries. *Science* **2013**, *340*, 1073–1076.

[161] Tsen, A. W.; Brown, L.; Levendorf, M. P.; Ghahari, F.; Huang, P. Y.; Havener, R. W.; Ruiz-Vargas, C. S.; Muller, D. a; Kim, P.; Park, J. Tailoring Electrical Transport across Grain Boundaries in Polycrystalline Graphene. *Science* **2012**, *336*, 1143–1146.

[162] Yu, Q.; Jauregui, L. A.; Wu, W.; Colby, R.; Tian, J.; Su, Z.; Cao, H.; Liu, Z.; Pandey, D.; Wei, D.; et al. Control and Characterization of Individual Grains and Grain Boundaries in Graphene Grown by Chemical Vapour Deposition. *Nat. Mater.* **2011**, *10*, 443–449.

[163] Yasaei, P.; Kumar, B.; Hantehzadeh, R.; Kayyalha, M.; Baskin, A.; Repnin, N.; Wang, C.; Klie, R. F.; Chen, Y. P.; Král, P.; et al. Chemical Sensing with Switchable Transport Channels in Graphene Grain Boundaries. *Nat. Commun.* **2014**, *5*, 4911.

[164] Perdew, J.; Burke, K.; Ernzerhof, M. Generalized Gradient Approximation Made Simple. *Phys. Rev. Lett.* **1996**, *77*, 3865–3868.

[165] Kresse, G.; Furthmüller, J. Efficient Iterative Schemes for Ab Initio Total-Energy Calculations Using a Plane-Wave Basis Set. *Phys. Rev. B* **1996**, *54*, 11169–11186.

[166] Lee, G. Do; Wang, C. Z.; Yoon, E.; Hwang, N. M.; Ho, K. M. Vacancy Defects and the Formation of Local Haeckelite Structures in Graphene from Tight-Binding Molecular Dynamics. *Phys. Rev. B: Condens. Matter Mater. Phys.* **2006**, *74*.

[167] Lee, G.-D.; Wang, C. Z.; Yoon, E.; Hwang, N.-M.; Kim, D.-Y.; Ho, K. M. Diffusion, Coalescence, and Reconstruction of Vacancy Defects in Graphene Layers. *Phys. Rev. Lett.* **2005**, *95*, 205501.

[168] Tang, M. S.; Wang, C. Z.; Chan, C. T.; Ho, K. M. Environment-Dependent Tight-Binding Potential Model. *Phys. Rev. B* **1996**, *53*, 979–982.

[169] Cowley, J. M.; Moodie, A. F. The Scattering of Electrons by Atoms and Crystals. I. A New Theoretical Approach. *Acta Crystallogr.* **1957**, *10*, 609–619.

[170] Goodman, P.; Moodie, A. F. Numerical Evaluation of N-Beam Wave Functions in Electron Scattering by the Multi-Slice Method. *Acta Crystallogr. Sect. A Cryst. Physics, Diffraction, Theor. Gen. Crystallogr.* **1970**, *30*, 280–290.

[171] Hÿtch, M. J.; Snoeck, E.; Kilaas, R. Quantitative Measurement of Displacement and Strain Fields from HREM Micrographs. *Ultramicroscopy*

1998, *74*, 131–146.

[172] Volterra, V. Sull' Equilibrio Dei Corpi Elastici Più Volte Connessi. *Nuovo Cim. Ser. 5* **1905**, *10*, 361–385.

[173] Read, W. T.; Shockley, W. Dislocation Models of Crystal Grain Boundaries. *Phys. Rev.* **1950**, *78*, 275–289.

[174] Hull, D.; Brody, S. B. Introduction to Dislocations. *Am. J. Phys.* **1968**, *36*, 174.

[175] Yazyev, O. Magnetism in Disordered Graphene and Irradiated Graphite. *Phys. Rev. Lett.* **2008**, *101*, 37203.

[176] Ishigami, M.; Chen, J. H.; Cullen, W. G.; Fuhrer, M. S.; Williams, E. D. Atomic Structure of Graphene on SiO2. *Nano Lett.* **2007**, *7*, 1643–1648.

[177] Bae, S.; Kim, H.; Lee, Y.; Xu, X.; Park, J.-S.; Zheng, Y.; Balakrishnan, J.; Lei, T.; Kim, H. R.; Song, Y. Il; et al. Roll-to-Roll Production of 30-Inch Graphene Films for Transparent Electrodes. *Nat. Nanotechnol.* **2010**, *5*, 574–578.

[178] Krasheninnikov, A. V; Lehtinen, P. O.; Foster, A. S.; Pyykkö, P.; Nieminen, R. M. Embedding Transition-Metal Atoms in Graphene: Structure, Bonding, and Magnetism. *Phys. Rev. Lett.* **2009**, *102*, 126807.

[179] Hawkes, P. W. Aberration Correction Past and Present. *Philos. Trans. R. Soc. London A Math. Phys. Eng. Sci.* **2009**, *367*, 3637–3664.

[180] Ramasse, Q. M.; Zan, R.; Bangert, U.; Boukhvalov, D. W.; Son, Y. W.; Novoselov, K. S. Direct Experimental Evidence of Metal-Mediated Etching of Suspended Graphene. *ACS Nano* **2012**, *6*, 4063–4071.

[181] Jeong, B.; Ihm, J.; Lee, G.-D. Stability of Dislocation Defect with Two Pentagon-Heptagon Pairs in Graphene. *Phys. Rev. B* **2008**, *78*, 165403.

[182] Fasolino, A.; Los, J. H.; Katsnelson, M. I. Intrinsic Ripples in Graphene. *Nat. Mater.* **2007**, *6*, 858–861.

[183] Bonilla, L. L.; Carpio, A. Model of Ripples in Graphene. *Phys. Rev. B* **2012**, *86*, 195402.

[184] Faccio, R.; Mombrú, A. W. Magnetism in Multivacancy Graphene Systems. *J. Phys. Condens. Matter* **2012**, *24*, 375304.

[185] He, Z.; He, K.; Robertson, A. W.; Kirkland, A. I.; Kim, D.; Ihm, J.; Yoon, E.; Lee, G.-D.; Warner, J. H. Atomic Structure and Dynamics of Metal Dopant Pairs in Graphene. *Nano Lett.* **2014**, *14*, 3766–3772.

[186] Santos, E. J. G.; Ayuela, A.; Sánchez-Portal, D. First-Principles Study of Substitutional Metal Impurities in Graphene: Structural, Electronic and Magnetic Properties. *New Journal of Physics*, 2010, *12*, 53012.

[187] Lee, G.-D.; Yoon, E.; Hwang, N.-M.; Wang, C.-Z.; Ho, K.-M. Formation and Development of Dislocation in Graphene. *Appl. Phys. Lett.* **2013**, *102*, 21603.

[188] Yakobson, B. I. Mechanical Relaxation and “intramolecular Plasticity” in Carbon Nanotubes. *Appl. Phys. Lett.* **1998**, *72*, 918–920.

[189] Ding, F.; Jiao, K.; Wu, M.; Yakobson, B. I. Pseudoclimb and Dislocation Dynamics in Superplastic Nanotubes. *Phys. Rev. Lett.* **2007**, *98*, 75503.

[190] Ding, F.; Jiao, K.; Lin, Y.; Yakobson, B. I. How Evaporating Carbon Nanotubes Retain Their Perfection? *Nano Lett.* **2007**, *7*, 681–684.

[191] Yazyev, O. V.; Louie, S. G. Topological Defects in Graphene: Dislocations and Grain Boundaries. *Phys. Rev. B* **2010**, *81*, 195420.

[192] Warner, J. H.; Margine, E. R.; Mukai, M.; Robertson, A. W.; Giustino, F.; Kirkland, A. I. Dislocation-Driven Deformations in Graphene. *Science*, 2012, *337*, 209–212.

[193] Gong, C.; He, K.; Robertson, A. W.; Yoon, E.; Lee, G.-D.; Warner, J. H. Spatially Dependent Lattice Deformations for Dislocations at the Edges of Graphene. *ACS Nano* **2015**, *9*, 656–662.

[194] Suenaga, K.; Wakabayashi, H.; Koshino, M.; Sato, Y.; Urita, K.; Iijima, S. Imaging Active Topological Defects in Carbon Nanotubes. *Nature nanotechnology*, 2007, *2*, 358–360.

[195] He, K.; Robertson, A. W.; Fan, Y.; Allen, C. S.; Lin, Y.-C.; Suenaga, K.; Kirkland, A. I.; Warner, J. H. Temperature Dependence of the Reconstruction of Zigzag Edges in Graphene. *ACS Nano* **2015**, *9*, 4786–4795.

[196] Huang, J. Y.; Chen, S.; Wang, Z. Q.; Kempa, K.; Wang, Y. M.; Jo, S. H.; Chen, G.; Dresselhaus, M. S.; Ren, Z. F. Superplastic Carbon Nanotubes. *Nature* **2006**, *439*, 281.

[197] Huang, J. Y.; Ding, F.; Jiao, K.; Yakobson, B. I. Real Time Microscopy, Kinetics, and Mechanism of Giant Fullerene Evaporation. *Phys. Rev. Lett.* **2007**, *99*, 175503.

[198] Robertson, A. W.; Warner, J. H. Atomic Resolution Imaging of Graphene by Transmission Electron Microscopy. *Nanoscale* **2013**, *5*, 4079–4093.

[199] Gong, C.; Robertson, A. W.; He, K.; Ford, C.; Watt, A. a R.; Warner, J. H. Interactions of Pb and Te Atoms with Graphene. *Dalton Trans.* **2014**, *43*, 7442–7448.

[200] Wang, Z.; Zhou, Y. G.; Bang, J.; Prange, M. P.; Zhang, S. B.; Gao, F. Modification of Defect Structures in Graphene by Electron Irradiation: Ab Initio Molecular Dynamics Simulations. *J. Phys. Chem. C* **2012**, *116*, 16070–16079.

[201] Lehtinen, O.; Kotakoski, J.; Krasheninnikov, A. V.; Tolvanen, A.; Nordlund, K.; Keinonen, J. Effects of Ion Bombardment on a Two-Dimensional Target: Atomistic Simulations of Graphene Irradiation. *Phys. Rev. B: Condens. Matter Mater. Phys.* **2010**, *81*.

[202] Peierls, R. The Size of a Dislocation. *Proc. Phys. Soc.* **1940**, *52*, 34–37.

[203] Alemán, B.; Regan, W.; Aloni, S.; Altoe, V.; Alem, N.; Girit, C.; Geng, B.; Maserati, L.; Crommie, M.; Wang, F.; et al. Transfer-Free Batch Fabrication of Large-Area Suspended Graphene Membranes. *ACS Nano* **2010**, *4*, 4762–4768.

[204] Bhaviripudi, S.; Jia, X.; Dresselhaus, M. S.; Kong, J. Role of Kinetic Factors in Chemical Vapor Deposition Synthesis of Uniform Large Area Graphene Using Copper Catalyst. *Nano Lett.* **2010**, *10*, 4128–4133.

[205] Li, X.; Magnuson, C. W.; Venugopal, A.; Tromp, R. M.; Hannon, J. B.; Vogel, E. M.; Colombo, L.; Ruoff, R. S. Large-Area Graphene Single Crystals Grown by Low-Pressure Chemical Vapor Deposition of Methane on Copper. *J. Am. Chem. Soc.* **2011**, *133*, 2816–2819.

[206] Mattevi, C.; Kim, H.; Chhowalla, M. A Review of Chemical Vapour Deposition of Graphene on Copper. *J. Mater. Chem.* **2011**, *21*, 3324–3334.

[207] Kim, H.; Mattevi, C.; Calvo, M. R.; Oberg, J. C.; Artiglia, L.; Agnoli, S.; Hirjibehedin, C. F.; Chhowalla, M.; Saiz, E. Activation Energy Paths for Graphene Nucleation and Growth on Cu. *ACS Nano* **2012**, *6*, 3614–3623.

[208] Wu, W.; Jauregui, L. A.; Su, Z.; Liu, Z.; Bao, J.; Chen, Y. P.; Yu, Q. Growth of Single Crystal Graphene Arrays by Locally Controlling Nucleation on Polycrystalline Cu Using Chemical Vapor Deposition. *Adv. Mater.* **2011**, *23*, 4898–4903.

[209] Wu, Y. A.; Fan, Y.; Speller, S.; Creeth, G. L.; Sadowski, J. T.; He, K.; Robertson, A. W.; Allen, C. S.; Warner, J. H. Large Single Crystals of Graphene on Melted Copper Using Chemical Vapor Deposition. *ACS Nano* **2012**, *6*, 5010–5017.

[210] Hao, Y.; Bharathi, M. S.; Wang, L.; Liu, Y.; Chen, H.; Nie, S.; Wang, X.; Chou, H.; Tan, C.; Fallahazad, B.; et al. The Role of Surface Oxygen in the Growth of Large Single-Crystal Graphene on Copper. *Science* **2013**, *342*, 720–723.

[211] Geng, D.; Meng, L.; Chen, B.; Gao, E.; Yan, W.; Yan, H.; Luo, B.; Xu, J.; Wang, H.; Mao, Z.; et al. Controlled Growth of Single-Crystal Twelve-Pointed Graphene Grains on a Liquid Cu Surface. *Adv. Mater.* **2014**, *26*, 6423–6429.

[212] Carlsson, J. M.; Ghiringhelli, L. M.; Fasolino, A. Theory and Hierarchical Calculations of the Structure and Energetics of [0001] Tilt Grain Boundaries in Graphene. *Phys. Rev. B: Condens. Matter Mater. Phys.* **2011**, *84*, 165423.

[213] Kim, K.; Lee, Z.; Regan, W.; Kisielowski, C.; Crommie, M. F.; Zettl, A. Grain Boundary Mapping in Polycrystalline Graphene. *ACS Nano* **2011**, *5*, 2142–2146.

[214] Lee, G.-D.; Yoon, E.; Wang, C.-Z.; Ho, K.-M. Atomistic Processes of Grain Boundary Motion and Annihilation in Graphene. *J. Phys. Condens. Matter* **2013**, *25*, 155301.

[215] Zhang, Z.; Yang, Y.; Xu, F.; Wang, L.; Yakobson, B. I. Unraveling the Sinuous Grain Boundaries in Graphene. *Adv. Funct. Mater.* **2015**, *25*, 367–373.

[216] Albrecht, T. R.; Mizes, H. A.; Nogami, J.; Park, S.; Quate, C. F. Observation of Tilt Boundaries in Graphite by Scanning Tunneling Microscopy and Associated Multiple Tip Effects. *Appl. Phys. Lett.* **1988**, *52*, 362–364.

[217] Liu, Z.; Lin, Y.-C.; Lu, C.-C.; Yeh, C.-H.; Chiu, P.-W.; Iijima, S.; Suenaga, K. In Situ Observation of Step-Edge in-Plane Growth of Graphene in a STEM. *Nat. Commun.* **2014**, *5*, 4055.

[218] Frenken, G. C. D. and D. W. van B. and M. J. R. and J. W. M. Graphene Formation on Metal Surfaces Investigated by in-Situ Scanning Tunneling Microscopy. *New J. Phys.* **2012**, *14*, 53033.

[219] Günther, S.; Dänhardt, S.; Ehrensperger, M.; Zeller, P.; Schmitt, S.; Wintterlin, J. High-Temperature Scanning Tunneling Microscopy Study of the Ordering Transition of an Amorphous Carbon Layer into Graphene on Ruthenium(0001). *ACS Nano* **2013**, *7*, 154–164.

[220] Patera, L. L.; Africh, C.; Weatherup, R. S.; Blume, R.; Bhardwaj, S.; Castellarin-Cudia, C.; Knop-Gericke, A.; Schloegl, R.; Comelli, G.; Hofmann, S.; et al. In Situ Observations of the Atomistic Mechanisms of Ni Catalyzed Low Temperature Graphene Growth. *ACS Nano* **2013**, *7*, 7901–7912.

[221] Dong, G.; Frenken, J. W. M. Kinetics of Graphene Formation on Rh(111) Investigated by In Situ Scanning Tunneling Microscopy. *ACS Nano* **2013**, *7*, 7028–7033.

[222] Günther, S.; Dänhardt, S.; Wang, B.; Bocquet, M.-L.; Schmitt, S.; Wintterlin, J. Single Terrace Growth of Graphene on a Metal Surface. *Nano Lett.* **2011**, *11*, 1895–1900.

[223] Warner, J. H.; Lin, Y.-C.; He, K.; Koshino, M.; Suenaga, K. Stability and Spectroscopy of Single Nitrogen Dopants in Graphene at Elevated Temperatures. *ACS Nano* **2014**, *11*, 11806–11815.

[224] Sutter, E.; Sutter, P.; Zhu, Y. Assembly and Interaction of Au/C Core−Shell Nanostructures: In Situ Observation in the Transmission Electron Microscope. *Nano Lett.* **2005**, *5*, 2092–2096.

[225] Koga, K.; Ikeshoji, T.; Sugawara, K. Size- and Temperature-Dependent Structural Transitions in Gold Nanoparticles. *Phys. Rev. Lett.* **2004**, *92*, 115507.

[226] Shu, H.; Chen, X.; Tao, X.; Ding, F. Edge Structural Stability and Kinetics of Graphene Chemical Vapor Deposition Growth. *ACS Nano* **2012**, *6*, 3243–3250.

[227] Koskinen, P.; Malola, S.; Häkkinen, H. Self-Passivating Edge Reconstructions of Graphene. *Phys. Rev. Lett.* **2008**, *101*, 115502.

[228] Gong, C.; Robertson, A. W.; He, K.; Lee, G.-D.; Yoon, E.; Allen, C. S.; Kirkland, A. I.; Warner, J. H. Thermally Induced Dynamics of Dislocations in Graphene at Atomic Resolution. *ACS Nano* **2015**, *9*, 10066–10075.

[229] Liu, T. H.; Gajewski, G.; Pao, C. W.; Chang, C. C. Structure, Energy, and Structural Transformations of Graphene Grain Boundaries from Atomistic Simulations. *Carbon* **2011**, *49*, 2306–2317.

[230] Boukhvalov, D. W.; Katsnelson, M. I. Chemical Functionalization of Graphene with Defects. *Nano Lett.* **2008**, *8*, 4374–4379.

[231] Zhang, Y.-H.; Chen, Y.-B.; Zhou, K.-G.; Liu, C.-H.; Zeng, J.; Zhang, H.-L.; Peng, Y. Improving Gas Sensing Properties of Graphene by Introducing Dopants and Defects: A First-Principles Study. *Nanotechnology* **2009**, *20*, 185504.

[232] López-Sancho, M. P.; de Juan, F.; Vozmediano, M. A. H. Magnetic Moments in the Presence of Topological Defects in Graphene. *Phys. Rev. B* **2009**, *79*, 75413.

[233] Khosravian, N.; Samani, M. K.; Loh, G. C.; Chen, G. C. K.; Baillargeat, D.; Tay, B. K. Effects of a Grain Boundary Loop on the Thermal Conductivity of Graphene: A Molecular Dynamics Study. *Comput. Mater. Sci.* **2013**, *79*, 132–135.

[234] Robertson, A. W.; Lee, G.-D.; He, K.; Fan, Y.; Allen, C. S.; Lee, S.; Kim, H.; Yoon, E.; Zheng, H.; Kirkland, A. I.; et al. Partial Dislocations in Graphene and Their Atomic Level Migration Dynamics. *Nano Lett.* **2015**, *15*, 5950–5955.